Study of Synthesis and Formation Mechanism of Metal Nanoparticles(Dissertation_全文)

AUTHOR(S):

Ohyama, Junya

Study of Synthesis and Formation Mechanism of Metal Nanoparticles

JUNYA OHYAMA

2011

Study of Synthesis and Formation Mechanism of Metal Nanoparticles

JUNYA OHYAMA

Department of Molecular Engineering

Graduate School of Engineering

KyotoUniversity

2011

Preface

In 2007, Gerhard Ertl won the Nobel Prize for his studies of chemical processes on solid surfaces. In the last four decades, surface chemistry achieved remarkable development to provide information of the surface structures and the behavior of molecular at an atomic level, owing to the progression of observation techniques. The surface chemistry has been applied to catalytic reaction on solid surfaces in order to study the relation between structures of solid surfaces and catalyses. As a result, nature of the catalysis has been getting clearer. On the other hand, there have been attempts to design active sites of catalysts at an atomic level, since the control of the catalytically active site leads to the achievement of the ideal reaction, such as a reaction producing desired product with 100% selectivity, which is the challenge of chemistry in the 21st century.

Nanometer-scale metals (1 - 10 nm), so called metal nanoparticles, are regarded as the candidate to achieve the ideal catalytic reaction. Metal nanoparticles show different properties from bulk metals due to high fraction of surface atoms and discrete electronic structure, and the properties dramatically vary with their size. What made the greatest impact on scientists is the catalytic activity of gold nanoparticles discovered by Haruta et al in 1982. Gold nanoparticles catalyze the oxidation of carbon monoxide even at 203 K, however bulk gold is inert. The catalytic activity increases with a decrease with the size of gold nanoparticles, and, notably, small gold nanoparticles having less than 2 nm diameter represents drastic enhancement of the catalytic activity as well as the peculiar selectivity, which cannot be explained only by their high fraction of the surface atoms. From this discovery, an intense attention has been focused on the origin and/or application of the unique property of gold nanoparticles, particularly, the size dependent property.

The properties of metal nanoparticles are also influenced by interaction between metal and support (protective agent). Tauster et al reported in 1978 that platinum nanoparticles on TiO_2 lose their capability of adsorption of substrate and catalytic activity by hydrogen treatment at high temperature (> 773 K). They called this phenomenon “strong metal support interaction (SMSI)”. Numerous studies have showed that the strong interaction causes the encapsulation of platinum nanoparticles with TiO_2 and the change of their electronic state. In the same year 1978, Bard et al. reported a new preparation method of

metal nanoparticles on a photocatalyst, so called photodeposition: photoexited electrons in a semiconductor photocatalyst reduce metal ions to deposit metal nanoparticles on the photocatalyst. The metal nanoparticles prepared by photodeposition often demonstrate higher catalytic activity than those prepared by the other conventional methods. The photodeposited metal particles might effectively modify and interact with a photocatalyst to separate the electrons and holes generated by photoirradiation.

On the other hand, the interaction between metal and support (protective agent) has effect on the morphology of metal nanoparticles. In 1995, Brust et al. synthesized gold nanoparticles by taking advantage of the strong interaction between thiol group and gold to form Au-S bonds as well as assemble of alkanethiol on the surface of gold. The strong interaction affords the small and uniformly dispersed gold nanoparticles, which clearly demonstrates that the metal-support interaction affects the morphology of metal nanoparticles.

On these backgrounds, for development and improvement of the unique property of metal nanoparticles, it is essential to understand metal-support interaction. Furthermore, the author believes that the study of formation mechanism of metal nanoparticles is also needed. This is because the understanding of the interaction and mechanism should lead to a new idea or a guideline for design of morphology and electronic property of metal nanoparticles.

From this perspective, the author has studied the formation mechanism of metal nanoparticles for a couple of preparation systems. One is gold nanoparticles covered with thiols, and the other is metal nanoparticles photodeposited on TiO_2. In the study on the formation mechanism, the metal-support interaction and the electronic properties of metal particles were focused. The author also developed the efficient synthesis of small gold nanoparticles in consideration of metal-support interaction.

The study in this thesis has been performed at Department of Molecular Engineering, Graduate School of Engineering, Kyoto University from 2008 to 2011 under supervision of Professor Tsunehiro Tanaka. The author wishes to express his sincerest gratitude to Professor Tsunehiro Tanaka for his invaluable guidance, fruitful discussions, worthy suggestions, and hearty encouragement, throughout this study. The author is deeply grateful to Professor Tetsuya Shishido for his profitable discussion, helpful suggestions, and continual

encouragement. The author is profoundly grateful to Dr. Kentaro Teramura for his valuable discussions, precious suggestions, and heartwarming advices. The author makes special acknowledgement to Professor Yutaka Hitomi at Doshisha University for his exact guidance, fruitful discussions, and instructive suggestions. Thanks are made to Assistant Professor Seiji Yamazoe at Ryukoku University, who was a senior of the laboratory the author belongs to, for the useful advices to experiment, and helpful suggestions and discussions. The author appreciates Professor Masahito Kodera and Professor Takuzo Funabiki at Doshisha University for their valuable discussions and encouragement. Hearty thanks are made to Professor Tomoya Uruga, Professor Hajime Tanida, and Mr. Kazuo Kato at SPring-8 in Hyogo prefecture not only for their technical aids and advices in the measurement of X-ray absorption fine structure (XAFS), but also for their helpful discussions and suggestions. Thanks must be made to the staffs of Photon Factory at KEK in Ibaraki prefecture and SPring-8 in Hyogo prefecture for the technical supports in the XAFS measurement. The author is grateful to Dr. Saburo Hosokawa, Professor Kenji Wada, and Professor Masashi Inoue for their aid in obtaining X-ray photoelectron spectra and in ICP spectroanalysis. Dr. Asako Narita at The University of Alabama, Professor Kensuke Naka at Kyoto Institute of Technology, Professor Yoshiki Chujo at Kyoto University, and Professor Mitsuru Funato at Kyoto University for their help in transmission electron microscope observation.

The author is indebted to Messrs. Yasuhiro Higuchi, Masashi Shinagawa, Kazuki Aoki, and Dr. Hidefumi Mukai who have collaborated the synthesis of gold nanoparticles passivated with novel porphyrin passivants described in Part I. The author also deeply thanks to Messrs. Shin-ich Okuoka and Akira Yamamoto for their cooperation and discussions on the study of the photodeposition mechanism described in Part II. Thanks should be made to Secretary Ms. Ayako Tanaka for her kind official supports. The author is grateful to all the members of the group of catalysis research led by Professor Tanaka.

Finally, the author sincerely thanks his parents, Hiroaki and Yukari, for their understanding and encouragement.

Junya Ohyama

Kyoto,

December, 2010

CONTENTS

Part I

Synthesis, Formation Mechanism, and Size Dependent Electronic Property of Thiolate Passivated Gold Nanoparticles

Introduction of Part I

There has been considerable interest in the unique properties of metal nanoparticles, such as catalytic activity, optical, and magnetic properties, depending on their size.[1-4] In order to apply the unique properties of metal nanoparticles, the synthesis of well-defined metal nanoparticles is demanded. In this view point, inorganic synthesis chemists have investigated preparation methods of such metal nanoparticles through the development of synthesis of colloidal metal nanoparticles, that is, wet chemical synthesis of metal nanoparticles. As a result, they have accumulated the methods and conditions for size control synthesis. In parallel, the formation mechanism of metal nanoparticles has been studied to understand the effect of the synthesis conditions on the size of metal nanoparticles and give the guide line for syntheses of a predesigned nanoparticle.

In this introductory part, the author briefly describes the synthesis methods of metal nanoparticles, formation mechanism of metal nanoparticles, and strategy for control the size of metal nanoparticles.

1. Wet chemical synthesis of metal nanoparticles

Metal nanoparticles can be easily synthesized by reduction of metal salts (wet chemical synthesis). As reducing agents, for example sodium, citric acid, ascorbic acid, borohydride, diborane, hydrogen, and alcohol are utilized. When citric acid or ascorbic acid is used as a reducing agent, the resulting metal nanoparticles are stabilized by electrostatic repulsion due to the adsorbed citric acid ions on the surface of metal.[5] On the other hand, when the reducing agents which do not prevent aggregation of particles are used, passivants are applied to hinder particle aggregation sterically. Organic polymers such as polyvinylpyrroldone, polyvinylalcohol, and polyvinylether are often utilized as passivants, particularly in alcohol reduction process which is one of the most widely used methods for preparation of metal nanoparticles. In this process, metal ions are reduced by heated alcohols in the presence of passivants.[6-10] Polyols (e.g. ethylene glycol) are also applied in the same manner as alcohol, which is called polyol reduction method.[11] When surfactants, for example,

alkyl ammonium compounds, are utilized as a paasivant, they form micelle or inverted micelle in a solution which provide not only reaction field for formation of metal nanoparticles but also protecting layer for metal nanoparticles.[12] This method is called micelle or inverse micelle method. Brust et al. developed the inverse micelle method by using an alkanethiol as a passivant which strongly binds to a surface of metal nanoparticles and self-assembles into monolayer on metal surface to prevent the coalescence and growth of metal nanoparticles (Brust method).[13] It is also noted that they used sodium borohydride as a reducing agent. As a result, monodisperse small gold nanoparticles covered with thiolates were synthesized. There are other wet chemical synthesis methods, for example, heat and photolytic degradation of organic metallic compounds,[14,15] and reduction of ligands of metallo-organic complexes[16], and so on. In addition, various protecting agents are applied to each synthesis method of metal nanoparticles. These preparation methods have developed the synthesis of structure-specific metal particles. Owing to these efforts, very recently, a number of atomically monodisperse nanoparticles have been available.[17,18] For synthesis of a series of precisely size-controlled metal particles, the researches on preparation methods are now underway.

2. Particle Formation Mechanism

In 1950, LaMer et al. studied the formation mechanism of sulfur sol to propose that the sol is formed by vast nucleation from supersaturated solution of monomer and growth by attachment of monomers to the resulting nuclei.[19] This LaMer mechanism has been applied to formation mechanism of metal nanoparticles and is one of the most popular formation mechanisms of metal nanoparticles.[20] On the other hand, Finke et al. have studied the formation kinetics and mechanism of Iridium nanoparticles from iridium precursors by H_2 reduction.[20] They proposed a different mechanism from LaMer one that nuclei are formed slowly but constantly and the nanoparticles grow mainly by autocatalytic reduction of metal precursors on the particle surface. Although both of the mechanisms are different in kinetics of nucleation, particle growth process mainly proceeds by the addition of monomer (precursor) on the particle surface in the mechanisms. In contrast, Baiker et al. studied the

formation mechanism of gold precursors by using the strong reducing agents and strongly passivating agents, and they proposed that combination/coalescence of particles is the dominant growth mechanism for the formation of gold nanoparticles.[21] In addition to these mechanisms, the other authors proposed that thermodynamic factors for passivation[22,23] or Ostwald ripening which is particle growth by redeposition of dissolved species of small particles on the surface of large nanoparticles[24] contribute the formation mechanism of metal nanoparticles. Although there are many studies of particle formation mechanism, it is still unclear. This is due to the difficulties of observation of the formation process, more specifically the nucleation process. Since the formation mechanisms can be utilized as a guide line for design of morphology of metal nanoparticles, it is necessary to investigate particle formation mechanism more closely.

3. Size Control

Here, the author would like to consider how the size of metal nanparticles can be controlled on the basis of a simple particle formation mechanism shown in Scheme 1.[25] When particles grow by addition of metal atoms on a surface of particle without Ostwald ripening and aggregation between particles, the size should vary with the number of nuclei, in other words, relative rate of nucleation to growth.

Scheme 1 Brief formation mechanism of metal nanoparticles.[25]

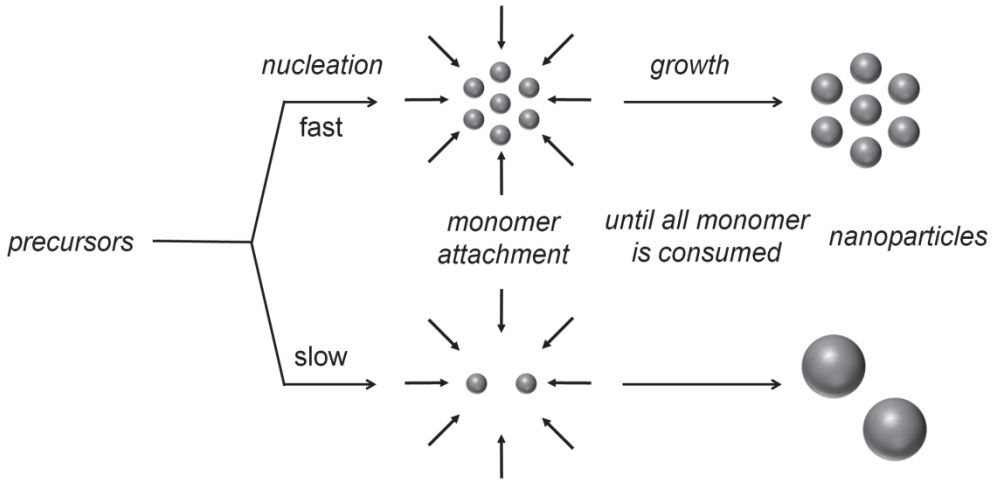

The high relative rate increases the number of particles and leads the small particles. On the contrary, the low relative rate results in the low concentration of particles and thus formation of large metal particles. Therefore, understanding and manipulation of the relative rate of nucleation to growth is critical for control the size of metal nanoparticles. The relative rate can be controlled by reduction rate of metal precursors, the initial molar ratio of a passivant to a metal precursor, and the affinity of passivants for metal species and the structure of passivants.

3-1. Reduction Rate of Metal Precursors Borohydrides reduce metal precursors faster than alcohols. Teranishi et al. reported the dependence of the size of gold nanoparticles protected by PVP on the kinds of reducing agents, alcohols and potassium borohydride.[26] The reduction with alcohols provided polydispersed gold nanoparticles having 2 – 14 nm diameter. On the other hand, the reduction with potassium borohydride afforded monodispersed particles with ca. 2 nm diameter. They also investigated the variation of the particle size with the amount of potassium borohydride, and showed that the particle size increases as a decrease in the concentration of potassium borohydrides. This result indicates that the fast reduction of gold ions causes the formation of large number of nuclei and provides small particles. In the case of the preparation of platinum and palladium nanoparticles using alcohol reduction method, the alcohol having strong reducing power gave the small metal nanoparticles.[27,28] It is concluded that the rapid reduction of metal ions causes the fast nucleation and which results in formation of many nuclei and then small metal nanoparticles.

3-2. Ratio of passivants to metal precursors Generally, the small metal nanoparticles are formed at the high molar ratio of passivants to precursors. The large amount of passivants will suppress the growth of metal nanoparticles, which makes the relative rate of nucleation to growth fast and provides small metal nanoparticles.[22,26-29] However, there is an exception. Weller et al. reported that the size of $CoPt_3$ increased with an increase in the ratio of 1-adamantanecarboxylic acid to metal precursors.[25] They proposed that the passivant strongly stabilizes the metal precursors, and thus the large amount of the passivant decreases the

nucleation rate. As for the preparation of gold nanoparticles covered with alkanethiol by using the Brust method, the particle size decreases from 5 nm to 2 nm with an increase in the ratio of alkanethiol to gold ion.[22] This variation of particle size can be explained by the kinetic control mechanism. However, Leff et al. proposed that the size of gold nanoparticles with alkanethiol is determined by the thermodynamic factors for surface stabilization rather than the relative rate of nucleation to particle growth.[22] Although the control of particle size by the ratio of passivants to metal precursors is easy and useful, it is necessary to understand the role of passivants in the particle formation process in more detail.

3-3. Affinity of Passivants for Metal Species and Structure of Passivants As described above, the affinity of passivants for metal precursors has an effect on the size-controlled behavior of metal nanoparticles. The interaction of passivants to the surface of metal can also affect the size of metal nanoparticles. For example, it was reported that the passivants with thiol and cyano groups which are known to have a high affinity for gold gave smaller and narrower size-distributed gold nanoparticles than the passivants with carbonyl and alcohol groups having a low affinity for gold.[26] The strong interaction of passivant to metal surface will provide small metal particles in the wet chemical synthesis. The affinity has been also manipulated by the structure of passivant such as bulkiness and multidentation. Yonezawa et al. demonstrated that smaller gold nanoparticles can be obtained by the use of a four-chained disulfide passivant, that is, a bulky passivant, than those prepared by using monoalkanethiols.[30] On the other hand, Mayor et al. have synthesized a series of linear oligomeric multidentate thioether ligands, and demonstrated a considerable increase in the stability and monodispersity of the resultant gold nanoparticles with the increasing length of the oligomeric ligands.[31] Recently, such passivants have been attracted the attention for the synthesis of size-specific metal nanoparticles, because the structure of passivants and their unique stabilization of particle surface can contribute the structure of metal particles.[32] However, it is not unclear how the structures of passivants act in the formation of metal nanoparticles.

4. Survey of Part I

Gold nanoparticles show unique properties deviated from the bulk, for example, catalytic reactivity and optical properties. Of particular interest is the dramatic change of the properties of gold nanoparticles with less than ca. 2 nm diameter. In order to efficiently synthesize such small gold nanoparticles, the author designed and synthesized new multidentate passivants having sulfur functional groups. In chapter 1 and 2, the author synthesized and characterized the gold nanoparticles capped by the multidentate passivants, and presents the size control synthesis of gold nanoparticles. In chapter 1, the ability of a multidentate passivant to control gold nanoparticles was evaluated in comparison with conventional monodentate passivants. In chapter 2, type of the sulfur functional groups of the multidentate passivants was varied to control the trapping rate of the surface of gold nanopaticles by the multidentate passivants. In chapter 3 and 4, the formation processes of gold nanoparticles with thiol passivants are observed and a mechanism is proposed. The kinetics for nucleation and particle growth are investigated by *in situ* time resolved X-ray absorption fine structure (XAFS) spectroscopy. These studies provide a new insight into not only the particle formation mechanism but also the structural effect of passivants in the particle formation process. Under favor of the particle formation mechanism, the author evaluates the electronic properties of gold nanoparticles with various sizes from sub-nanometer to ca. 5 nm by *in situ* Au L_3 and L_2 edge X-ray absorption near edge structure (XANES) spectral analysis during the particle formation. The result can explain the unique catalytic property of gold nanoparticles with less than ca. 2 nm diameter.

References

(1) Haruta, M. *Catalysis Today* **1997**, *36*, 153.

(2) Kamat, P. V. *J. Phys. Chem. B* **2002**, *106*, 7729.

(3) Hu, M.; Chen, J.; Li, Z.-Y.; Au, L.; Hartland, G. V.; Li, X.; Marquez, M.; Xia, Y. *Chem. Soc. Rev.* **2006**, *35*, 1084.

(4) Hori, H.; Teranishi, T.; Nakae, Y.; Seino, Y.; Miyake, M.; Yamada, S. *Physics Letters A* **1999**, *263*, 406.

(5) Blatchford, C. G.; Campbell, J. R.; Creighton, J. A. *Surface Science* **1982**, *120*, 435.

(6) Toshima, N.; Yonezawa, T. *New Journal of Chemistry* **1998**, *22*, 1179.

(7) Hirai, H.; Nakao, Y.; Toshima, N. *Journal of Macromolecular Science-Chemistry* **1979**, *A13*, 727.

(8) Hirai, H.; Nakao, Y.; Toshima, N. *Chemistry Letters* **1976**, 905.

(9) Hirai, H.; Nakao, Y.; Toshima, N. *Chemistry Letters* **1978**, 545.

(10) Lu, P.; Teranishi, T.; Asakura, K.; Miyake, M.; Toshima, N. *Journal of Physical Chemistry B* **1999**, *103*, 9673.

(11) Fievet, F.; Lagier, J. P.; Blin, B.; Beaudoin, B.; Figlarz, M. *Solid State Ionics* **1989**, *32-33*, 198.

(12) Bonnemann, H.; Richards, R. M. *European Journal of Inorganic Chemistry* **2001**, 2455.

(13) Brust, M.; Walker, M.; Bethell, D.; Schiffrin, D. J.; Whyman, R. *J. Chem. Soc., Chem. Commun.* **1994**, 801.

(14) Glockler, J.; Klutzke, S.; Meyer-Zaika, W.; Reller, A.; Garcia-Garcia, F. J.; Strehblow, H. H.; Keller, P.; Rentschler, E.; Klaui, W. *Angew. Chem.-Int. Edit.* **2007**, *46*, 1164.

(15) Toshima, N.; Takahashi, T.; Hirai, H. *Chemistry Letters* **1985**, 1245.

(16) Pelzer, K.; Vidoni, O.; Philippot, K.; Chaudret, B.; Colliere, V. *Advanced Functional Materials* **2003**, *13*, 118.

(17) Schmid, G. *Chemical Reviews* **1992**, *92*, 1709.

(18) Jin, R. C. *Nanoscale* **2010**, *2*, 343.

(19) LaMer, V. K.; Dinegar, R. H. *J. Am. Chem. Soc.* **1950**, *72*, 4847.

(20) Watzky, M. A.; Finke, R. G. *J. Am. Chem. Soc.* **1997**, *119*, 10382.

(21) Duff, D. G.; Baiker, A.; Edwards, P. P. *Langmuir* **1993**, *9*, 2301.

(22) Leff, D. V.; Ohara, P. C.; Heath, J. R.; Gelbart, W. M. *Journal of Physical Chemistry* **1995**, *99*, 7036.

(23) Look, J. L.; Bogush, G. H.; Zukoski, C. F. *Faraday Discussions* **1990**, 345.

(24) Matijevic, E. *Chem. Mater.* **1993**, *5*, 412.

(25) Shevchenko, E. V.; Talapin, D. V.; Schnablegger, H.; Kornowski, A.; Festin, O.; Svedlindh, P.; Haase, M.; Weller, H. *J. Am. Chem. Soc.* **2003**, *125*, 9090.

(26) Teranishi, T.; Kiyokawa, I.; Miyake, M. *Advanced Materials* **1998**, *10*, 596.

(27) Teranishi, T.; Hosoe, M.; Tanaka, T.; Miyake, M. *J. Phys. Chem. B* **1999**, *103*, 3818.

(28) Teranishi, T.; Miyake, M. *Chem. Mater.* **1998**, *10*, 594.

(29) Hostetler, M. J.; Wingate, J. E.; Zhong, C.-J.; Harris, J. E.; Vachet, R. W.; Clark, M. R.; Londono, J. D.; Green, S. J.; Stokes, J. J.; Wignall, G. D.; Glish, G. L.; Porter, M. D.; Evans, N. D.; Murray, R. W. *Langmuir* **1998**, *14*, 17.

(30) Yonezawa, T.; Yasui, K.; Kimizuka, N. *Langmuir* **2001**, *17*, 271.

(31) Peterle, T.; Leifert, A.; Timper, J.; Sologubenko, A.; Simon, U.; Mayor, M. *Chem. Commun.* **2008**, 3438.

(32) Jin, R.; Qian, H.; Wu, Z.; Zhu, Y.; Zhu, M.; Mohanty, A.; Garg, N. *J. Phys. Chem. Lett.* **2010**, *1*, 2903.

Chapter 1

One-Phase Synthesis of Small Gold Nanoparticles Coated by a Horizontal Porphyrin Monolayer

Abstract

One-pot reduction of $HAuCl_4$ in a DMF solution containing a porphyrin-cored tetradentate passivant gives horizontal porphyrin monolayer–coated gold nanoparticles, whose particle size is significantly smaller than that made by using monodentate passivants under the identical conditions.

Introduction

Gold nanoparticles coated by an alkanethiol monolayer have attracted intense attention due to their unique optical and electronic properties that can be controlled by particle size as well as nature of the protecting molecules.[1] Surface modification of gold nanoparticles with functional molecules has been utilized as a powerful method to create nanoscale devises such as memories, sensors and catalysts.[2,3] Introduction of functional molecules in well-defined orientation and alignment on gold nanoparticle surface would bring about an appreciable improvement on this approach. Multipoint Au−S bond formation would be a straight way to fix functional molecules in desired geometry. As a pioneering work, Beer and Davis and co-worker reported that multidentate zinc porphyrin-modified gold nanoparticles exhibited enhanced anion binding ability thanks to the pre-organized structure of the zinc porphyrin receptor for anion sensing.[4] However, there are still only few examples of multidentate ligands to passivate gold nanoparticles. Notably, Wei and co-workers first reported that tetrathiolated resorcinarene was able to stabilize large gold nanoparticles of up to 87 nm diameter.[5] And very recently, Lee and co-workers proved that multidentate passivants can enhance the stability of large gold nanoparticles by testing a series of monodentate, bidentate and tridentate alkanethiols.[6] Not only to stabilize gold nanoparticles, multidentate ligands have been utilized also to control interparticle distances of gold nanoparticles.[7-9] Thus, the advantages of multidentate ligands to control the properties of gold nanoparticles have been demonstrated so far, but above-mentioned gold nanoparticles all were obtained by ligand replacement from premade citrate-stabilized gold nanoparticles or through two-phase synthesis using phase transfer reagents like tetraoctylammonium bromide (TOAB), which is known as Brust's method.[10] In this study, we focused on simple one-phase method, that is, reduction of a $HAuCl_4$ solution containing multidentate passivant ligands in order to evaluate the intrinsic ability of the passivant to produce and stabilize gold nanoparticles without any assistance by other co-stabilizers such as citrate or TOAB.[6,11] Moreover, this simple system would avoid possible surface occupation by the co-stabilizers, which may block the fixation of multidentate passivant on the gold surface.

In this study, we designed a porphyrin-based surface passivant ligand (**1**) that

displays four sulfur atoms via rigid linkers in the same direction perpendicular to the porphyrin plane as shown in Figure 1. Thus, we utilized porphyrin molecule as a scafold here, since it and its metal complexes are fascinating functional molecules exhibiting unique optical and electronic properties and high catalytic activities. The ligand **1** is expected to build up fast and tight connections with gold surface via four Au-S bonds since all the four S atoms are pre-oriented to form Au-S bonds and do not rotate away due to steric hindrance between the amide moiety and the porphyrin plane, as demonstrated with the Collman's picket fence porphyrin.[12] Most importantly, this Lunar-Lander-like structure is supposed to be capable of fixing the porphyrin plane in a plane parallel with respect to the gold surface, and then enable to coat gold nanoparticles with a horizontal porphyrin monolayer.[13-15]

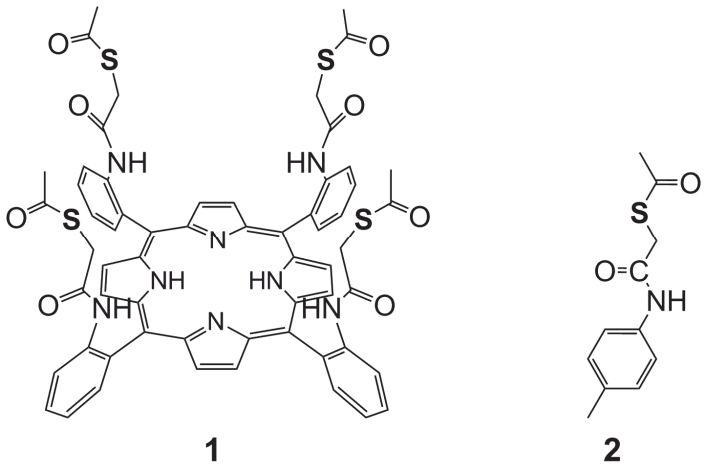

Figure 1. Structures of tetradentate and monodentate passivants, **1** and **2**.

Experimental

General methods. Electronic absorption spectra were measured on a HITACHI U-3500 UV-VIS-NIR spectrometer by using a quarts cell with a 1-cm path length. 1H, 13C, 2D (HMQC, HMBC) NMR spectra were measured in $CDCl_3$ on a JEOL JNM-ECX400 spectrometer. Transmission electron microscopy (TEM) images were taken with a JEOL JEM-100SX operating at an accelerating voltage of 100 kV.TEM samples were prepared by

depositing of drops of a methanol solution onto a carbon-coated copper grid (Okenshoji Co. LTD.) and dried to the solvent at room temperature. X-ray photoelectron spectra (XPS) were acquired using an ULVAC PHI 5500MT. XPS samples were mounted on an indium foil and the spectra were measured using Mg $K\alpha$ radiation (15 kV, 400 W) in a chamber with the base pressure of ca. 1×10^{-8} Torr. The take-off angle was set at 45º. All binding energies were corrected for charge shifting by referencing to the C(ls) line from the adventitious carbon at 284.6 eV.

Materials. All solvents were purchased from Wako Pure Chemical Industry. 2-Nitrobenzaldehyde, pyrrole, and potassium thioacetate were purchased from Tokyo Chemical Industry, and the other chemicals were from Wako Pure Chemical Industry. 5,10,15,20-Tetrakis(*o*-nitrophenyl)-porphyrin and 5,10,15,20-tetrakis(*o*-aminophenyl)-porphyrin were synthesized and the latter was atropisomerized to the $\alpha,\alpha,\alpha,\alpha$–atoropisomer according to the Lindsey's procedure.[16]

$\alpha,\alpha,\alpha,\alpha$-5,10,15,20-tetrakis(2-(S-acetyl-thioacetamido)phenyl)porphyrin (1). To a solution of α,α,α,α–5,10,15,20-tetrakis(2-aminophenyl) porphyrin (0.498 g, 0.738 mmol) in dry THF (80 mL) was diethylaniline (1.6 mL, 10.3 mmol) added under N_2. Bromoacetyl bromide (641 μL, 7.34 mmol) in CH_2Cl_2 (11 mL) was added to the mixture dropwise over 5 min at 0ºC and stirred for 1 h at 0ºC. Then, potassium thioacetate (1.7 g, 14.9 mmol) in dry EtOH (80mL) was added to the mixture and stirred for 2 h. The solvent was removed under reduced pressure. The residue was purified by column chromatography on silica gel eluted with $CHCl_3$ and subsequent recrystalization from $CHCl_3$-MeOH. 0.240 g (0.211 mmol, 29%). TLC R_f = 0.62 ($CHCl_3$:MeOH 10:1); HRMS-FAB (m/z): $[M+H]^+$ calcd for $C_{60}H_{50}O_8N_8S_4$, 1138.26; found, 1138.2642; ^{1}H NMR ($CDCl_3$, 400 MHz): δ 8.78 (s, 8H), 8.57 (d, 4H), 7.99 (d, 4H), 7.85 (dd, 4H), 7.64 (s, 4H), 7.54 (dd, 4H), 3.56 (s, 8H), 0.75 (s, 12H), -2.69 (s, 2H).; ^{13}C-NMR ($CDCl_3$, 100 MHz): δ 194.1, 165.9, 138.2, 134.6, 131.8, 131.4, 129.9, 123.6, 121.8, 114.8, 33.2, 28.7 (Carbon atoms at α position of pyrrole utits could not be observed,[17] presumably due to N-H tautomerism; UV-Vis λ_{max} in DMF: 422, 516, 550, 591, 647 nm.

4-(S-Acetyl-thioacetamido)-toluene (2). Compound **2** was synthesized by the similar procedure to **1**. *p*-Toluidine (535.8 mg, 5.00 mmol) was reacted with bromoacetyl bromide (1.1 mL, 12.6 mmol) in the presence of diethylaniline (2.5 mL, 15.6 mmol) under N_2 and 0 ºC, followed by reaction with potassium thioacetate (2.83 g, 24.8 mmol) under N_2. The product was purified by column chromatography on silica gel with chloroform and 100:1 chloroform:methanol, and followed by recrystalization from hexane-AcOEt. 0.786 g (3.52 mmol, 70%). TLC R_f = 0.50 ($CHCl_3$:MeOH 100:1); ^{1}H NMR ($CDCl_3$, 400 MHz): δ 8.02 (s, 4H), 7.37 (d, 2H), 7.12 (d, 2H), 3.65 (s, 2H), 2.45 (s, 3H), 2.31 (s, 3H). ^{13}C-NMR ($CDCl_3$, 100 MHz): δ 197.0, 166.2, 135.0, 134.2, 129.5, 120.0, 34.2, 30.3, 20.9.

Gold nanoparticles covered with 1 (GN@1). A solution of **1** (11.4 mg, 10.0 μmol) in DMF (180 mL) was added to a 300 mL round-bottom flask which was cleaned with piranha solution. 40.0 μM $HAuCl_4$ solution in DMF (2 mL) was added and the mixture was reduced with $NaBH_4$ (18.25 mg, 772 μmol) dissolved in DMF. After 2 hour stirring, the reaction mixture was evaporated to ca. 3 mL and precipitated by 30 mL of methanol to remove excess amount of **1** and $NaBH_4$. The precipitate was dissolved in 2 mL of DMF and reprecipitated by 30 mL of $CHCl_3$. The reprecipitation process was repeated five times. Purified **GN@1** was characterized by TEM, UV-vis and XPS measurements.

Size controlled synthesis of gold nanoparticles. Gold nanoparticles were synthesized in the presence of **1**, **2**, and dodecanethiol under various molar ratios (S/Au = 0, 0.1, 0.2, 1, 4 and 16). All of glass vials for the syntheses of gold nanoparticles were cleaned with piranha solution. A typical method is as follows; 8 mL of 1.01 mM **1** solution of DMF (8.08 μmol), 93.5 μL of 21.4 mM hydrogen tetrachloroaurate trihydrate solution of DMF (2.00 μmol) and 1.8 mL of DMF were added to a reaction vessel. While the mixture was vigorously stirring, 100 μL of 0.248 M sodium borohydride (24.8 mmol) was swiftly added and then stirred for 1 hour. The solutions were evaporated and the residue was dispersed in MeOH. All samples were observed by TEM without purification.

Results and Discussions

Figure 2 shows UV-vis spectrum of purified **GN@1** which was prepared at a molar ratio of **1** to $HAuCl_4$ of 1. The spectrum showed both features characteristic of porphyrin and gold nanoparticles; the Soret and Q bands at 426 nm and 500 to 670 nm, respectively, and the surface plasmon band at around 530 nm. The Soret band for **GN@1** was significantly broadened and red-shifted compared with that for **1** before reduction; 426 nm (FHW 13 nm) for **GN@1** vs. 422 nm (FHW 9.6 nm) for **1**, suggesting the electronic interactions between gold nanoparticles and the porphyrin and/or side-by-side alignment of **1** on the gold surface.[9,18] Although gold nanoparticles could be formed by $NaBH_4$ reduction of $HAuCl_4$ in DMF without **1**, the resultant gold nanoparticles were unstable and easily precipitated as gold chunks. In contrast, the gold nanoparticles **GN@1** did not change the surface plasmon band over weeks, apparently due to the surface coating with **1**.

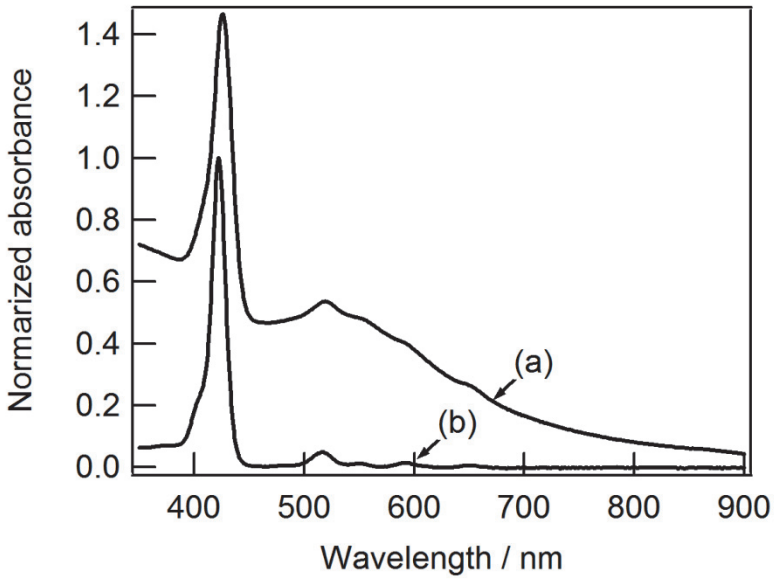

Figure 2. UV-vis spectra of **GN@1** (a) and **1** (b) in DMF.

Figure 3a shows a representative TEM image of **GN@1**, where crystal lattice of gold was observed. Particle analysis revealed that **GN@1** has a mean diameter of 3.5 ± 0.7 nm. The size of alkanethiol-protected gold nanoparticles has been demonstrated to be controlled by the initial thiol/gold ratio (ξ).[19] Therefore, we prepared **GN@1** at various ratios of **1** to $HAuCl_4$ from 0.025 to 4, which correspond to ξ values from 0.1 to 16. Analyzed particles sizes are plotted against ξ values in Figure 4, where the particle size decreased down to ca. 2 nm as increasing ξ to 16. To evaluate the capability of **1** to control the size of formed gold nanoparticles, as a control we synthesized a monodentate surface passivant ligand (**2**) whose structure was taken from **1** (Figure 1), and prepared monodentate-thiol-protected gold nanoparticles (**GN@2**) at different values of ξ from 0.1 to 16. The particle size of **GN@2**

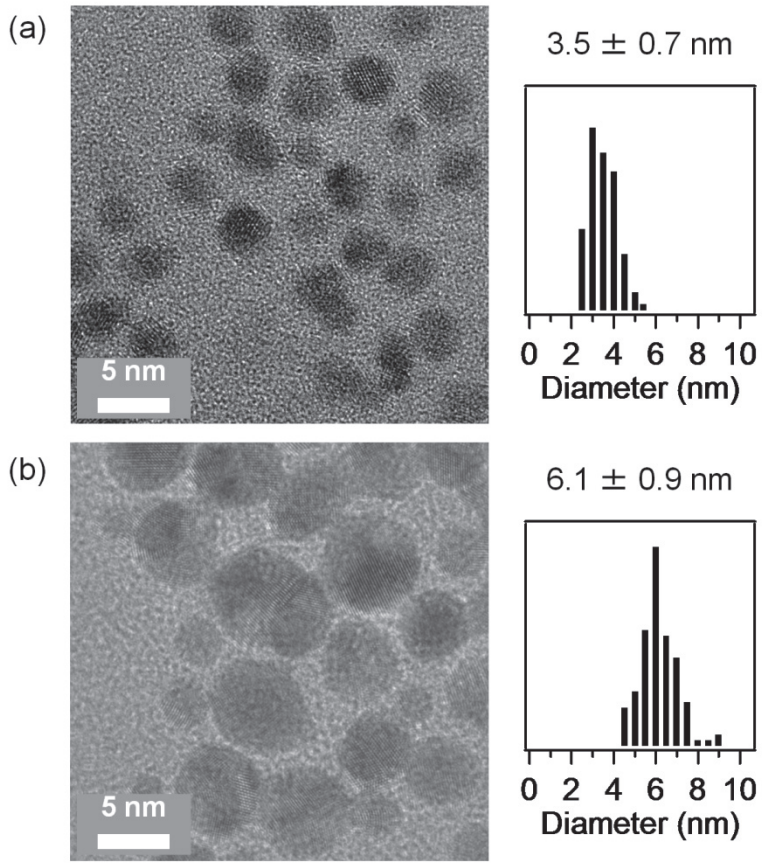

Figure 3. TEM images of **GN@1** (a) and **GN@2** (b) with histograms of particle size in the right. The initial S to Au ratio = 1 for both cases.

decreased as observed for **GN@1**, but was larger than those of **GN@1** when compared at the same value of ξ. We also prepared dodecanethiol-protected gold nanoparticles **GN@3** by the one-phase method, since dodecanethiol is known to stabilize gold nanoparticles by forming a closely packed self-assembled monolayer and would give smaller gold nanoparticles. In fact, however, the size of **GN@3** was larger than that of **GN@1** at every value of ξ, i.e. larger by 1.0 nm at ξ = 16. Thus, the passivant ligand **1** tends to produce smaller gold nanoparticles than monodentate passivant **2** and dodecanethiol. Although at this moment we cannot address exact mechanisms concerning how **1** determines the particle size, probably the relatively large porphyrin moiety of **1** may play a role in producing smaller gold nanoparticles.[20]

To inspect the chemical status of the four S atoms of **GN@1**, X-ray photoelectron spectroscopy (XPS) measurements were carried out. Figure 5a shows S(2p) region of the XPS spectrum of **GN@1** prepared at ξ = 1, together with that for **1** for comparison. In the case of **GN@1**, S(2p) peaks were observed at the binding energy of 163 eV, together with a very weak peak at 170 eV. The latter peak is assignable to sulfur oxide (SO_x) of the impurities derived from **1**.[7,21] On the other hand, the main peak at 163 eV is ascribed to the alkanethiol

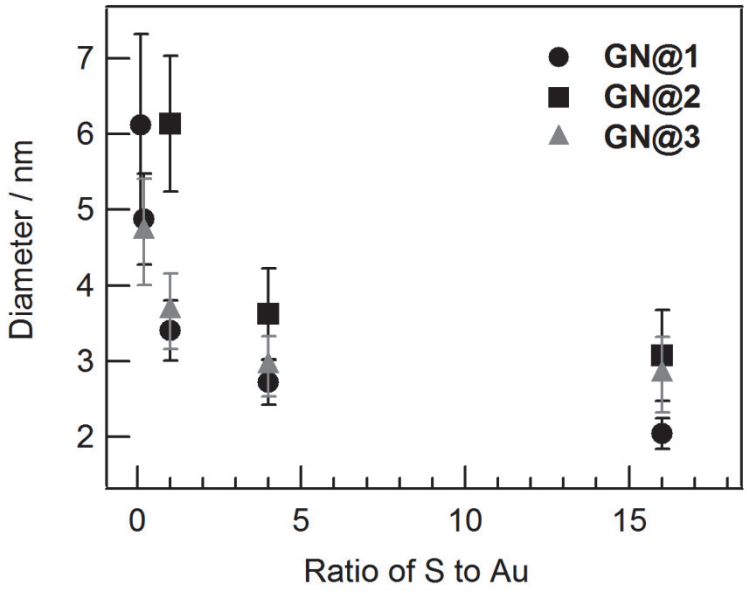

Figure 4. Plots of the mean diameter of gold nanoparticles against the initial S to Au ratio.

bound to Au, judged from reported values for other alkanethiol-monolayer-protected gold nanoparticles.[7,22] Importantly, there was no peak at 164 eV that was observed for acetyl-protected S atoms of **1**. Similar spectrum was obtained with **GN@2**. Thus, these results indicate that **1** attached with the gold nanoparticle surface via four S−Au bonds, where the S atoms lack acetyl groups and exist as thiolate anions (Figure 6). Therefore, it is conclusive that the porphyrin plane of **1** orients in a plane parallel to the gold surface, as we designed. Such a horizontal monolayer formation of **1** on gold surface is in agreement with the red-shifted Soret band of **GN@1** (*vide supra*).

Figure 5(c, d) shows XPS spectra of Au(4f) core levels. The XPS spectra exhibited an Au 4f7/2 level with a binding energy of 84.9 eV and 85.3 eV for GN@1 and GN@2, respectively. These binding energies are higher than that observed for dodecanethiol-protected gold nanoparticles (83.8 eV).[10,22,23] and for bulk gold (84.0 eV). These results indicate that the gold cores of **GN@1** and **GN@2** were positively charged. In the case of **GN@1**, but not of **GN@2,** a shoulder peak was observed at around 84 eV that indicates the existence of neutral charged **GN@1** as a minor fraction. Although such positively charged thiol-protected gold nanoparticles are rarely known, Tsukuda and co-workers recently reported that chemical oxidation of $[Au_{25}(SC_6H_{13})_{18}]^0$ produced the corresponding positively charged gold nanoclusters.[24]

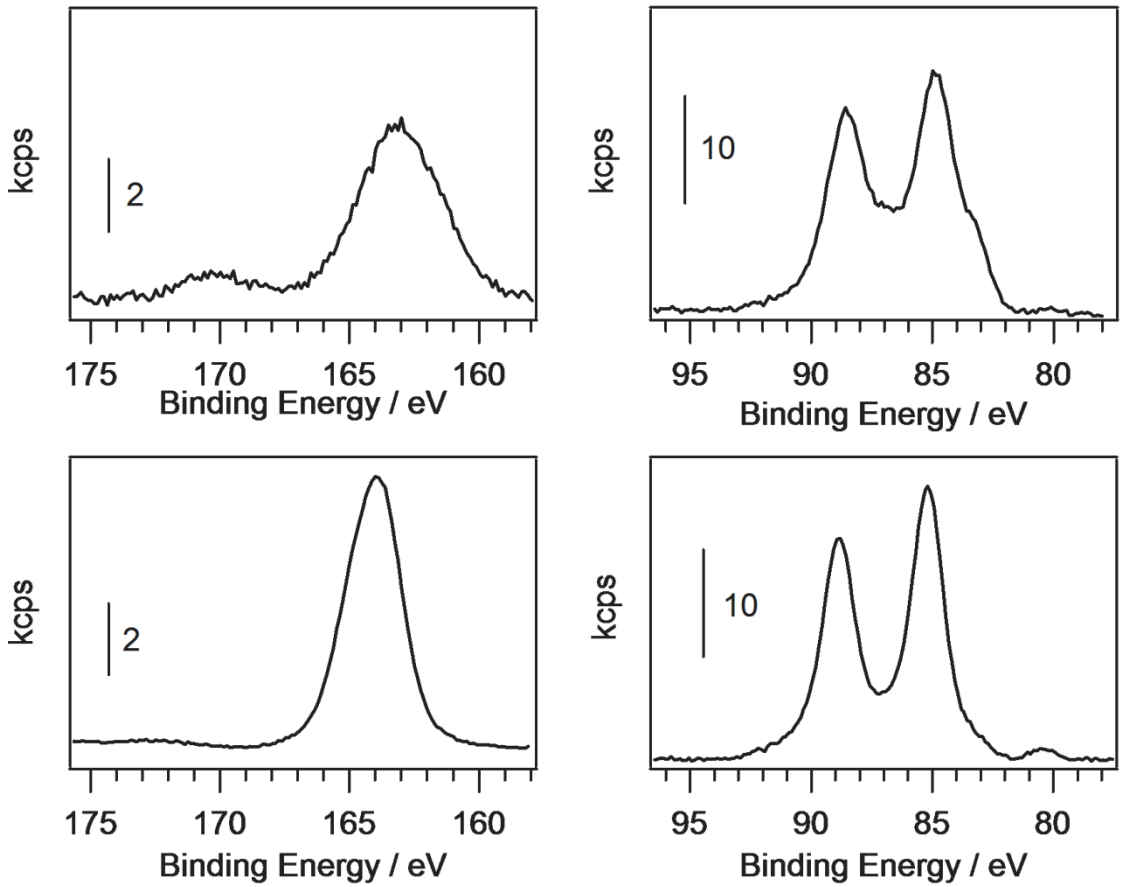

Figure 5. XPS spectra of S(2p) core level of **GN@1** (a) and **1** (b) and Au(4f) core level of **GN@1** (c) and **GN@2** (c).

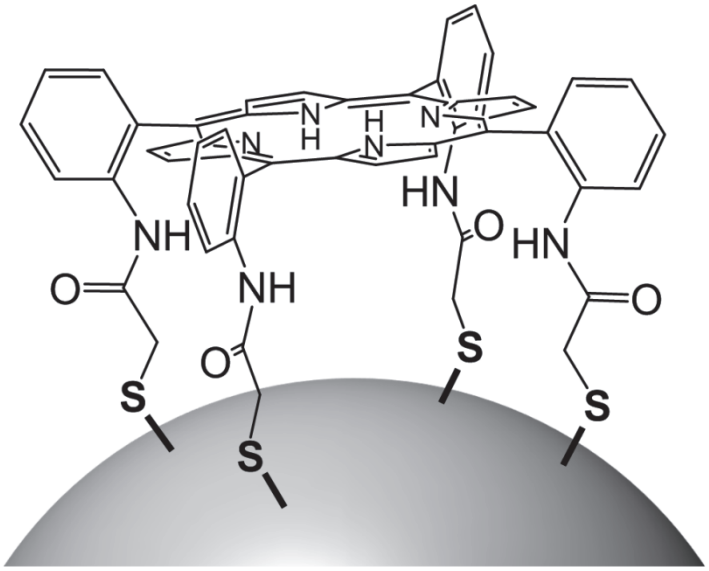

Figure 6. Plausible structure of **GN@1**.

Conclusion

We have synthesized stable gold nanoparticles coated by a porphyrin monolayer by one-phase reduction of $HAuCl_4$ in DMF in the presence of a specially designed porphyrin-cored tetradentate passivant **1**. Our tetradentate passivant **1** reasonably affords a horizontal porphyrin monolayer on gold nanoparticles thanks to the four S atoms extending in the same direction. In addition, the systematic synthesis of gold nanoparticles at different values of ξ revealed that the new tetradentate passivant **1** gives smaller gold nanoparticles than monodentate ligands can. Thus, our studies demonstrated that highly functionalized multidentate passivants such as **1** are promising not only to control the size of gold nanoparticles, but also to introduce functional molecules on the gold surface with well-defined orientation.

References

(1) (a) Daniel, M.-C.; Astruc, D. *Chem. Rev*. **2004**, *104,* 293; (b) Turkevich, J.: Hillier, *J, Anal. Chem.* **1949**, *21*, 475–485; (c) Turkevich, J.: Stevenson, P. C.; Hillier, J. *Discuss. Faraday Soc.* **1951**, 55; (d) Enustun, B. V.; Turkevich, J. *J. Am. Chem. Soc.* **1963**, *85*, 3317–3328; (e) Schmid, G. *Chem. Rev.* **1992**, *92*, 1709–1727; (f) Gross, S. *Colloidal Dispersion of Gold Nanoparticles in Material Syntheses, Springer-Verlag, Wien, 2008.*

(2) Love, J. C.; Estroff, L. A.; Kriebel, J. K.; Nuzzo, R. G.; Whitesides, G. M. *Chem. Rev.* **2005**, *105*, 1103.

(3) Drechsler, U.; Erdogan, B.; Rotello, V. M. *Chem.-Eur. J.* **2004**, *10*, 5570.

(4) Beer, P. D.; Cormode, D. P.; Davis, J. J. *Chem. Commun.* **2004**, 414.

(5) Balasubramanian, R.; Kim, B.; Tripp, S. L.; Wang, X.; Lieberman, M.; A., W. *Langmuir* **2002**, *18*, 3676.

(6) Zhang, S. S.; Leem, G.; Srisombat, L. O.; Lee, T. R. *J. Am. Chem. Soc.* **2008**, *130*, 113.

(7) Kanehara, M.; Kodzuka, E.; Teranishi, T. *J. Am. Chem. Soc.* **2006**, *128*, 13084.

(8) Kanehara, M.; Takahashi, H.; Teranishi, T. *Angew. Chem. Int. Ed.* **2008**, *47*, 307.

(9) Takahashi, H.; Kanehara, M.; Teranishi, T. *J. Photopoly. Sci. Technol.* **2007**, *20*, 133.

(10) Brust, M.; Walker, M.; Bethell, D.; Schiffrin, D. J.; Whyman, R. *J. Chem. Soc., Chem. Commun.* **1994**, 801.

(11) Yamada, M.; Kuzume, A.; Kurihara, M.; Kubo, K.; Nishihara, H. *Chem. Commun.* **2001**, 2476.

(12) Collman, J. P.; Gagne, R. R.; Reed, C.; Halbert, T. R.; Lang, G.; Robinson, W. T. *J. Am. Chem. Soc.* **1975**, *97*, 1427.

(13) For gold nanoparticles with a vertical porphyrin monolayer, see, (a) Akiyama, T.; Nakada, M.; Terasaki, N.; Yamada, S. *Chem. Commun,* **2006**, 359-397; (b) Imahori, H.; Fujimoto, A.; Kang, S.; Hotta, H.; Yoshida, K.; Umeyama, T.; Matano, Y.; Isoda, S.; Isosomppi, M.; Tkachenko, N. V.; Lemmeyinen, H. *Chem.-Eur. J.* **2005**, *11*, 7265-7275; (c) Hasobe, T.; Imahori, H.; Kamat, P. V.; Ahn, T. K.; Kim, S. K.; Kim, D.; Fujimoto, A.; Hirakawa, T.; Fukuzumi, S. *J. Am. Chem. Soc.* **2005**, *127*, 1216-1228.

(14) For horizontal porphyrin coverage over gold crystal surface, see, (a) Éll, A. H.; Csjernyik, G.; Slagt, V. F.; Bäckvall, J.-E.; Berner, S.; Puglia, C.; Ledung, G.; Oscarsson, S. *Eur. J. Org. Chem.* **2006**, 1193-1199; (b) Berner, S.; Lidbaum, H.; Ledung, G.; Ahlund, J.; Nilson, K.; Schiessling, J.; Gelius, U.; J. Backvall, E.; Puglia, C.; Oscarsson, S. *Applied Surface Science* **2007**, *253*, 7540-7548; (c) Berner, S.; Biela. S.; Ledung, G.; Gogoll, A.; Backvall, J.E.; Puglia, C.; Oscarsson, S. *J. Catal.* **2006**, *244*, 86-91.

(15) For a gold nanocluster non-covalently trapped within a hexaporphyrin cage, see, Inomata, T.; Konishi, K. *Chem. Commun.* **2003**, 1282-1283.

(16) Lindsey, J. *Journal of Organic Chemistry* **1980**, *45*, 5215.

(17) Abraham, R. J.; Hawkes, G. E.; Hudson, M. F.; Smith, K. M. *Journal of the Chemical Society-Perkin Transactions 2* **1975**, 204.

(18) Barber, D. C.; Freitagbeeston, R. A.; Whitten, D. G. *J. Phys. Chem.* **1991**, *95*, 4074.

(19) Frenkel, A. I.; Nemzer, S.; Pister, I.; Soussan, L.; Harris, T.; Sun, Y.; Rafailovich, M. H. *J. Chem. Phys.* **2005**, *123*, 184701.

(20) Yonezawa, T.; Yasui, K.; Kimizuka, N. *Langmuir* **2001**, *17*, 271.

(21) Wirde, M.; Gelius, U.; Nyholm, L. *Langmuir* **1999**, *15*, 6370.

(22) Hostetler, M. J.; Wingate, J. E.; Zhong, C.-J.; Harris, J. E.; Vachet, R. W.; Clark, M. R.; Londono, J. D.; Green, S. J.; Stokes, J. J.; Wignall, G. D.; Glish, G. L.; Porter, M. D.; Evans, N. D.; Murray, R. W. *Langmuir* **1998**, *14*, 17.

(23) Tanaka, A.; Takeda, Y.; Imamura, M.; Sato, S. *Physical Review B* **2003**, *68*, 195415.

(24) Negishi, Y.; Chaki, N. K.; Shichibu, Y.; Whetten, R. K.; Tsukuda, T. *J. Am. Chem. Soc.* **2007**, *127*, 11322.

Chapter 2

Efficient Capping of Growing Gold Nanoparticles by Porphyrin Having Two Disulfide Straps over One Face

Abstract

Two types of tetrathiolated surface passivants were synthesized in order to explore the effect of S-functional groups (disulfide vs. S-thioester) to control the size of gold nanoparticles prepared by a simple one-pot reduction of tetrachloroaurate with sodium tetrahydroborate. Both the passivants have four thiolated arms in the same direction perpendicular to a porphyrin plane, and produced small porphyrin-coated gold nanoparticles 2 to 4nm in size by one-pot reduction of Au^{III} ions at S/Au from 1 to 16. The constancy in particle size at S/Au ratio less than 4 was greater with use of tetradentate disulfide passivant compared with use of tetradentate S-thioester ligand, which should be attributed to faster adsorption of disulfide groups with gold than that of S-thioester groups. The results described here suggest that passivants having multivalent disulfide bonds should be promising candidates for constructing monolayer-protected gold nanoparticles of well-defined size.

Introduction

Nanosized gold particles have attracted increasing attention because they display unique properties that are not observed in bulk gold, such as distinctive extinction bands in the visible region and catalytic activities.[1-3] The properties are highly dependent on particle size; therefore, substantial efforts have been made to develop methods of preparing gold nanoparticles with a desired size. In general, small gold nanoparticles or nanoclusters have been prepared by reduction of gold ions in presence of polymers or high-surface-area metal oxides; these adsorbents suppress growth and agglomeration of gold nanoparticles owing to their weak but numerous interaction points with gold. The use of a large excess of surface passivants such as 1-dodecanethiol is another strategy to synthesize gold nanoparticles with a controlled small particle size.[3-9] In this case, the initial molar ratio of alkanethiols and gold ions is crucial to determining the particle size; increasing the molar ratio decreases the particle size.[8,10] The resulting monolayer-protected gold nanoparticles are attractive in designing nanoscale devices such as memory devices, sensors, and catalysts because of their ability to introduce various types of functional molecules.[13,11,17]

The use of surface passivants that can afford multiple Au-S interactions has been employed by several groups in effort to stabilize gold nanoparticles. Jutzi and co-workers improved the exchange stability of thiolate ligands on gold nanoparticles using a tridentate alkanethiol, 1,1,1-tris(mercaptomethyl)-undecane.[18] Lee and co-workers reported that bidentate and particular tridentate alkanethiols inhibit the aggregation of large gold nanoparticles in organic solvents.[19-21] Wei and co-workers succeeded in stabilization of large gold nanoparticles up to 87 nm using resorcinarene tetrathiols.[22] Mayor, Simon, and coworkers have synthesized a series of linear oligomeric multidentate thioether ligands, and demonstrated the advantage of multidentate ligands in enwrapping and stabilizing gold nanoparticles with diameters below 2 nm, which become more stable with increasing the number of the thioether groups.[23] Kanehara and co-workers reported that porphyrin derivatives having four thioester groups, tetrakis-5,10,15,20-(2-acetylthiophenyl)-porphyrin, **SC_0P**, and tetrakis-5,10,15,20-(2-acetylthiomethylphenyl) porphyrin, **SC_1P**, can stabilize gold nanoparticles even under the ligand-exchange conditions.[17] Thus, multidentate ligands

have been shown to be able to stabilize gold nanoparticles in an effective manner. Recently, we reported the synthesis of a tetradentate surface passivant $\mathbf{1}^{\mathbf{SAc}}$ holding up four S-thioester arms in the same direction perpendicular to a porphyrin plane in order to introduce porphyrin molecules in a well-defined orientation on a gold surface (Scheme 1).[24] The porphyrin $\mathbf{1}^{\mathbf{SAc}}$ has a structure related to Kanehara's porphyrins, $\mathbf{SC_nP}$. The porphyrins $\mathbf{SC_nP}$ are a mixture of four atropisomers, but $\mathbf{1}^{\mathbf{SAc}}$ has only a stable $\alpha,\alpha,\alpha,\alpha$ -atropisomer. This advantage enables us to synthesize porphyrin-coated gold nanoparticles through one-pot reduction at room temperature.[17,24] Reduction of a DMF solution containing a 1:4 molar ratio of Au^{III} ions and $\mathbf{1}^{\mathbf{SAc}}$ affords ca. 2-nm gold nanoparticles, which is significantly smaller than those prepared using 1-dodecanethiol instead of $\mathbf{1}^{\mathbf{SAc}}$ at the same molar ratio of S atoms and Au^{III} ions.[24] This result suggests that multidentate passivants not only stabilize gold nanoparticles but also would provide a unique opportunity to alter the nucleation and growth processes of gold nanoparticles. Herein, we synthesized a new porphyrin-based passivant $\mathbf{2}^{\mathbf{SS}}$ which can give small gold nanoparticles at much smaller molar ratio of S atoms and Au ions than the previously reported passivant $\mathbf{1}^{\mathbf{SAc}}$.

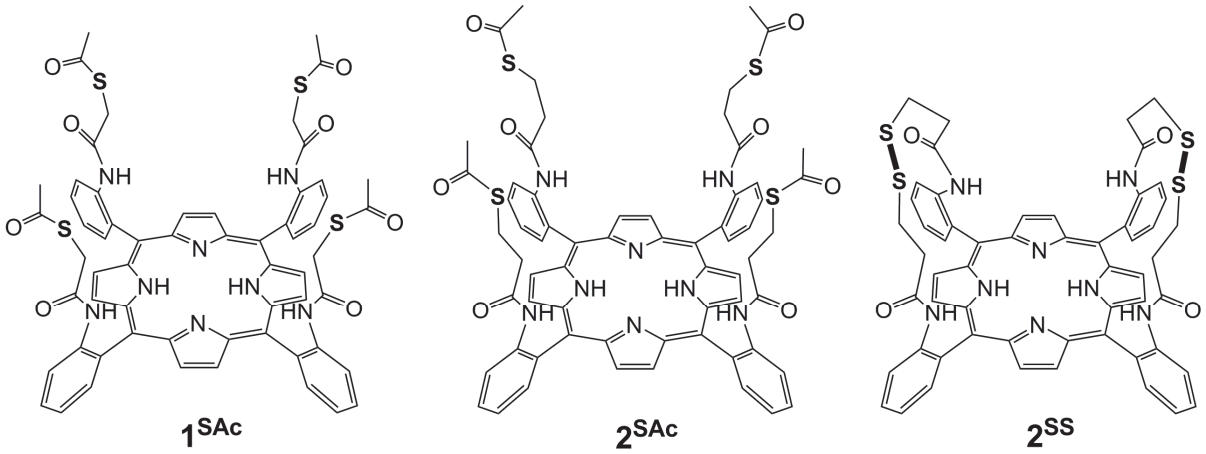

Scheme 1. Structures of porphyrin-based passivants.

Experimental

Materials. 2-Nitrobenzaldehyde, pyrrole, *N,N*-diethylaniline, and thioacetic acid were purchased from Tokyo Chemical Industry (Tokyo, Japan), and the other chemicals and solvents were from Wako Pure Chemical Industry (Osaka, Japan).

Instrumentation. Electronic absorption spectra were measured on a HITACHI U-3500 UV-VIS-NIR spectrometer by using a quartz cell with a 1-cm path length. ^{1}H, ^{13}C, 2D (HMQC, HMBC) NMR spectra were measured in $CDCl_3$ (expect for $\mathbf{2}^{SS}$) and DMSO-d_6 ($\mathbf{2}^{SS}$) on a JEOL JNMECX400 spectrometer. Transmission electron microscopy (TEM) images were taken with a JEOL JEM-100SX operating at an accelerating voltage of 100 kV and a JEOL JEM-2100F operating at an accelerating voltage of 200 kV. TEM samples were prepared by depositing drops of a methanol solution onto a carbon-coated copper grid (Okenshoji Co.) and dried at room temperature. At least 200 particles were measured to determine the mean diameter. X-ray photoelectron spectroscopy (XPS) measurement was performed using an ULVAC PHI 5500MT. XPS samples were mounted on an indium foil and the spectra were measured using Mg$K\alpha$ radiation (15 kV, 400 W) in a chamber with the base pressure of ca. 1×10^{-8} Torr. The takeoff angle was set at 45°. All binding energies were corrected for charge shifting by referencing to the C(ls) line from the adventitious carbon at 284.6 eV.

Synthesis of $\mathbf{2}^{SAc}$. To a solution of α,α,α,α-5,10,15,20-tetrakis(o-acrylamidophenyl) porphyrin[25] (0.212 g, 0.238mmol) in dry CH_2Cl_2 (2 mL) were thioacetic acid (210 μL, 2.95mmol) and dry triethylamine (60 μL, 0.430mmol) added. After the solution was stirred for 2 h at room temperature, the solvent was removed under reduced pressure. The residue was purified by column chromatography on silica gel eluted with 3 vol% MeOH in $CHCl_3$ and subsequent recrystallization from $CHCl_3$/MeOH to afford $\mathbf{2}^{SAc}$ (64%). TLC: R_f = 0.32 ($CHCl_3$:MeOH = 30:1); HRMS-FAB (*m/z*): $[M + H]^+$ calcd for $C_{64}H_{59}O_8N_8S_4$, 1194.3260; found, 1194.3302; 1HNMR (CDCl3, 400 MHz): δ 8.81 (s, 8H), 8.65 (d, J = 7.5 Hz, 4H), 7.93 (d, J = 8.0 Hz, 4H), 7.87-7.82 (m, 4H), 7.54-7.52 (m, 4H), 7.12 (s, 4H), 2.55 (brs, 8H), 1.71

(brs, 8H), 1.60 (s, 12H), 12.73 (s, 2H); ^{13}CNMR ($CDCl_3$, 100 MHz): 195.6, 165.9, 138.2, 135.1, 131.8, 131.4, 130.1, 123.6, 122.1, 115.2, 36.0, 30.0, 24.5 (The meso-carbon atoms could not be observed, presumably due to NH tautomerism.[26]); UVvis λ_{max} in DMF: 423, 517, 550, 591, 648 nm.

Synthesis of 2^{SS}. To a solution of $\mathbf{2}^{SAc}$ (0.100 g, 0.0837 mmol) in THF (100 mL) was 25% NH_3 aq. (13 mL) added. After the mixture was stirred for 1 day at room temperature, the solvent was removed under reduced pressure. The residue was dissolved in $CHCl_3$ and washed with water. The aqueous phase was washed with $CHCl_3$ and all the organic phase was collected. The organic phase was dried over Na_2SO_4, and filtered to be concentrated under reduced pressure. The residue was purified by column chromatography on silica gel eluted with 9 vol% CH_3OH in $CHCl_3$ and subsequent recrystallization from $CHCl_3$/MeOH to afford $\mathbf{2}^{SS}$ (65%). TLC: R_f = 0.48 ($CHCl_3$:MeOH = 10:1); HRMS-FAB (*m/z*): $[M]^+$ calcd for $C_{56}H_{46}O_4N_8S_4$, 1022.2525; found, 1022.2523; ^{1}HNMR (DMSO-d_6, 400 MHz): δ 8.73 (s, 8H), 8.64 (s, 4H), 8.34 (d, J = 8.0 Hz, 4H), 7.877.81 (m, 8H), 7.567.52 (m, 4H), 2.272.09 (m, 8H), 2.061.79 (m, 8H), 2.73 (s, 2H); ^{13}CNMR (DMSO-d_6, 100 MHz): . 168.8, 138.0, 135.8, 133.3, 131.0, 129.1, 123.5, 123.2, 115.4, 34.6, 32.3 (The meso-carbon atoms, Cl, could not be observed, presumably due to NH tautomerism.[26]); UVvis λ_{max} in DMF: 423, 516, 551, 593, 649 nm.

X-ray Structure Determination of Zinc Complex of 2^{SS}. Crystals for X-ray analysis were grown by the slow diffusion of methanol into a chloroform solution of zinc complex of $\mathbf{2}^{SS}$, **Zn-2^{SS}**, which was prepared by reacting $\mathbf{2}^{SS}$ with $Zn(OAc)_2$ in $CHCl_3$ at room temperature. $C_{57}H_{47}C_{l3}N_8O_5S_4Zn$, M_r = 1224.03, monoclinic, space group $P2_1/c$ (No. 14), a = 13.2277(7), b = 26.6609(14), c = 16.2075(8) Å, $\alpha = \gamma = 90°$, β = 107.5754(14)°, V = 5449.0(5) Å^3, Z = 4, μ(MoK_α) = 0.378 mm^{-1}. Data collection ($6.06 < 2\theta < 55.24°$) was performed at 243K using a Rigaku CCD diffractometer (MoK_α, λ = 0.71070 Å). The structure was solved using direct methods and refined by a full-matrix least-squares method, giving a final R_1 value of 0.0755 for 768 parameters and 12444 unique reflections with $I > 2\sigma(I)$ and wR_2 of 0.1526 for all

12444 reflections. All non-hydrogen atoms and hydrogen atoms were anisotropically and isotropically refined, respectively. Crystallographic data have been deposited with Cambridge Crystallographic Data Centre: Deposition number CCDC-775279 for **Zn-2^{SS}**. Copies of the data can be obtained free of charge via http://www.ccdc.cam.ac.uk/conts/retrieving.html (or from the Cambridge Crystallographic Data Centre, 12, Union Road, Cambridge, CB2 1EZ, U.K.; Fax: +44 1223 336033; e-mail: deposit@ccdc.cam.ac.uk).

Gold Nanoparticles Covered with 2^{SAc}, GN@2^{SAc}. To a solution of **2^{SAc}** (18.0 mg, 15.0 μmol at ξ = 1 or 1.8 mg, 1.50 μmol at ξ = 0.1, in which ξ denotes the S/Au ratio) in DMF (292 mL) in a 500mL round-bottom flask which was cleaned with piranha solution was added a 20.5 μM $HAuCl_4$ solution in DMF (0.5 mL). Then, the mixture was reduced with $NaBH_4$ (27.34 mg, 723 μmol) dissolved in DMF (7 mL). After stirring for 1.5 h, the reaction mixture was evaporated to ca. 3mL and precipitated with 30 mL of methanol to remove excess **2^{SAc}** and any salts. The precipitate was dissolved in DMF (3 mL) and precipitated again by adding $CHCl_3$ (30 mL). The reprecipitation process was repeated four times. The pure **GN@2^{SAc}** was characterized by TEM, UVvis, and XPS measurements.

Gold Nanoparticles Covered with 2SS, GN@^{2SS}. GN@^{2SS} was prepared under the identical conditions to **GN@2^{SAc}**.

Size-Controlled Synthesis of Gold Nanoparticles. Gold nanoparticles were synthesized in the presence of **2^{SAc}** and **2^{SS}** under various molar ratios (S/Au = 0, 0.1, 0.2, 1, 4, and 16). All of glass vials for the syntheses of gold nanoparticles were cleaned with piranha solution. A typical method is as follows; an 1.0mM solution of **2^{SAc}** in DMF (8 mL, 8.00 μmol), a 153.7mM solution of $HAuCl_4$ in DMF (13.0 μL, 2.00 μmol) and 1.8mL of DMF were added to a reaction vessel. While the mixture was vigorously stirring, 100 μL of 241mM $NaBH_4$ (24.1mmol) was swiftly added and then stirred for 1 h. The solutions were evaporated and the residue was dispersed in MeOH.

Results and Discussion

Design and Synthesis of New Passivants. The previously reported porphyrin-based surface passivant $\mathbf{1}^{\mathbf{SAc}}$ has four S-thioester groups, but the XPS analysis indicated that the S atoms lack acetyl groups and exist as thiolate anions on a gold surface.[24] S-Thioester groups do not adsorb onto a gold surface rapidly compared to the corresponding thiol functional groups.[27,28] Therefore, we tried to deprotect the acetyl groups of $\mathbf{1}^{\mathbf{SAc}}$ in an attempt to realize more efficient capping of small gold nanoparticles. Unfortunately however, we failed to isolate any monomeric porphyrin compounds, instead always obtaining insoluble polymers, probably due to the formation of intermolecular disulfide bonds.[29] We then designed a new porphyrin-based passivant $\mathbf{2}^{\mathbf{SAc}}$ that has a structure similar to $\mathbf{1}^{\mathbf{SAc}}$ except for one more methylene in each arm (Scheme 1). Ligand $\mathbf{2}^{\mathbf{SAc}}$ was synthesized by Michael reaction of α,α,α,α-5,10,15,20-tetrakis(2-acryloylaminophenyl)porphyrin[24] and potassium thioacetate. Mild hydrolysis of $\mathbf{2}^{\mathbf{SAc}}$ followed by aeration nearly quantitatively yielded monomeric porphyrin compound $\mathbf{2}^{\mathbf{SS}}$, which has two disulfide bonds over one face of the porphyrin plane (Scheme 1). The C_2 symmetric structure of $\mathbf{2}^{\mathbf{SS}}$ was confirmed by ^{1}H and ^{13}CNMR measurements and by X-ray crystal structure analysis of the corresponding zinc complex (Figure 1).

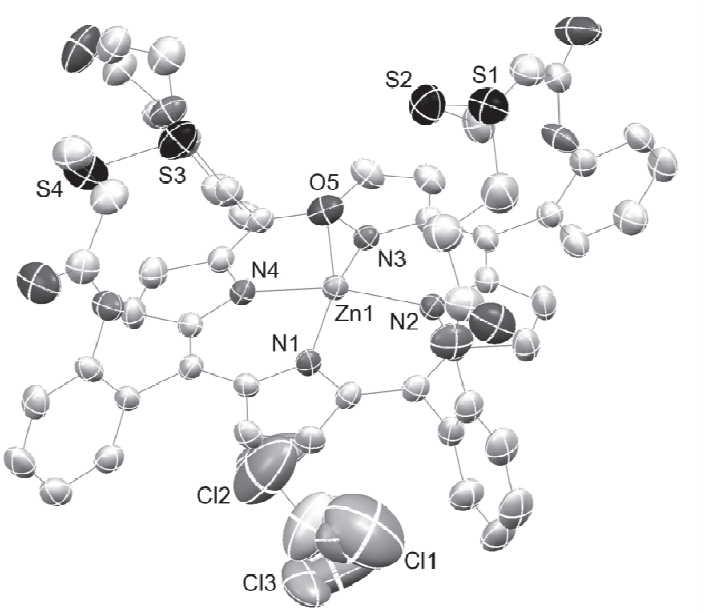

Figure 1. An ORTEP drawing of the zinc complex of $\mathbf{2}^{\mathbf{SS}}$ ($[Zn(\mathbf{2}^{\mathbf{SS}})(H_2O)]\cdot CHCl_3$) showing 50% probability thermal ellipsoids. The hydrogen atoms are omitted for clarity. Selected bond lengths/Å: S(1)-S(2) = 2.021(2), S(3)-S(4) = 2.020(4), Zn(1)-N(1) = 2.058(3), Zn(1)-N(2) = 2.081(4), Zn(1)-N(3) = 2.062(3), Zn(1)-N(4) = 2.069(4), Zn(1)-O(5) = 2.114(5).

Preparation and Absorption Spectra of Gold Nanoparticles. Porphyrin-coated gold nanoparticles were synthesized by $NaBH_4$ reduction of $HAuCl_4$ in a DMF solution containing $\mathbf{2}^{\mathbf{SAc}}$ or $\mathbf{2}^{\mathbf{SS}}$ at an S/Au ratio (ξ) of 1, hereafter called $\mathbf{GN@2}^{\mathbf{SAc}}$ or $\mathbf{GN@2}^{\mathbf{SS}}$, respectively. Both $\mathbf{GN@2}^{\mathbf{SAc}}$ and $\mathbf{GN@2}^{\mathbf{SS}}$ were purified by repeated precipitation with methanol and chloroform, as previously reported for $\mathbf{GN@1}^{\mathbf{SAc}}$.[23] The UVvis spectra of $\mathbf{2}^{\mathbf{SAc}}$ and $\mathbf{2}^{\mathbf{SS}}$ were nearly identical (Figure 2A), but the gold nanoparticles prepared with them showed different features in the absorption spectra especially in surface plasmon bands. The UVvis spectrum of purified $\mathbf{GN@2}^{\mathbf{SAc}}$ in a DMF solution showed a Soret band at 426.0nm and a relatively weak, broad surface plasmon band at around 545 nm, which is very close to that of $\mathbf{GN@1}^{\mathbf{SAc}}$.[23] On the other hand, purified $\mathbf{GN@2}^{\mathbf{SS}}$ displayed an intense Soret band at 426.4 nm, but the surface plasmon band was fairly weak in intensity compared to those of

GN@1$^{\mathbf{SAc}}$ and **GN@2**$^{\mathbf{SAc}}$ (Figure 2B). These results suggest that disulfide passivant **2**$^{\mathbf{SS}}$ should afford smaller gold nanoparticles than S-thioester passivants **1**$^{\mathbf{SAc}}$ and **2**$^{\mathbf{SAc}}$ under identical conditions. Although Kanehara and co-workers reported that the molar absorption coefficients of the Soret bands for **SC$_n$P** decrease by one order of magnitude upon coordination onto the gold nanoparticles,[17] **GN@2**$^{\mathbf{SS}}$ did not show such a large decrease in the intensity of the Soret band ($\varepsilon_{\mathrm{Soret}} = 3.4 \times 10^5$ and 1.1×10^5 $\mathrm{M^{-1}cm^{-1}}$ for **2**$^{\mathbf{SS}}$ and **GN@2**$^{\mathbf{SS}}$ in DMF, respectively, where the latter value was obtained by subtracting the surface plasmon band derived from gold nanoparticles), indicating weaker interactions between **2**$^{\mathbf{SS}}$ and gold nanoparticles due to the longer arms of **2**$^{\mathbf{SS}}$ than **SC$_n$P**.

Next, we prepared gold nanoparticles under more severe conditions, that is, at ξ = 0.1 (Figure 2C). Under this condition, reduction of $HAuCl_4$ gave a clear red solution in both cases. A DMF solution of purified **GN@2**$^{\mathbf{SAc}}$ (ξ = 0.1) showed a much more intense surface plasmon band at ca. 562 nm than that of **GN@2**$^{\mathbf{SAc}}$ (ξ = 1), but the UVvis spectrum of **GN@2**$^{\mathbf{SS}}$ (ξ = 0.1) did not differ greatly from that of **GN@2**$^{\mathbf{SS}}$ (ξ = 1). This result indicated that the particle size of **GN@2**$^{\mathbf{SAc}}$ increased with a decrease in the ratio of initially used S to Au (ξ), but that the particle size of **GN@2**$^{\mathbf{SS}}$ was nearly constant despite the changing ξ value.

Particle Size. To further evaluate the ability of **2**$^{\mathbf{SS}}$ to cap small gold nanoparticles, we estimated the particle size of **GN@2**$^{\mathbf{SAc}}$ and **GN@2**$^{\mathbf{SS}}$ prepared at five different ξ values by TEM measurements. Representative TEM images of **GN@2**$^{\mathbf{SAc}}$ and **GN@2**$^{\mathbf{SS}}$ are shown in Figure 3, together with corresponding histograms of particle size distribution. Analyzed particle sizes (diameter in nm) are plotted against ξ in Figure 4. The particle size of **GN@2**$^{\mathbf{SAc}}$ decreased from 6.2 ± 1.4 nm and reached approximately 2 nm as the ξ value changed from 0.1 to 16, which is very similar to that observed for **GN@1**$^{\mathbf{SAc}}$.[23] On the other hand, the particle size of **GN@2**$^{\mathbf{SS}}$ was 3.8 ± 0.4nm even at ξ = 0.1 and reached ca. 2 nm as the ξ value increased. This clearly demonstrates that the disulfide passivant **2**$^{\mathbf{SS}}$ efficiently capped the small growing gold nanoparticles.

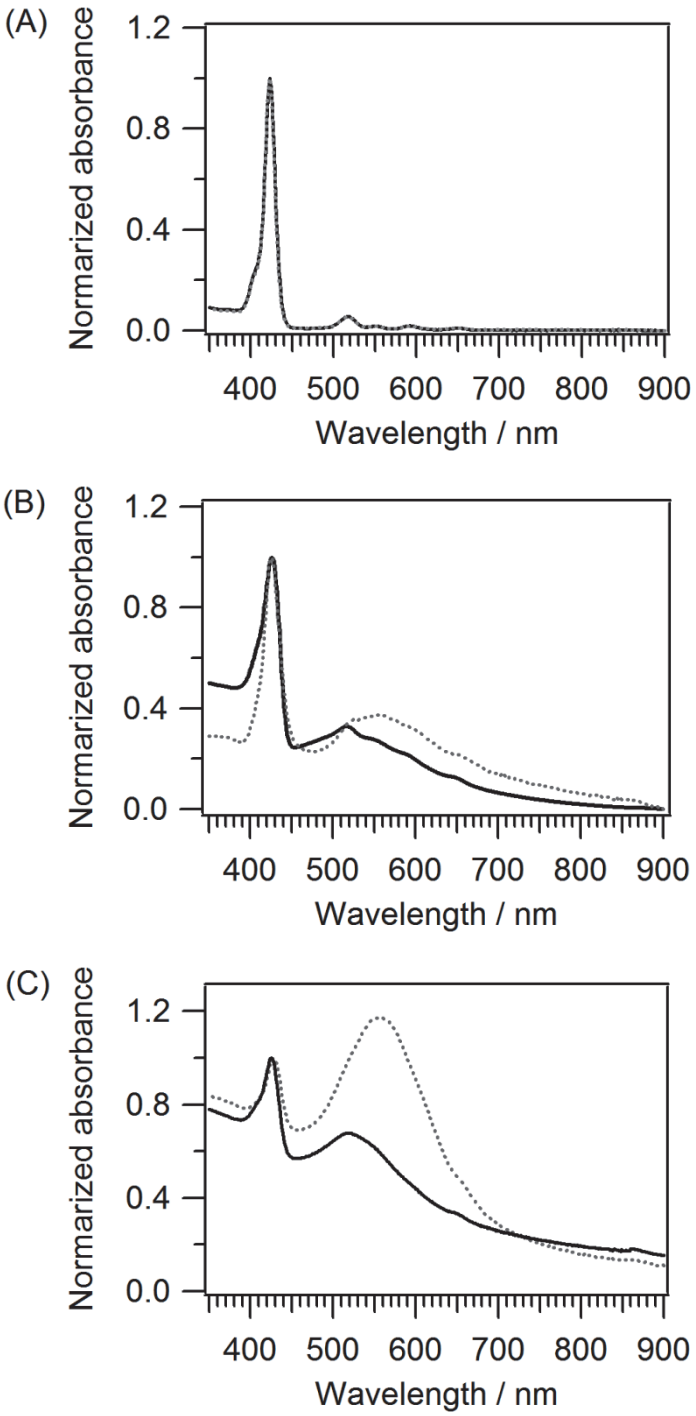

Figure 2. Absorption spectra of $\mathbf{2}^{\mathbf{SAc}}$ and $\mathbf{2}^{\mathbf{SS}}$ (A) as well as **GN@**$\mathbf{2}^{\mathbf{SAc}}$ and **GN@**$\mathbf{2}^{\mathbf{SS}}$ prepared at the initial S/Au ratio = 1 (B) and 0.1 (C) in DMF. $\mathbf{2}^{\mathbf{SAc}}$ and its derivatives are drawn in gray dotted lines and $\mathbf{2}^{\mathbf{SS}}$ and its derivatives in black solid lines.

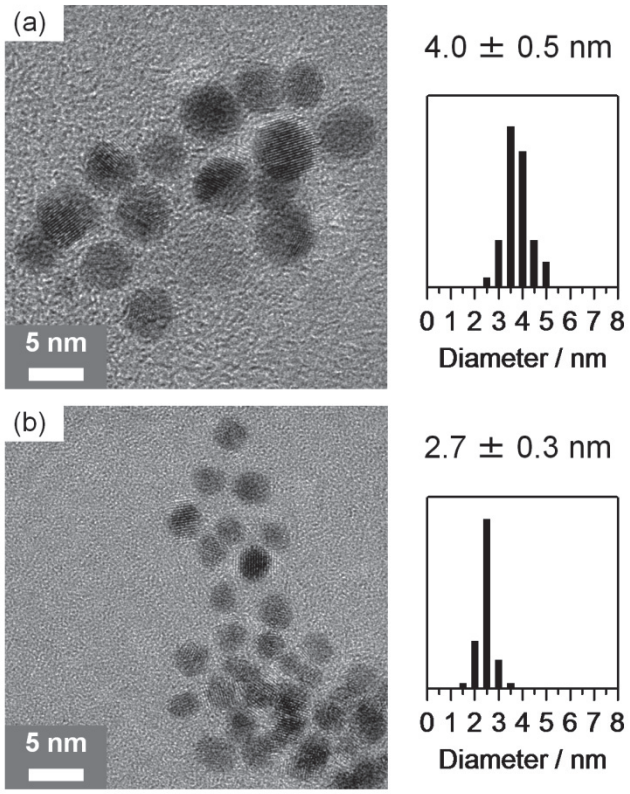

Figure 3. TEM images of **GN@2**$^{\mathbf{SAc}}$ (a) and **GN@2**$^{\mathbf{SS}}$ (b) with histograms of particle size on the right. Initial S-to-Au ratio = 1 for both cases.

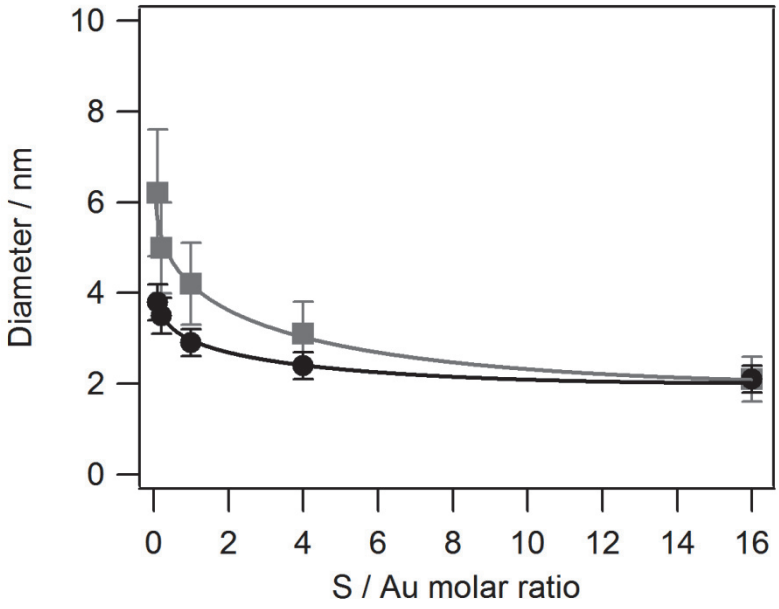

Figure 4. Mean diameter plots of gold nanoparticles **GN@2**$^{\mathbf{SAc}}$ (square) and **GN@2**$^{\mathbf{SS}}$ (circle) against the initial S-to-Au ratio.

Coverage Numbers. X-ray photoelectron spectra (XPS) of **GN@2^{SAc}** and **GN@2^{SS}** showed an S(2p) peak at the same binding energy of 163 eV, which is also the previously reported value for **GN@1^{SAc}**.[23] These results indicate that the ligands of both **2^{SAc}** and **2^{SS}** attach to gold nanoparticles via four S-Au bonds; this consequently suggests, based on the molecular structure of the ligands, horizontal orientation of the porphyrin plane to the gold surface. In the XPS experiments, we also estimated the molar ratio of S to Au of **GN@2^{SS}** by dividing the peak areas of S(2p) and Au(4f) by the respective atomic sensitivity factors;[29] we found a molar ratio of 0.12 for **GN@2^{SS}** (ξ = 1). Since one 2.7-nm gold nanoparticle is composed of ca. 598 gold atoms, the S/Au ratio of 0.12 suggests that 18 porphyrin molecules cover the gold core of **GN@2^{SS}**, which agrees well with the model in which 18 porphyrin planes of ca. 1.25 nm^2 fully covered the particle surface. Horizontal full coverage with **2^{SS}** was also supported by elemental analysis. The values for elemental analysis of **GN@2^{SS}** (H, 0.80%; C, 10.92%; N, 1.48%) also support the model there are 18 porphyrin planes on the gold surface.

Aggregation of Gold Nanoparticles. Interestingly, the TEM images showed submicrometer-sized aggregates of gold nanoparticles when a suspension of purified **GN@2^{SS}** (ξ = 1) in MeOH was cast on a TEM grid to be dried (Figure 5), although samples prepared by evaporation of a drop of a DMF solution of **GN@2^{SS}** afforded discretely distributed gold nanoparticles as shown in Figure 3. The assembly of **GN@2^{SS}** seems to have a multi-layered structure. This behavior should be caused by the hydrophobic coating and uniform size of **GN@2^{SS}**.[30-36]

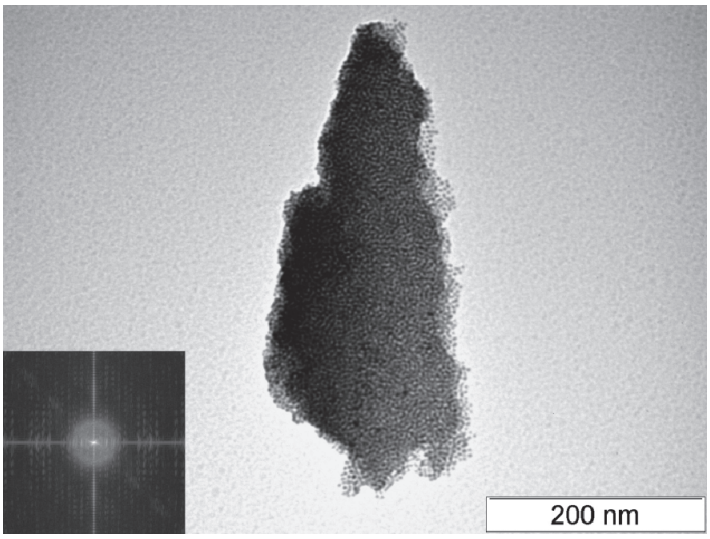

Figure 5. TEM images of submicrometer-sized assembly of **GN@2**^{SS} Inset: Fast Fourier transform of the image.

Conclusion

The constancy in particles size at S/Au ratio less than 4 was improved by the use of tetradentate disulfide passivant **2**^{SS} compared to the case of tetradentate S-thioester ligand **2**^{SAc}, which should be attributed to faster adsorption of disulfide groups with gold than that of S-thioester groups. This effect is prominent because **2**^{SS} can yield ca. 3-nm gold nanoparticles even in the presence of a large number of Au^{III} ions. The result described here suggests that passivants having multivalent disulfide bonds should be promising candidates for constructing monolayer-protected gold nanoparticles of well-defined size.

References

References

(1) Jain, P.K.; Huang, X.; El-Sayed, I. H.; El-Sayed, M. A. *Acc. Chem. Res.* **2008**, *41*, 1578.

(2) Hu, M.; Chen, J.; Li, Z.-Y.; Au, L.; Hartland, G. V.; Li, X.; Marquez, M.; Xia, Y. *Chem. Soc. Rev.* **2006**, *35*, 1084.

(3) Daniel, M.-C.; Astruc, D. *Chem. Rev.* **2004**, *104*, 293.

(4) Turkevich, J.; Stevenson, P. C.; Hillier, J. *Discuss. Faraday Soc.* **1951**, *11*, 55.

(5) Frens, G. *Nature (London), Phys. Sci.* **1973**, *241*, 20.

(6) Giersig, M.; Mulvaney, P. *Langmuir* **1993**, *9*, 3408.

(7) Brust, M.; Walker, M.; Bethell, D.; Schiffrin, D. J.; Whyman, R. *J. Chem. Soc., Chem. Commun.* **1994**, 801.

(8) Leff, D.V.; Ohara, P. C.; Heath, J. R.; Gelbart, W. M. *J. Phys. Chem.* **1995**, *99*, 7036.

(9) Hostetler, M. J.; Wingate, J. E.; Zhong, C.-J.; Harris, J. E.; Vachet, R. W.; Clark, M. R.; Londono, J. D.; Green, S. J.; Stokes, J. J.; Wignall, G. D.; Glish, G. L.; Porter, M. D.; Evans, N. D.; Murray, R. W. *Langmuir* **1998**, *14*, 17.

(10) Frenkel, A. I.; Nemzer, S.; Pister, I.; Soussan, L.; Harris, T.; Sun, Y.; Rafailovich, M. H. *J. Chem. Phys.* **2005**, *123*, 184701.

(11) Templeton, A. C.; Wuelfing, W. P.; Murray, R. W. *Acc. Chem. Res.* **2000**, *33*, 27.

(12) Inomata, T.; Konishi, K. *Chem. Commun.* **2003**, 1282.

(13) Konishi, K.; Xu, F.; Murakami, Y. *Chem. Lett.* **2006**, *35*, 476.

(14) Berner, S.; Biela, S.; Ledung, G.; Gogoll, A.; Bäckvall, J.-E.; Puglia, C.; Oscarsson, S. *J. Catal.* **2006**, *244*, 86.

(15) Beer, P. D.; Cormode, D. P.; Davis, J. J. *Chem. Commun.* **2004**, 414.

(16) Beer, P. D.; Bayly, S. R. *Top. Curr. Chem.* **2005**, *255*, 125.

(17) Kanehara, M.; Takahashi, H.; Teranishi, T. *Angew. Chem., Int. Ed.* **2008**, *47*, 307.

(18) Wojczykowski, K.; Meißner, D.; Jutzi, P.; Ennen, I.; Hütten, A.; Fricke, M.; Volkmer, D. *Chem. Commun.* **2006**, 3693.

(19) Srisombat, L.; Park, J.-S.; Zhang, S.; Lee, T. R. *Langmuir* **2008**, *24*, 7750.

(20) Zhang, S.; Leem, G.; Srisombat, L.; Lee, T. R. *J. Am. Chem. Soc.* **2008**, *130*, 113.

(21) Srisombat, L.; Zhang, S.; Lee, T. R. *Langmuir* **2010**, *26*, 41.

(22) Balasubramanian, R.; Kim, B.; Tripp, S. L.; Wang, X.; Lieberman, M.; Wei, A. *Langmuir* **2002**, *18*, 3676.

(23) Peterle, T.; Leifert, A.; Timper, J.; Sologubenko, A.; Simon, U.; Mayor, M. *Chem. Commun.* **2008**, 3438.

(24) Ohyama, J.; Hitomi, Y.; Higuchi, Y.; Shinagawa, M.; Mukai, H.; Kodera, M.; Teramura, K.; Shishido, T.; Tanaka, T. *Chem. Commun.* **2008**, 6300.

(25) Collman, J. P.; Zhang, X. M.; Herrmann, P. C.; Uffelman, E. S.; Boitrel, B.; Straumanis, A.; Brauman, J. I. *J. Am. Chem. Soc.* **1994**, *116*, 2681.

(26) Abraham, R. J.; Hawkes, G. E.; Hudson, M. F.; Smith, K. M. *J. Chem. Soc., Perkin Trans. 2* **1975**, 204.

(27) Béthencourt, M. I.; Srisombat, L.; Chinwangso, P.; Lee, T. R. *Langmuir* **2009**, *25*, 1265.

(28) Tour, J. M.; Jones, II, L.; Pearson, D. L.; Lamba, J. J. S.; Burgin, T. P.; Whitesides, G. M.; Allara, D. L.; Parikh, A. N.; Atre, S. *J. Am. Chem. Soc.* **1995**, *117*, 9529.

(29) Redman, J. E.; Sanders, J. K. M. *Org. Lett.* **2000**, *2*, 4141.

(30) Wagner, C. D.; Riggs, W. M.; Davis, L. E.; Moulder, J. M. *Handbook of X-ray Photoelectron Spectroscopy*, ed. by Muilenberg, G. E., Perkin-Elmer Co., Eden Prairie, MN, USA, 1979.

(31) *Nanoparticle Assemblies and Superstructures*, ed. by Kotov, N. A., CRC Press, Boca Raton, FL, 2005.

(32) Vignolle, J.; Tilley, T. D. *Chem. Commun.* **2009**, 7230.

(33) Yao, H.; Kojima, H.; Sato, S.; Kimura, K. *Langmuir* **2004**, *20*, 10317.

(34) Kanehara, M.; Kodzuka, E.; Teranishi, T. *J. Am. Chem. Soc.* **2006**, *128*, 13084.

(35) Wei, A. *Chem. Commun.* **2006**, 1581.

(36) Kim, B.; Tripp, S. L.; Wei, A. *J. Am. Chem. Soc.* **2001**, *123*, 7955.

Chapter 3

In Situ Observation of Nucleation and Growth Process of Gold Nanoparticles by Quick XAFS Spectroscopy

Abstract

In-situ 100-millisecond time-resolved quick X-ray absorption fine structure (QXAFS) spectroscopy was used to clarify the formation process of gold nanoparticles (AuNPs) from a toluene solution of $HAuCl_4$ by $NaBH_4$ reduction in the presence of dodecanethiol as a passivant. XAFS spectral analysis revealed that AuNPs are formed by $NaBH_4$ reduction of Au ions via very small Au nuclei; an Au_4 cluster is proposed as an example of their possible structure. The XAFS spectral analysis also elucidates the time course of the growth of AuNPs.

Introduction

Gold nanoparticle (AuNP) is one of the most attractive materials because it has unique properties that are useful in fields such as electronics, magnetics, and optics, and in the manufacturing of catalysts.[1-3] The unique properties of AuNPs can be controlled by controlling their size and shape, which is accomplished using protective agents.[2, 4, 5] Colloidal gold nanoparticles can be synthesized easily by the reduction of Au^{3+} ions in a solution containing protective agents. The most popular methods for preparing colloidal AuNPs include the reduction of Au^{3+} ions in a solution by citric acid or ascorbic acid, which also act as protective agents;[6, 7] reduction of the same by alcohol or polyol in the presence of polyvinylpyrrolidone (PVP);[8, 9] and reduction by $NaBH_4$ or KBH_4 in the presence of PVP or dodecanethiol (DT).[10, 11] Many research groups have made considerable efforts to develop new synthesis methods for AuNPs using various functional protective agents.[1, 4, 6, 12-14] Meanwhile, despite its importance, the formation process of AuNPs is still unclear; this is because there are only a few effective techniques for *in-situ* observations. Of these, Quick X-ray absorption fine structure (XAFS) spectroscopy is one of the most useful methods to observe AuNP formation process *in situ* because the chemical state and the structure of AuNP can be analyzed from the spectra.[15, 16, 17] Recently, Polte et al. observed the formation process of AuNPs with citric acid by coupled *in-situ* XANES and small-angle X-ray scattering (SAXS) spectroscopy.[18] These helped describe the mechanism of nanoparticle formation, which was found to comprise different steps of particle growth via both the coalescence of nuclei and further monomer attachment; however, the spectral analysis did not clearly reveal the formation of nuclei. On the other hand, we succeeded in observing the formation of nuclei in the solution using the *in-situ* quick XAFS spectroscopy on the BL40XU beamline in SPring-8 of the Japan Synchrotron Radiation Research Institute (JASRI; 8 GeV, 100 mA) with millisecond time resolution. Specifically, we observed the formation process of AuNPs prepared by $NaBH_4$ reduction of $HAuCl_4$ in toluene, in the presence of DT. This is one of the most popular methods used to prepare AuNPs, as represented by the Shiffrin-Brust method.[11] A series of X-ray absorption near-edge structure (XANES) spectra were analyzed to clarify the variation of the chemical state of Au atoms and the formation process of AuNPs.

Experimental

Materials. All of the solvents were purchased from Wako Pure Chemical Industries, Ltd. $HAuCl_4$, $NaBH_4$, and triphenylphosphine was purchased from Wako Pure Chemical Industries, Ltd., and DT and tetrahydrothiophene from Tokyo Chemical Industry Co., Ltd.

Instrumentation. UV-vis. spectra were corrected by using a HITACHI U-3500 UV-VIS-NIR spectrometer. TEM images were taken with a JEOL JEM-2100F operating at an accelerating voltage of 200 kV. TEM sample was prepared by depositing of drops of a methanol solution onto a carbon-coated copper grid (Okenshoji Co. LTD.) and dried at room temperature.

UV-vis. spectra of toluene solutions with a various DT/Au ratio. To 2 mL of toluene solutions of $HAuCl_4$ (20 μmol) were added 0, 2, 8, 20, 40, 80, and 320 μmol of DT, resulting in DT/Au = 0, 0.1, 0.4, 1, 2, 4, and 16 respectively. A 20 μL of each solution was added to a 2 mL of toluene in quartz cell with 1-cm optical length.

Synthesis of purified AuNPs covered with DT possessing 3.3 ± 0.5 nm diameter. AuNPs covered with DT was prepared using modification of the procedure described by Brust et al.[11] 5 mL of toluene solution of $HAuCl_4$ (50 μmol), which was transferred from H_2O to toluene using tetraoctylammoniumbromide (TOAB), was reduced by the addition of 5 mL of $NaBH_4$ aqueous solution (500 μmol) in the presence of DT (50 μmol) under vigorous stirring. After stirring for 1 h, the toluene phase was extracted and evaporated. The residue was dissolved in small amount of toluene and precipitated by addition of 100 mL of ethanol and cooling in a refrigerator. The resulting suspension was filtered off. This precipitation was repeated once more to give purified AuNPs covered with DT possessing 3.3 ± 0.5 nm diameter.

Synthesis and characterization of $Au_{11}(PPh_3)_8Cl_3$. $Au_{11}(PPh_3)_8Cl_3$ was synthesized by $NaBH_4$ reduction of $AuPPh_3Cl$ as reported by Woehrle et al.[22] $AuPPh_3Cl$ was synthesized

from $AuSC_4H_8Cl$ which was easily prepared by reduction of $HAuCl_4$ with tetrahydrothiophene (SC_2H_8).

$AuSC_4H_8Cl$ was synthesized as follows. 0.29 mmol of $HAuCl_4$ was dissolved in 0.2 mL of distilled water and 0.5 mL of ethanol. To the solution, 56 μl of SC_2H_8 (0.635 mmol) was slowly added under stirring. After stirring for 15 min, the solution was filtered off resulting in a white powder. The powder was washed with ethanol followed by evaporation. The resulting powder, $AuSC_4H_8Cl$, was used for the synthesis of $AuPPh_3Cl$ without further purification.

To a 3 mL of CH_2Cl_2 solution of $AuSC_4H_8Cl$ (0.29 mmol) was slowly added 1.8 mL of CH_2Cl_2 solution of triphenylphosphine ($P(Ph)_3$) (0.3 mmol) under stirring. After 6h, the solvent was evaporated to give 139 mg of $AuPPh_3Cl$ (0.28 mmol) as a white solid. Yield: 97%.

0.28 mmol of $AuPPh_3Cl$ in 7.5 mL of ethanol was dispersed in 7.5 mL of ethanol. After 0.28 mmol of $NaBH_4$ was slowly added to the suspension for 10 min under stirring, the suspension was stirred for 120 min. The resulting suspension was dispersed in 200 mL of hexane, and placed in a refrigerator. After filtration with membrane filter, the suspension was washed four times with 5 mL of a hexane/CH_2Cl_2 = 1 : 1 and once with 4 mL of a hexane/CH_2Cl_2 = 1 : 3. The resulting brown solid was dispersed in CH_2Cl_2 and filtered off. To the filtrate, 200 mL of hexane was added for reprecipitation. The suspension was filtered off to give 11 mg of $Au_{11}(PPh_3)_8Cl_3$ (2.5 μmol) as a orange powder. Yield: 9.8%.

XAFS measurement 2 mL of $HAuCl_4$ aqueous solution (0.129 M) and 2.58 mL of toluene was added to a round-bottomed flask, followed by the addition of tetraoctylammonium bromide (TOAB) (282 mg, 0.516 mmol), resulting in the transfer of $HAuCl_4$ from aqueous to toluene. 0.2 mL of the toluene solution of $HAuCl_4$ (0.1 M), 0.2 mL of the toluene solution of DT (0.1 M), and 1.2 mL of toluene were added to a Teflon cell (thickness: 0.5 mm, optical path length: 8 mm), in which the concentration of $HAuCl_4$ and DT were 0.0125 M (DT/Au = 1). The solution in the Teflon cell was cooled to 263 K using USP-203-A variable-temperature liquid-nitrogen cryostat (UNISOKU Co., Ltd.). To the

solution, 0.4 mL of the DMF solution of $NaBH_4$ (0.1 M) was added using an electromagnetic valve under stirring by magnetic stirrer attached to the cryostat. The addition of the $NaBH_4$ solution was synchronized with the XAFS measurement.

Au L_3-edge QXAFS experiment was carried out on the BL40XU beamline in SPring-8 of the Japan Synchrotron Radiation Research Institute (JASRI; 8 GeV, 100 mA), where a high-flux X-ray is supplied by using a helical undulator.[33] The spectra were measured in the transmission mode. A small and light Si (111) monochromator was used to achieve millisecond time resolution. XAFS spectra with good quality were selected and accumulated for each 1 s time-interval to form a series of spectra. The spectra of the Au foil (0.1 μm) were measured simultaneously for energy calibration. The data reduction was performed using REX2000 Ver.2.5.9. program (Rigaku).

Results and Discussions

We prepared a toluene solution of $HAuCl_4$ for XAFS measurement by the transfer of $HAuCl_4$ from water using tetraoctylammonium bromide (TOAB).[11] 1.6 mL of the toluene solution of $HAuCl_4$ (0.0125 M) in a Teflon cell was reduced by the addition of 0.4 mL of *N*,*N*′-dimethylformamide (DMF) solution of $NaBH_4$ (0.2 M) in the presence of DT (0.0125 M) at 263 K. The XAFS measurement was performed with a 100 ms time resolution. After 10 spectra were collected, the *in-situ* XAFS measurement was triggered off at the same time as the addition of the DMF solution of $NaBH_4$ to the toluene solution. The spectra were measured for 180 s to obtain 1800 spectra. This series of spectra was divided into sets of 10 spectra, and each set of 10 spectra was combined to obtain a single spectrum to improve the S/N ratio.

Figure 1 shows a series of Au L_3-edge XANES spectra during the formation of AuNPs, together with the toluene solution of $HAuCl_4$ and Au foil as references. The XANES spectrum of $HAuCl_4$ has a sharp and narrow absorption band at the edge, which is called the white line; it corresponds to the electronic transition from the $2p_{3/2}$ core level state to a vacant 5d state. The XANES spectrum of the Au foil exhibits almost no white line because of the

fully filled 5d state of Au^0. The addition of DT to $HAuCl_4$ results in the lowering of the white line on the spectrum, indicating reduction of Au^{3+} ions by DT. The white line disappears after the addition of $NaBH_4$ at 0.5 s, followed by the appearance of a small peak just at the high-energy side of the edge as clearly shown in the XANES spectrum at 4.6 s.

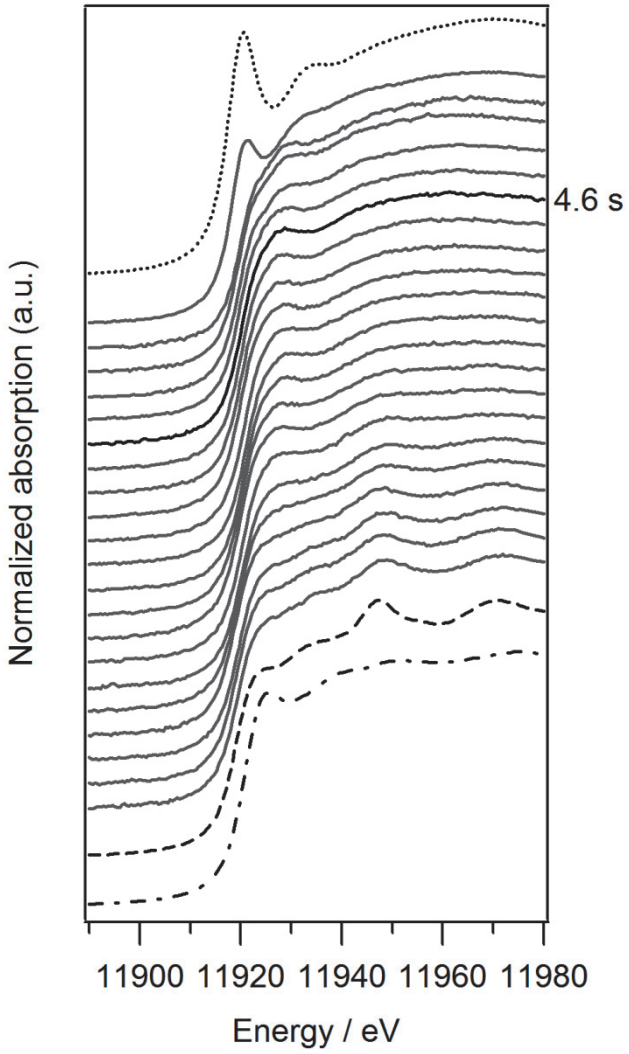

Figure 1. Series of Au L_3-edge XANES spectra during AuNP formation together with those of $HAuCl_4$, Au foil, and $Au_{11}(PPh_3)_8Cl_3$ as references. The XANES spectra during the formation of AuNPs in the presence of the equimolar of DT to $HAuCl_4$ from 0 s to 178.5 s (solid line). The spectra vary from the top to the bottom region with an increase in time. References: $HAuCl_4$ (dotted line), Au foil (dashed line), and $Au_{11}(PPh_3)_8Cl_3$ (dot-dash line).

The intensity of the small peak decreases with time, and the XANES spectra become similar to that of the Au foil. The spectral change indicates the reduction of $HAuCl_4$ and the formation of AuNPs.

First, we investigated the state of Au ions before the reduction. Figure 2 shows the XANES spectra of the $HAuCl_4$ solution in the presence of DT at various concentration ratios of DT to $HAuCl_4$ (DT/Au) before the reduction by $NaBH_4$. The intensity of the white line decreases with an increase in DT/Au from 0 to 2, and further addition of DT does not change the spectral features. The Au atoms in the solution of DT/Au = 16 exist as Au^+ ions, whose 5d states are fully occupied by electrons.[19, 20]

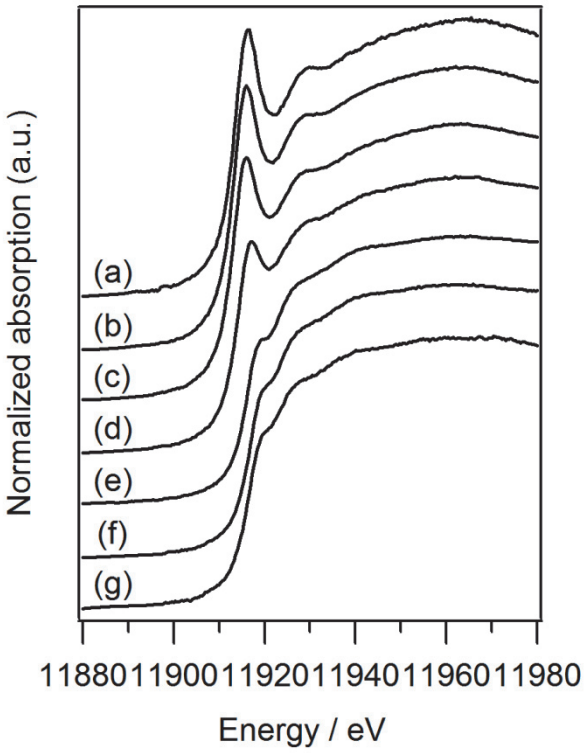

Figure 2. XANES spectra of toluene solution for a series of DT/Au ratios. DT/Au ratios are (a) 0, (b) 0.1, (c) 0.4, (d) 1, (e) 2, (f) 4, and (g) 16.

The XANES spectra change little by the further addition of dodecanethiol, which indicates no formation of Au-S bonds. These results are consistent with the Lennox's work. Accordingly, the equimolar mixture of $[TOA][Au^+X_2]$ and $[TOA][Au^{3+}X_4]$ is a precursor in the toluene solution of DT/Au = 1.

Table 1. The fractions of Au^{3+} and Au^{+} in the solution with various DT/Au ratios before $NaBH_4$ reduction.

DT/Au	0.1	0.4	1	2	4
Au^{3+} (%) [a]	90.3	79.0	50.3	0	0
Au^{+} (%) [a]	9.7	21.0	49.7	100	100
R factor	0.006	0.004	0.005	0.009	0.007
Calcd. Au^{3+} (%) [b]	95	80	50	0	0

[a] The fractions were evaluated by fitting of the XANES spectra of various DT/Au with linear combination of those of DT/Au = 0 and 16.

[b] The fraction was calculated based on the stoichiometric reaction shown below.

The spectra were fitted with the linear combination of those obtained for DT/Au = 0 and 16, i.e., for Au^{3+} and Au^{+} ions, to evaluate the fractions of Au^{3+} and Au^{+} in the solution. The fractions evaluated from the XANES analysis are well consistent with those calculated as per the stoichiometric reaction (Table 1), which indicates the reduction of Au^{3+} ions by two molecules of DT to form Au^{+} ions. Recently, Lennox et al. reported that Au^{3+} ion are reduced by 2 molecules of DT to form $[TOA][Au^{+}X_2]$ (X = Cl^{-} or Br^{-}) complex, and further addition of DT did not lead the formation of Au^{+} thiolate species in two-phase Shiffrin-Brust method.[21] In our study, XANES spectral analysis showed that $[TOA][Au^{3+}X_4]$ is reduced to $[TOA][Au^{+}Cl_2]$ by 2 eq. molar of dodecanethiol.

The UV-vis. spectra of the solutions for various DT/Au ratios were also measured (Figure 3). The intensity and shape of the LMCT band varied as per the conversion of Au^{3+} to Au^{+} when DT/Au was between 0 and 2. The intensity of the LMCT band changed with almost no variation in the peak wavelengths (316 nm and 368 nm) when DT/Au was

between2 and 16. Au^{3+} ions may be reduced to $Au^{\delta+}$ via Au^{+} in the solution of DT/Au = 4 and 16. By observing the XANES spectra carefully, we can see that the shoulder peaks at the edge become slightly smaller with an increase in DT/Au from 2 to 16. The Au^{+} could be further reduced by DT to $Au^{\delta+}$. It is also noted that the precipitation due to the formation of Au^{+} thoilate species was not observed in the presence of more than 2 eq. molar of DT.

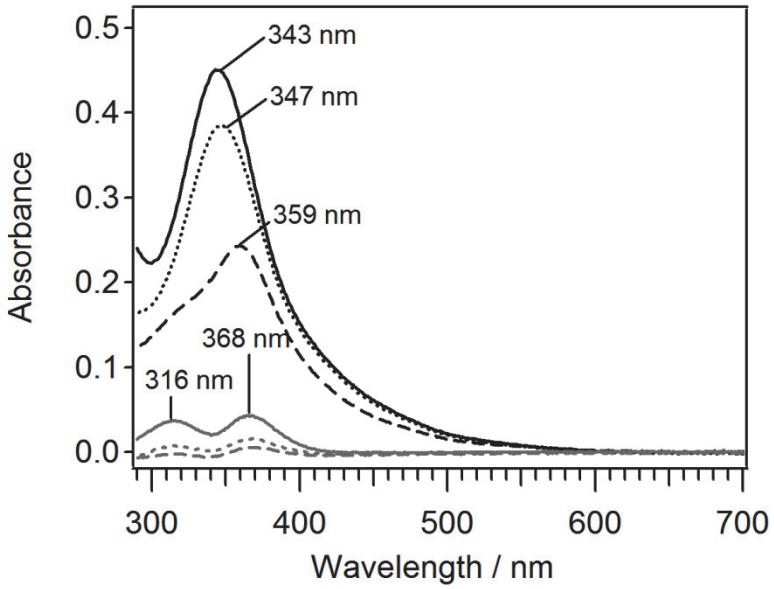

Figure 3. UV-vis spectra of the toluene solutions of $HAuCl_4$ in the presence of various concentrations of DT. DT/Au = 0 (black solid), 0.1 (black dotted), 1 (black dashed), 2 (gray solid), 4 (gray solid), and 16 (gray solid).

The DMF solution of $NaBH_4$ was added to the toluene solution of DT/Au = 1 containing an equal quantity of Au^{3+} and Au^{+} ions. The small peak that appears at the edge after the disappearance of the white line in the early stage of the series of the XANES spectra is shown in Figure 1. The XANES spectrum exhibits the most specific small peak at 4.6 s. A similar small peak is also observed in the XANES spectrum of $Au_{11}(PPh_3)_8Cl_3$,[22] but it is not observed in that of Au^{+} ions. This result suggests that very small AuNPs, i.e., Au nuclei, are formed at 4.6 s. The XANES spectral feature at 4.6 s is broader than that of $Au_{11}(PPh_3)_8Cl_3$,

which is particularly represented as the broader small peak at the edge. This might imply that the Au nuclei might vary in size. It should also be noted that the XANES spectra obtained before the formation of the Au nuclei were fitted by the spectra of the Au nuclei and those of the solution of DT/Au = 16 (Figure 4). Au^{+} ions are the intermediate in the formation process of the Au nuclei. Furthermore, the appearance of the small peak around the edge immediately after the addition of $NaBH_4$ indicates that DT passivates Au just after the reduction of Au ions to Au^{0}, because the small peak is derived from the formation of Au-S bonds[4] and Au ions do not have Au-S bonds.

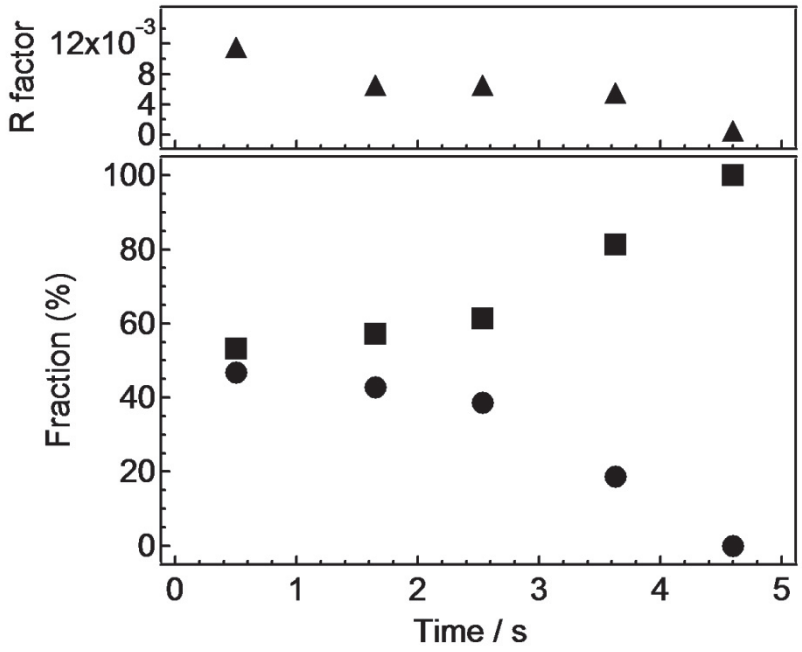

Figure 4. Time course of the fractions of Au^{+} and Au nuclei. Circle: The fraction of the XANES spectrum of the solution of DT/Au = 16 in which Au atoms exist as Au^{+} (or $Au^{\delta+}$). Square: The fraction of Au nuclei observed at 4.6 s. Triangle: The resulting R factor.

The Extended XAFS (EXAFS) spectrum at 4.6 s was analyzed to confirm the formation of the Au nuclei and to investigate their structure. Figure 5 (a) shows the EXAFS spectrum at 4.6 s. The EXAFS spectrum at 4.6 s shows oscillations in the 7.5–11 and 13–15 $Å^{-1}$ *k* ranges (gray regions in Figure 5) and almost no oscillations in the other *k* ranges. The oscillation phase of the Au foil is in accordance with that of the solution of DT/Au = 1 before its reduction in the 7.5–11 and 13–15 $Å^{-1}$ *k* range, although these oscillations are in antiphase in the other *k* ranges. These results suggest that the EXAFS spectrum at 4.6 s consists of the oscillations due to Au-Au scatterings resulting from a face-centered cubic (fcc) crystal structure and those due to Au-X scatterings. A similar EXAFS spectrum as that obtained at 4.6 s is represented by the linear combination of 12.5% of the EXAFS spectrum of the DT/Au = 1 solution (Figure 5 (c)) and 25% of that of Au foil (Figure 5 (d)), as shown in Figure 5 (b). The coordination number of the Au-Au pair of Au nuclei is evaluated to be 3; this is based on the assumption that the coordination number of the Au-Au pair is proportional to the amplitude of the EXAFS spectrum of the Au foil, the coordination number of which is 12. Therefore, the structure of the Au nuclei is estimated to be an Au_4 cluster with an fcc crystal system, as shown in the inset of Figure 5. It should also be noted that almost all the Au atoms in the cell belong to the Au nuclei at 4.6 s, because an XAFS spectrum provides information about the average state of an absorption atom. As far as we know, this is the first report of an observation of Au nuclei in the formation process of AuNPs.

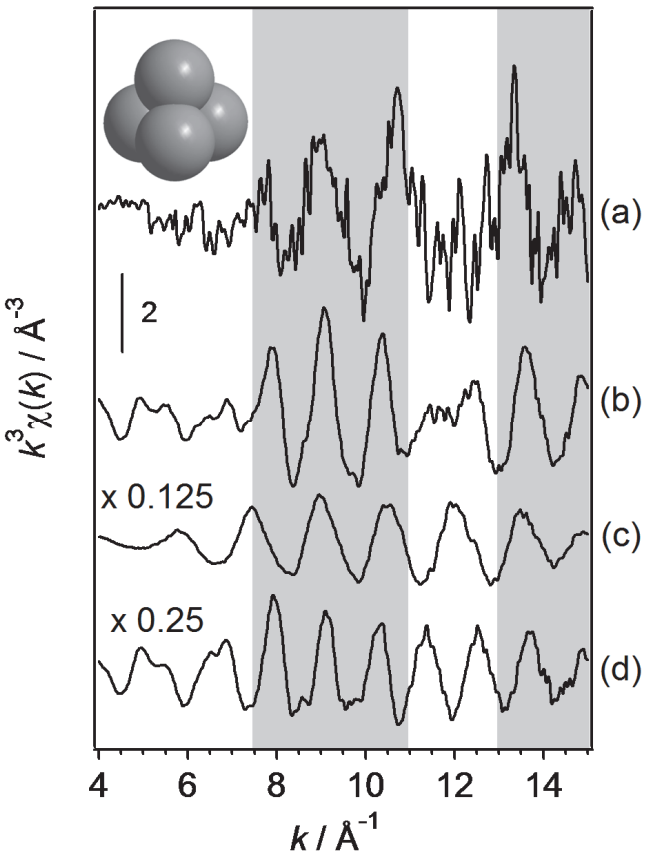

Figure 5. EXAFS spectrum of Au nuclei observed during AuNPs formation. (a) EXAFS spectrum of Au nuclei observed at 4.6 s after the addition of $NaBH_4$ to the $HAuCl_4$ solution. (b) The simulated spectrum by linear combination of the reference spectra of (c) 12.5% of the solution of DT/Au = 1 before reduction and (d) 25% of the Au foil. The 7.5–11 and 13–15 $Å^{-1}$ *k* ranges where the oscillations of (c) and (d) are in phase are in gray. The inset is the estimated structure of Au nuclei from the linear combination, an Au_4 cluster with fcc crystal system.

After the formation of Au nuclei, the XANES spectra approach those of Au foil. Each XANES spectrum after 4.6 s was fitted with the linear combination of the spectrum of the Au nuclei observed at 4.6 s and that of the Au foil (Figure 6). Figure 7 shows the change in the fraction of XANES spectrum at 4.6 s and that of the Au foil. The fraction of the Au nuclei decreases with time and approaches ca. 30%, and that of the Au foil increases and approaches ca. 70% for ca. 180 s. This result indicates that the AuNPs possess less than 100% of the fraction of the Au foil and more than 0% of that of the Au nuclei. In fact, the XANES spectrum of purified AuNPs covered with DT having 3.3±0.5 nm diameter, estimated from TEM observation, was represented by the linear combination of 67.5% of the XANES spectrum of the Au foil and 32.5% of that of the Au nuclei. AuNPs have a larger fraction of surface atoms, i.e., coordinatively unsaturated atoms, than the Au foil, and the Au nuclei almost exclusively consist of coordinatively unsaturated atoms. Therefore, we inferred that the fraction of the XANES spectrum of the Au nuclei was that of the coordinatively unsaturated atoms, and the fraction of the Au foil was that of the coordinatively saturated atoms, i.e., inner atoms of AuNPs. The fractions of the inner and surface atoms of the purified AuNPs estimated by XANES spectral analysis were close to the fractions estimated from the size evaluated from TEM results (the fractions of inner atoms: 49%–62%); the TEM analysis involved the estimation of spherical AuNPs with Au atoms having 2.88 Å atomic diameter. The separation of the XANES spectra of surface and inner atoms between a XANES spectrum of AuNPs conforms to the theoretically calculated result for $Au_{38}(SCH_3)_{24}$ having a truncated-octahedral face-centered-cubic structure by Hakkinen, et al. who showed that the electron-density deficit and buildup regions concentrate around the outermost gold atoms,[23] although the calculated structure is different from the structure of $Au_{38}(SR)_{24}$ determined by single X-ray crystallography reported by Jin et al.[24] We should also mention about the fitting of the XANES spectra. The XANES spectra observed at 178.6 s and the XANES spectra for the purified AuNPs are slightly different from the combined spectra of the Au nuclei and the Au foil, although those observed at the earlier stages after the formation of the Au nuclei fit well (see Figure 6 and 8). The possible reason for the difference is the variation in the 5d state of AuNPs with the size and surrounding environment of AuNPs.[4, 25, 26] The size and

protecting agents of AuNPs can cause variations in the d-d interaction of Au atoms and the d-charge transfer to protecting agents. In fact, the difference can be observed, particularly in the energy region around the edge, where the 5d state of Au atoms mainly contributes to the spectral feature. For a more detailed fitting of XANES spectra of AuNPs, another component of the spectra representing surface Au atoms which have a smaller peak at the edge, is necessary.

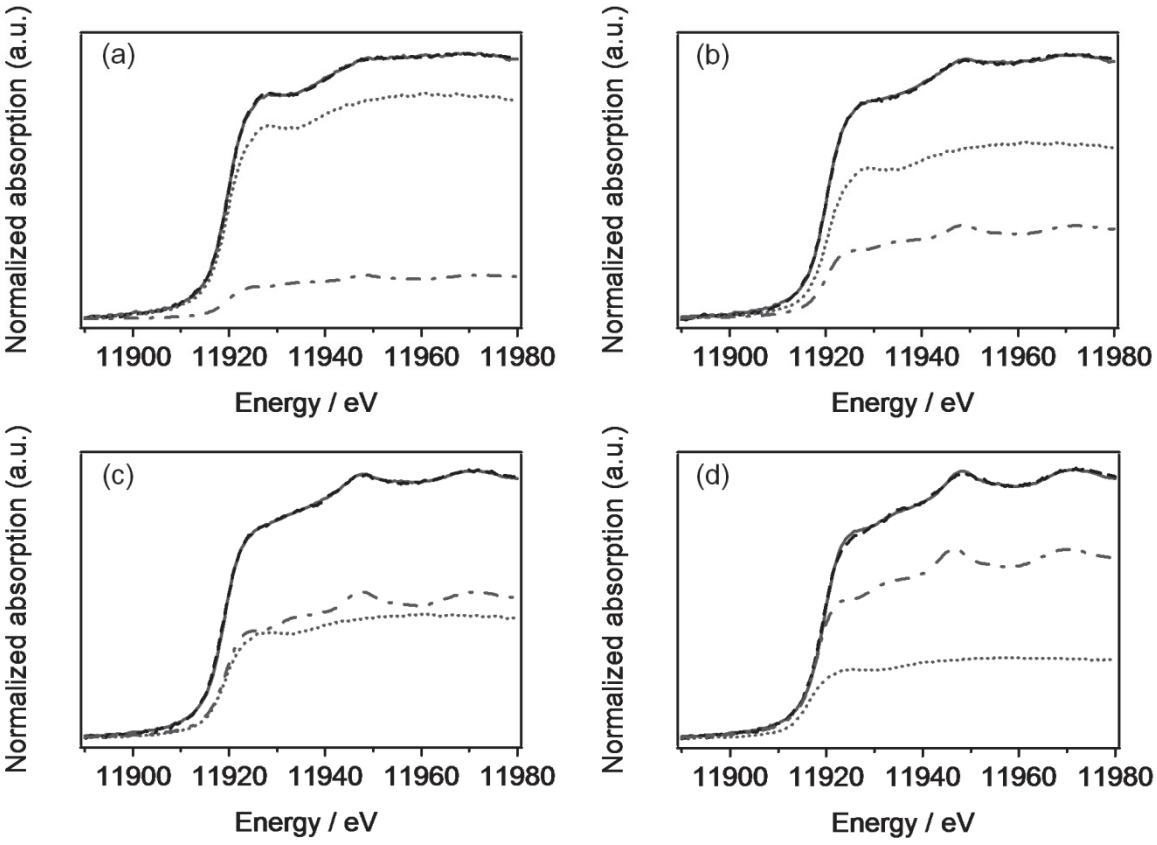

Figure 6. Fitting of the XANES spectra observed at (a) 19.6 s, (b) 39.5, (c) 79.6, and (d) 178.6 s with the linear combination of those of Au nuclei observed at 4.6 s (gray dotted line) and Au foil (gray dot-dash line). Black dashed line: The practical spectra. Gray solid line: The spectra resulted from the linear combination.

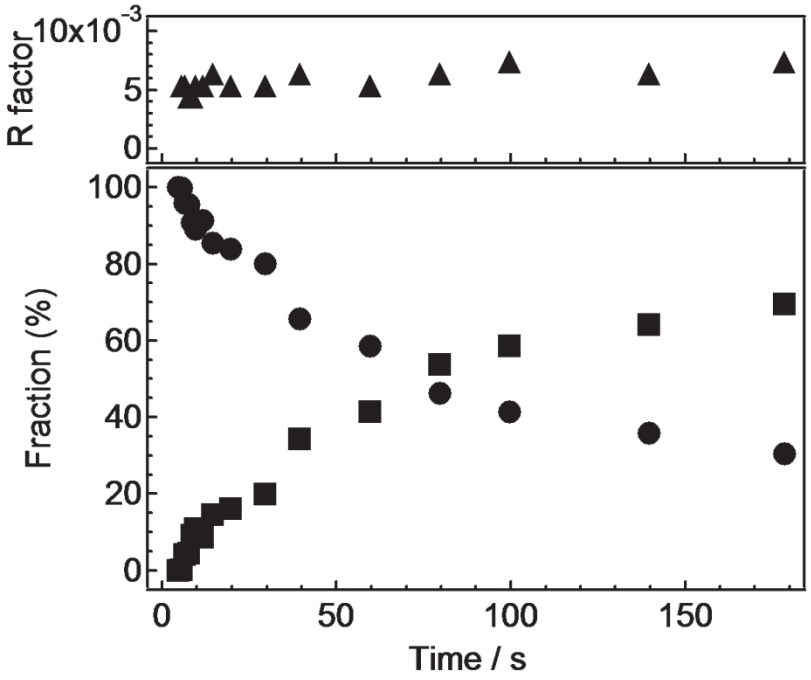

Figure 7. Time course of the fractions of the surface and inner atoms of AuNPs. The fraction of the XANES spectrum of Au nuclei observed at 4.6 s during the formation of AuNPs, representing that of the surface atoms of AuNPs (circle). The fraction of the XANES spectrum of the Au foil representing that of the inne atoms (square). The fractions were evaluated by least-squares fitting of the series of XANES spectra with a linear combination of the spectra of the Au nuclei and Au foil. The resulting R factor (triangle).

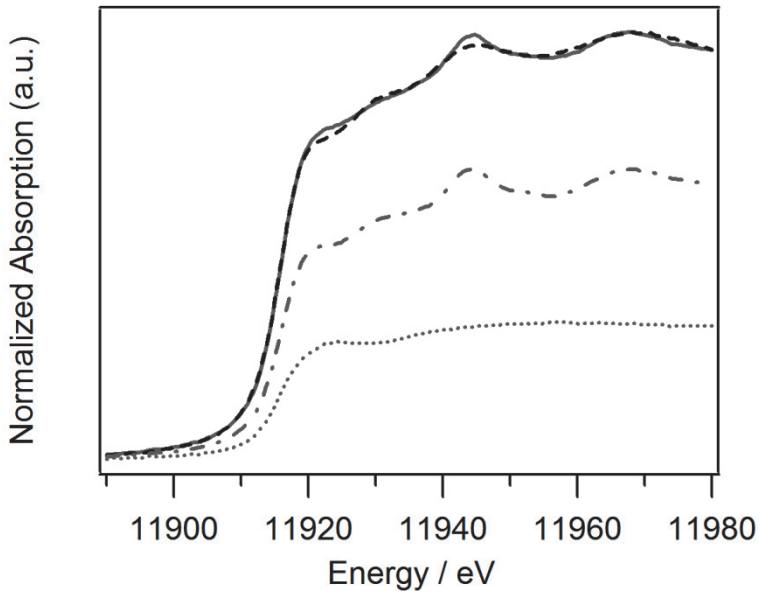

Figure 8. The measured XANES spectrum of purified AuNPs (black dashed line) and the spectra resulting from the linear combination (gray solid line) of the spectra of Au nuclei observed at 4.6 s (gray dotted line) and Au foil (gray dashed line).

In order to confirm our interpretation of the XANES spectra of the Au nuclei and Au foil, we calculated the XANES spectra of the surface and the inner atoms of Au_{144} cluster protected by 60 of sulfur atoms[27] as a model by using the FEFF 8.4 code.[28] Figure 5 shows the XANES spectra of the surface Au atoms and the inner Au atoms of the Au_{144} cluster, together with the XANES spectrum of the whole cluster. The XANES spectra of the following two types of the surface Au atoms were calculated; one type is the outermost atom having two Au-S bonds; the other type is the second-outermost atom having one Au-S bond. As inner atoms, the following two types of Au atoms were chosen; one is the innermost atom having 11 of Au-Au bonds; the other is the second-innermost atom having 12 of Au-Au bonds. The XANES spectra of the inner Au atoms show two obvious peaks in the range from 11940 eV to 11980 eV, which is similar to the spectrum of the Au foil shown in Figure 1. The surface Au atoms exhibit smoother spectra than the inner Au atoms, and have similar characteristics as that of the Au nuclei. The whole cluster represents an intermediate spectrum between the spectrum of the surface atoms and that of the inner atom. These results support

the interpretation that the XANES spectra of the Au foil and the Au nuclei are those of the inner and surface atoms of AuNPs, respectively.

On the basis of this interpretation, the change in the fractions shown in Figure 7 is understood to be on the account of the growth of AuNPs, because the fraction of the surface atoms decreases, and that of the inner atoms increases with time. Now, we speculate whether the growth of AuNPs in this condition proceeds via the aggregation of the Au nuclei themselves, the AuNPs themselves, and/or both the Au nuclei and AuNPs, because, as mentioned above, the XAFS spectrum of the Au nuclei was observed. Several scientists had proposed formation mechanisms for AuNPs; the LaMer mechanism and Finke–Watzky mechanism are the most well known mechanisms.[29-31] In LaMer mechanism, NPs are formed by burst nucleation and slow growth by the addition of monomers without further nucleation.[29] The Finke–Watzky mechanism is a slow and continuous nucleation and an autocatalytic surface growth.[30, 31] Our *in situ* analysis showed the different mechanism from them: reduction of all of Au ions; formation of small clusters, nuclei; aggregation of the nuclei and then the particles to grow larger. Duff et al. analyzed the particle size distribution investigated by TEM to propose the combination/coalescence mechanism as a dominant particle growth mechanism.[32] Their mechanism is compatible to our mechanism proposed by *in situ* analysis. They applied $P(CH_2OH)_4Cl$ to a reductant for preparation of AuNPs. $P(CH_2OH)_4Cl$ is a strong reducing agent to succeed in fast reduction of Au^{3+} to Au^0 as well as $NaBH_4$ used in this study. The fast reduction of Au^{3+} by strong reducing agents will produce Au nuclei, which aggregate to become larger.

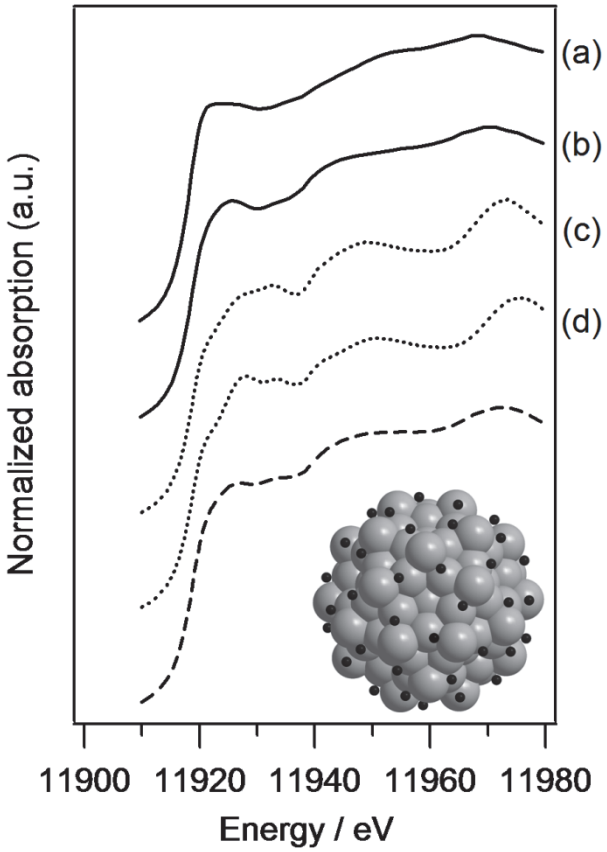

Figure 5. Calculated XANES spectra of the surface (solid line), and inner Au atoms (dotted line) of Au_{144} cluster protected by 60 of S atoms (insert; Au: gray, S: black), together with the entire cluster (dashed line). (a) The outermost atom having two Au-S bonds. (b) The second-outermost atom having one Au-S bond. (c) The second-innermost atom having 12 of Au-Au bonds. (d) The innermost atom having 11 of Au-Au bonds.

Conclusion

The formation process of AuNPs in the presence of the equimolar of DT to $HAuCl_4$ was observed using millisecond time-resolved QXAFS measurement. The XANES spectral change revealed that AuNPs are formed by the reduction of the solution containing an equal quantity of Au^{3+} and Au^{+} ions, via the formation of Au nuclei. The series of XANES spectra obtained after the formation of Au nuclei at 4.6 s were respectively fitted by the linear combination of those of the Au nuclei and Au foil to obtain the fractions of the spectra. The fraction of the XANES spectrum of the Au foil was identified as that of the inner atoms of AuNPs; and the fraction of the XANES spectrum of the Au nuclei, as that of the surface atoms. These analyses clarified the time course of the growth of the AuNPs. The XANES spectral analysis in this study will lead to the kinetic assessment of the formation reaction of AuNPs, which can reveal their formation mechanism via the useful $NaBH_4$ reduction system. The further study for the mechanism under various reaction conditions, for example, reaction temperature, concentration, thiol/Au ratio, and so on, will reveal how the reaction parameters affect the growth kinetics and the size of AuNPs, which will develop the strategy for a synthesis of AuNPs with a specific size.

References

(1) Daniel, M.-C.; Astruc, D. *Chem. Rev.* **2003**, *104*, 293.

(2) Haruta, M. *Catal. Today* **1997**, *36*, 153.

(3) Jain, P. K.; Huang, X.; El-Sayed, I. H.; El-Sayed, M. A. *Acc. Chem. Res.* **2008**, *41*, 1578.

(4) Zhang, P.; Sham, T. K. *Appl. Phys. Lett.* **2002**, *81*, 736.

(5) Hu, M.; Chen, J.; Li, Z.-Y.; Au, L.; Hartland, G. V.; Li, X.; Marquez, M.; Xia, Y. *Chem. Soc. Rev.* **2006**, *35*, 1084.

(6) Enustun, B. V.; Turkevich, J. *J. Am. Chem. Soc.* **1963**, *85*, 3317.

(7) Murphy, C. J.; Sau, T. K.; Gole, A. M.; Orendorff, C. J.; Gao, J.; Gou, L.; Hunyadi, S. E.; Li, T. *J. Phys. Chem. B* **2005**, *109*, 13857.

(8) Kim, F.; Connor, S.; Song, H.; Kuykendall, T.; Yang, P. D. *Angew. Chem. Int. Ed.* **2004**, *43*, 3673.

(9) Eustis, S.; Hsu, H.-Y.; El-Sayed, M. A. *J. Phys. Chem. B* **2005**, *109*, 4811.

(10) Teranishi, T.; Kiyokawa, I.; Miyake, M. *Adv. Mater.* **1998**, *10*, 596.

(11) Brust, M.; Walker, M.; Bethell, D.; Schiffrin, D. J.; Whyman, R. *J. Chem. Soc. Chem. Commun.* **1994**, 801.

(12) Schmid, G. *Chem. Rev.* **1992**, *92*, 1709.

(13) Crooks, R. M.; Zhao, M. Q.; Sun, L.; Chechik, V.; Yeung, L. K. *Acc. Chem. Res.* **2001**, *34*, 181.

(14) Ohyama, J.; Hitomi, Y.; Higuchi, Y.; Shinagawa, M.; Mukai, H.; Kodera, M.; Teramura, K.; Shishido, T.; Tanaka, T. *Chem. Commun.* **2008**, 6300.

(15) Teramura, K.; Okuoka, S.; Yamazoe, S.; Kato, K.; Shishido, T.; Tanaka, T. *J. Phys. Chem. C* **2008**, *112*, 8495.

(16) Shishido, T.; Asakura, H.; Amano, F.; Sone, T.; Yamazoe, S.; Kato, K.; Teramura, K.; Tanaka, T. *Catal. Lett.* **2009**, *131*, 413.

(17) Grunwaldt, J. -D.; Beier, M.; Kimmerle, B.; Baiker, A.; Nachtegaal, M.; Griesebock, B.; Lutzenkirchen-Hecht, D.; Stotzel, J.; Frahm, R.; *Phys. Chem. Chem. Phys.* **2009**, *11*, 8779.

(18) Polte, J.; Ahner, T. T.; Delissen, F.; Sokolov, S.; Emmerling, F.; Thunemann, A. F.; Kraehnert, R. *J. Am. Chem. Soc.* **2010**, *132*, 1296.

(19) Cha, S.-H.; Kim, J.-U.; Kim, K.-H.; Lee, J.-C. *Chem. Mater.* **2007**, *19*, 6297.

(20) Nakamoto, M.; Yamamoto, M.; Fukusumi, M. *Chem. Commun.* **2002**, 1622.

(21) Goulet, P. J. G.; Lennox, R. B. *J. Am. Chem. Soc.* 2010, 132, 9582.

(22) Woehrle, G. H.; Warner, M. G.; Hutchison, J. E. *J. Phys. Chem. B* **2002**, *106*, 9979.

(23) Hakkinen, H.; Barnett, R. N.; Landman, U. *Phys. Rev. Lett.* **1999**, *82*, 3264.

(24) Qian, H.; Eckenhoff, W. T.; Zhu, Y.; Pintauer, T.; Jin, R. *J. Am. Chem. Soc.* **2010**, *132*, 8280.

(25) Benfield, R. E.; Grandjean, D.; Kroll, M.; Pugin, R.; Sawitowski, T.; Schmid, G. *J. Phys. Chem. B* **2001**, *105*, 1961.

(26) Zhang, P.; Sham, T. K. *Phys. Rev. Lett.* **2003**, *90*, 245502.

(27) MacDonald, M. A.; Zhang, P.; Qian, H.; Jin, R. *J. Phys. Chem. Lett.* **2010**, *1*, 1821.

(28) Ankudinov, A. L.; Ravel, B.; Rehr, J. J.; Conradson, S. D. *Physical Review B* **1998**, *58*, 7565.

(29) LaMer, V. K.; Dinegar, R. H. *J. Am. Chem. Soc.* **1950**, *72*, 4847.

(30) Watzky, M. A.; Finke, R. G. *J. Am. Chem. Soc.* **1997**, *119*, 10382.

(31) Watzky, M. A.; Finney, E. E.; Finke, R. G. *J. Am. Chem. Soc.* **2008**, *130*, 11959.

(32) Duff, D. G.; Baiker, A.; Edwards, P. P. *Langmuir* 1993, 9, 2301.

(33) Uruga, T.; Tanida, H.; Inoue, K.; Yamazaki, H.; Irie, T. *AIP Conf. Proc.* **2007**, *882*, 914.

Chapter 4

In Situ Quick XAFS Study on the Formation Mechanism of Small Gold Nanoparticles Supported by Porphyrin-cored Tetradentate Passivants

Abstract

We previously reported that a porphyrin-cored tetradentate passivant, which has two disulfide straps over one face of the porphyrin plane, can produce monolayer-protected gold nanoparticles, 2−4 nm in size, by the one-pot reduction of $HAuCl_4$ in DMF. The resulting nanoparticles are smaller than those prepared using the same S/Au molar ratio of a monodentate passivant. To examine the formation mechanism of small gold nanoparticles, the formation of gold nanoparticles in the presence of porphyrin-cored tetradentate passivants or a structurally related monodentate passivant was studied by time-resolved quick X-ray absorption fine structure spectroscopy. The results demonstrated that all of Au ions in solution are reduced to compose small Au clusters, i.e. nuclei, just after the $NaBH_4$ reduction of $HAuCl_4$ in both cases, but their size varied with the initial S/Au molar ratios and structure of the passivants. Thus, the size of Au nuclei was kinetically controlled by the passivants. Interestingly, the porphyrin-cored tetradentate passivant could stabilize smaller gold nanoparticles, 2−4 nm in size, but it was less efficient in trapping the Au nuclei formed at a very early stage, in comparison to the monodentate passivant.

Introduction

Size control of gold nanoparticles is essential for tuning their unique properties such as catalytic activity, extinction characteristics, and magnetism.[1-3] Wet chemical synthesis of gold nanoparticles is one of the most reliable methods to control their size. Since a report by Brust et al., alkanethiols have been frequently used as the passivants for gold nanoparticles in wet chemistry.[4] The Brust–Schiffrin method allows us to prepare gold nanoparticles, ca. 2–5 nm in size, in a size-controlled manner by varying the initial molar ratio of alkanethiols and gold ions.[5-9] Moreover, recent advances have led to the production of atomically precise gold nanoparticles protected by alkanethiols, such as $Au_{102}RS_{44}$ and $Au_{25}RS_{18}$ clusters.[10,11] Designing passivants is another effective method to control the size of gold nanoparticles. Yonezawa et al. elegantly demonstrated that smaller gold nanoparticles can be obtained using a four-chained disulfide passivant as compared to those prepared using monoalkanthiols.[9] Mayor et al. synthesized a series of linear oligomeric multidentate thioether ligands and demonstrated a considerable increase in the stability and monodispersity of the resultant gold nanoparticles with the increasing length of the oligomeric ligands.[12] We also demonstrated that small porphyrin-coated gold nanoparticles, 2−4 nm in size, can be produced by the one-pot reduction of $HAuCl_4$ in the presence of bulky porphyrin-cored tetradentate passivants, which have four acetyl alkanethiols or two disulfide straps over the porphyrin plane.[7,8] Among the porphyrin-cored tetradentate passivants, α,α,α,α-5,10,15,20-(*o*-bisdisulfidepropylamidophenyl)porphyrin (**1**) (Scheme 1) afforded small gold nanoparticles, 2–4 nm in size, over the range of the initial S/Au ratios from 1 to 16.[7] Thus, multidentate passivants have been proven to be effective for the stabilization and size control of gold nanoparticles. However, the formation mechanism of small gold nanoparticles supported by multidentate passivants has not been explored in detail in terms of time-dependent processes.

Scheme 1 Structures of tetradentate porphyrin passivant having two disulfide straps over the porphyrin plane (a) and monodentate passivant (b).

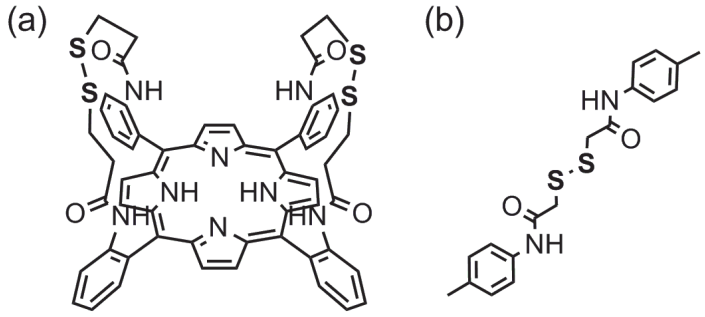

Some mechanisms have been proposed for the formation of gold nanoparticles during wet chemical synthesis. In the LaMer mechanism, gold nanoparticles are generated through a burst nucleation process followed by slow growth of an Au cluster by adding metal precursors.[13,14] On the other hand, an *ex situ* analysis performed by Duff et al. proposed that once all gold ions are reduced to form Au nuclei, the Au nuclei become larger by combination and coalescence.[15] We recently monitored the formation mechanism of gold nanoparticles in the presence of equimolar quantities of 1-dodecanthiol and $HAuCl_4$ by millisecond time-resolved quick X-ray absorption fine structure spectroscopy (QXAFS).[16] The X-ray absorption near edge structure (XANES) spectra showed that half the Au atoms exist as Au^+ ions even before the $NaBH_4$ reduction, which is compatible with the results reported by Goulet and Lennox.[17] Based on the time-resolved XANES spectral changes, we proposed that once all gold ions, Au^{3+} and Au^+, are reduced to compose very small Au clusters, which we call Au nuclei in this paper, and then the Au nuclei aggregate themselves to grow. This is in agreement with Duff's mechanism but not with the LaMer mechanism.

In this study, we investigated the formation mechanism of gold nanoparticles in the presence of the porphyrin-cored tetradentate passivant **1** by transmission electron microscopy (TEM), UV-vis spectroscopy, and *in situ* quick X-ray absorption fine structure spectroscopy (XAFS) to reveal the effect of the bulky porphyrin-cored tetradentate passivant on the formation mechanism of gold nanoparticles.

Experimental

Materials. All chemicals and solvents were purchased from Wako Pure Chemical Industries, Ltd., Japan. Passivant **1** and 4-(*S*-acetyl-thioacetamide)-toluene were prepared according to the reported procedure.[7,8]

Instrumentation. Electronic absorption spectra were measured on a HITACHI U-3500 UV-VIS-NIR spectrometer by using a quartz cell with a 1 cm path length. The TEM images were obtained using JEOL JEM-100SX and JEM-2100F electron microscopes operating at accelerating voltages of 100 and 200 kV, respectively. The TEM samples were prepared by depositing drops of a methanol solution onto a carbon-coated copper grid (Okenshoji Co., Ltd.), which were then dried at room temperature. At least 200 particles were measured to determine the mean diameter.

Acetamide, 2,2'-dithiobis[*N*-(4-methylphenyl)- (2). The monodentate passivant **2** was prepared by the hydrolysis of 4-(*S*-acetyl-thioacetamide)-toluene.[8] To a solution of 4-(*S*-acetyl-thioacetamide)-toluene (0.161 g, 0.0722 mmol) in tetrahydrofuran (THF, 110 mL), 25% aqueous NH_3 (13 mL) was added. After the mixture was stirred for 1 day at room temperature, the solvent was removed under reduced pressure. The residue was dissolved in $CHCl_3$ and washed with water. The aqueous phase was washed with $CHCl_3$, and the organic phase was then collected and dried over Na_2SO_4. After filtration, the solution was concentrated under reduced pressure. The residue was purified by column chromatography on silica gel eluted with 1–2 vol% CH_3OH in $CHCl_3$ and subsequent recrystallization from CH_2Cl_2/MeOH to produce **2**. Yield: 80 mg, 62%. TLC: R_f = 0.60 ($CHCl_3$:MeOH = 10:1); HRMS-FAB (m/z): $[M+H]^+$ calculated for $C_{18}H_{20}O_2N_2S_2$, 360.0966; found, 360.0965; ^{1}H-NMR ($CDCl_3$, 400 MHz): δ = 8.31 (s, 2H), 7.49–7.47 (m, 4H),7.15–7.13 (m, 4H), 3.62 (s, 4H), 2.33 (s, 6H); ^{13}C-NMR ($CDCl_3$, 100 MHz): δ = 166.6, 135.1, 134.6, 129.7, 120.2, 43.9, 21.0.

Gold nanoparticles coated with 1 (GN@1). **GN@1** was prepared at ξ = 1, where ξ

denotes the used S/Au ratio, as follows. A DMF solution (280 mL) containing **1** (15.4 mg, 15.0 μmol) and $HAuCl_4$ (60.0 μmol) was added to a 500 mL round-bottom flask, which was cleaned with piranha solution. To this solution, a 20 mL DMF solution containing $NaBH_4$ (18.25 mg, 772 μmol) was added. After stirring for 2 h, the reaction mixture was evaporated to ca. 3 mL and precipitated by adding 30 mL methanol to remove excess **1** and inorganic salts. The precipitate was dissolved in 2 mL DMF and reprecipitated by adding 30 mL $CHCl_3$. The reprecipitation process was repeated five times.

Gold nanoparticles coated with 2 (GN@2). **GN@2** was prepared under the conditions identical to those of **GN@1** at $\xi = 1$.

Size-controlled synthesis of gold nanoparticles. Gold nanoparticles were synthesized in the presence of **1** or **2** under various S/Au molar ratios ($\xi = 0$, 0.1, 0.2, 1, 4, and 16). All glass vials for the syntheses of gold nanoparticles were cleaned with piranha solution. A typical method is as follows: 8 mL DMF solution containing **1** (1.0 mM), 13 μL DMF solution of $HAuCl_4$ (154 mM), and 1.8 mL DMF were added to a reaction vessel ($\xi = 16$). While the mixture was vigorously stirred, 100 μL DMF solution of $NaBH_4$ (241 mM) was rapidly added and the mixture was then stirred for 1 h. The solutions were evaporated and the residue was dispersed in MeOH.

XAFS measurement 0.2 mL DMF solution of $HAuCl_4$ (0.1 M), 0.2 mL DMF solution of passivants, and 1.2 mL DMF were added to a Teflon cell (optical path length = 8 mm). The solution in the Teflon cell was cooled to 263 K using USP-203-A, a variable-temperature liquid-nitrogen cryostat (UNISOKU Co., Ltd.). To this solution, 0.4 mL DMF solution of $NaBH_4$ (0.1 M) was added using an electromagnetic valve.

QXAFS experiment at Au L_3-edges was performed on the BL40XU beamline in SPring-8 of the Japan Synchrotron Radiation Research Institute (JASRI; 8 GeV, 100 mA), where a high-flux X-ray is supplied using a helical undulator.[18] The spectra were measured in the transmission mode. A small and light Si(111) monochromator was used to achieve

millisecond time resolution. The XAFS measurements were performed with 100 ms time resolution. After 10 spectra were collected, the *in situ* XAFS measurement was triggered off at the same time as the addition of the DMF solution of $NaBH_4$ to the toluene solution. The spectra were measured for 180 s to obtain 1800 spectra. To improve the signal-to-noise ratio, good-quality XAFS spectra were selected and accumulated for each 1 s time interval to obtain a series of spectra. The spectra of the Au foil (0.1 μm) were measured simultaneously for energy calibration. The data reduction was performed using a REX2000 Ver.2.5.9. program (Rigaku). The k^3-weighted extended X-ray absorption fine structure spectroscopy (EXAFS) oscillation in the range 2.92–13.5 $Å^{-1}$ was Fourier-transformed into *r* space.

Results and Discussions

UV-vis spectra and TEM. Figure 1 shows the UV-vis spectra of **1** in DMF solution in the presence and absence of 4 equivalents of $HAuCl_4$ ($\xi = 1$) before $NaBH_4$ reduction. The spectrum of **1** exhibited a characteristic absorption band at around 423 nm, the so-called Soret band, which did not change in the presence of $HAuCl_4$. This result indicates no interaction between **1** and Au^{3+} ions. Figure 2 shows the UV-vis spectra of **2** in DMF solution in the presence and absence of 2 equivalents of $HAuCl_4$ ($\xi = 1$) before $NaBH_4$ reduction. The observed spectrum of **2** in the presence of $HAuCl_4$ was identical to the combined spectrum of **2** and $HAuCl_4$. Thus, these results indicate that neither **1** nor **2** affects Au^{3+} ions before $NaBH_4$ reduction, which is contrary to the case of alkanethiols. Au^{3+} ions are reduced to generate Au^+ ions in the presence of alkanethiol passivants.[16,17,19] Since the disulfides cannot act as reducing agents, our disulfide-based passivants will not strongly interact with and reduce Au^{3+} ions.

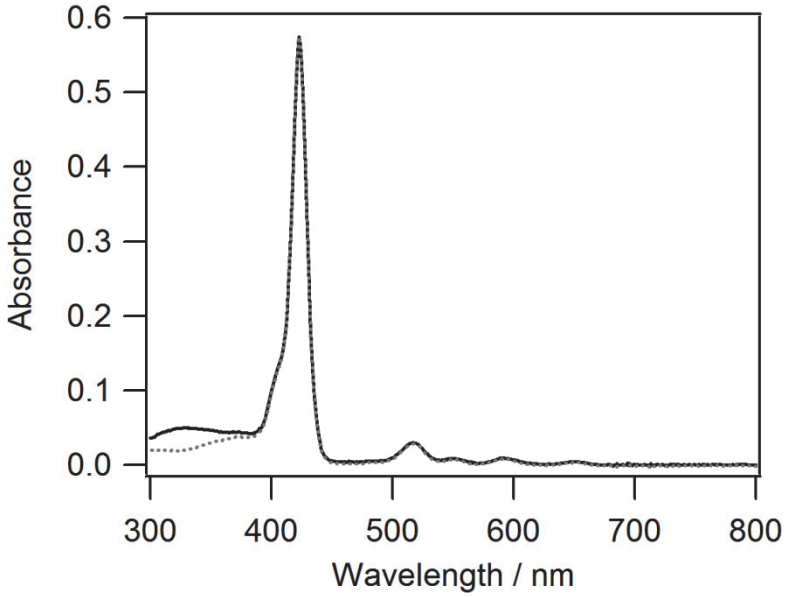

Figure 1. UV-vis spectra of passivant **1** in DMF solution with $HAuCl_4$ at ξ=1 (solid line) and without $HAuCl_4$ (gray dotted line).

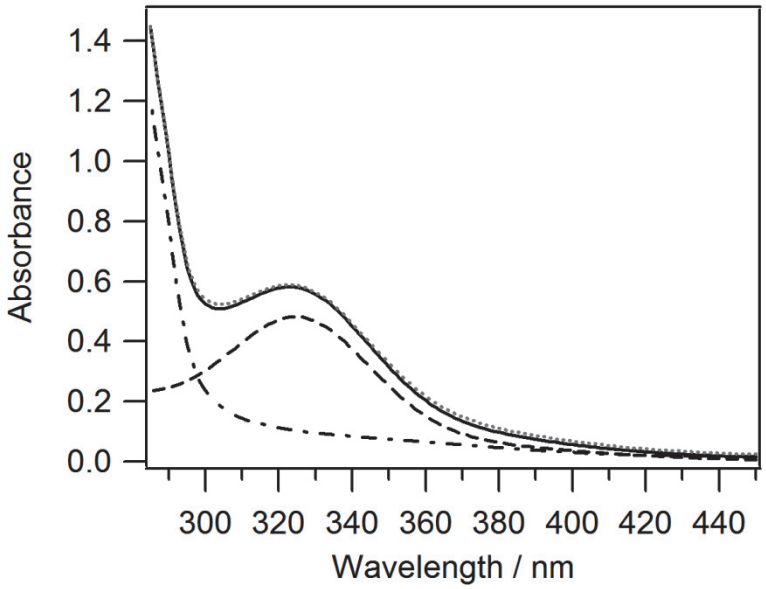

Figure 2. UV-vis. spectra of the DMF solutions containing $HAuCl_4$ and the passivant **2** at ξ=1 (solid line), $HAuCl_4$ (dashed line), **2** (dashed-dotted line), and the combined spectrum of those of $HAuCl_4$ and **2** (gray dotted line).

GN@1 and **GN@2** prepared at ξ = 0.5–16 were characterized by TEM. The TEM images at ξ = 1 are shown in Figure 3, where spherical particles with crystal lattice of gold were observed. Particle analysis of the TEM images demonstrated that the particle sizes of **GN@1** and **GN@2** prepared at ξ = 1 were 2.7 ± 0.3 nm and 3.6 ± 1.0 nm, respectively. The particle size of **GN@2** decreased as the ξ value increased, as reported for **GN@1**, but **GN@2** was always larger than **GN@1** at every examined S/Au ratio, as shown in Figure 4. For example, **GN@1** and **GN@2** prepared at ξ = 0.5 were 3.5 ± 0.4 and 5.0 ± 0.9 nm, respectively. These results demonstrate that the passivant **1** can stabilize gold nanoparticles smaller than those stabilized by **2**.

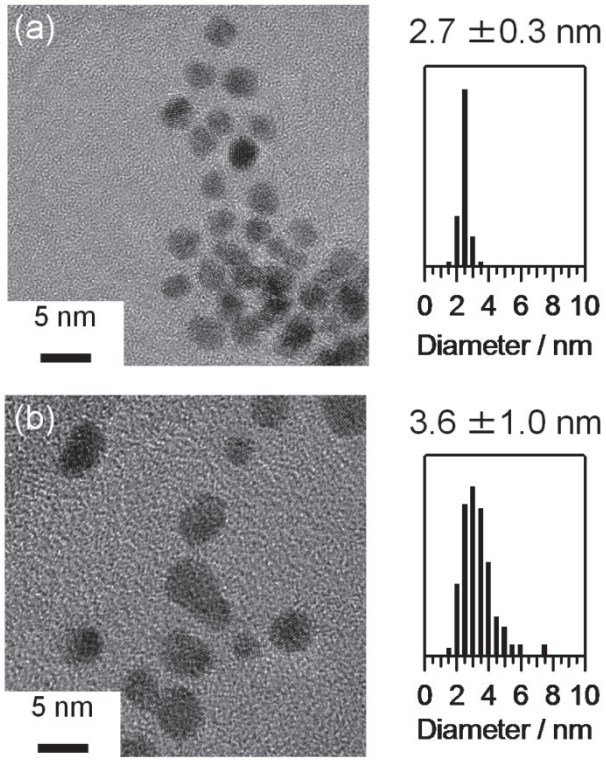

Figure 3. TEM images of **GN@1** (a) and **GN@2** (b) with histograms of particle size on the right. ξ = 1 in both cases.

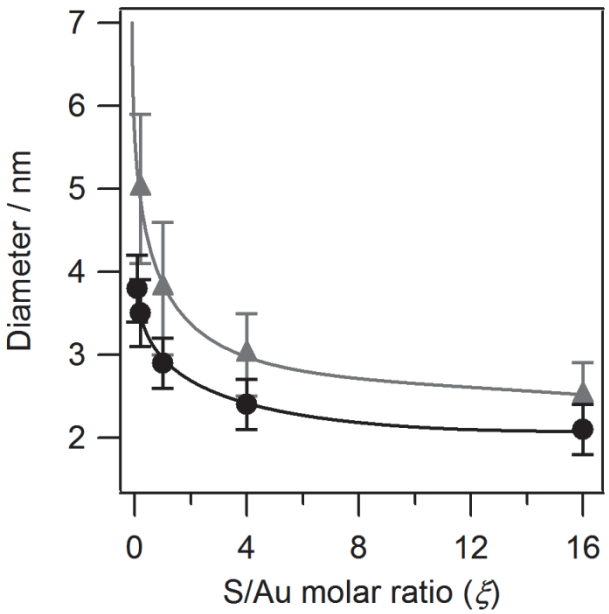

Figure 4. Mean diameter plots of **GN@1** (red) and **GN@2** (black) against the ξ value.

XANES. The Au L_3-edge XANES spectra of the DMF solution containing $HAuCl_4$ in the presence of **1** or **2** at ξ = 1 before the $NaBH_4$ reduction showed a sharp and narrow absorption band at the edge, as shown in Figure 5. This is called the white line and corresponds to the electronic transition from the $2p_{3/2}$ core level state to the vacant $5d_{3/2}$ and $5d_{5/2}$ states. Both the XANES spectra were identical to that of the DMF solution of $HAuCl_4$. This result indicates that **1** and **2** do not reduce Au^{3+} ions, which is consistent with the results of the UV-vis spectral analysis. On the other hand, the addition of $NaBH_4$ will reduce both Au^{3+} ions and disulfides **1** and **2** to the corresponding thiols **1'** and **2'**, as represented in Scheme 2. Note that **2'** has a thiol group within the molecule; therefore, **2** virtually acts as a monodentate passivant. The resulting thiols can interact with Au metal species and Au ions as well as reduce Au^{3+} ions to Au^{+} ions, as mentioned above. In addition, the thiols could bind to Au^{+} ions to form Au^{+}-thiolate species because a polar solvent, DMF, was used in this study.[17]

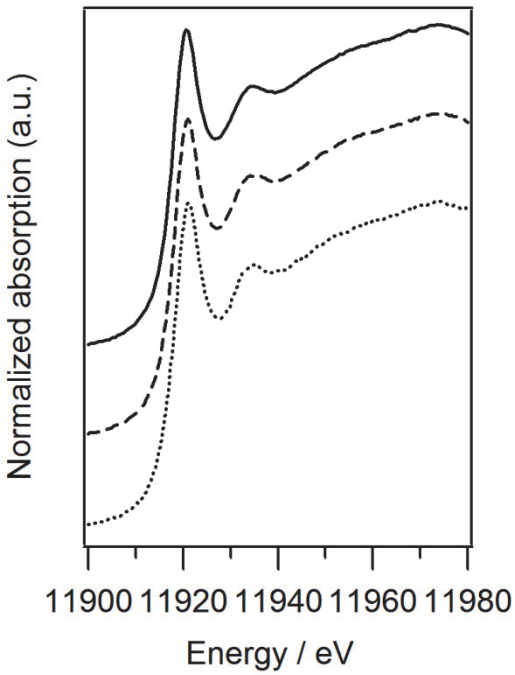

Figure 5. Au L_3-edge XANES spectra of the DMF solutions of $HAuCl_4$ with **1** (solid line) and **2** (dashed line) and a $HAuCl_4$ solution (dotted line).

Scheme 2 Formation of thiols **1'** and **2'** corresponding to disulfides **1** and **2**, respectively, by $NaBH_4$ reduction.

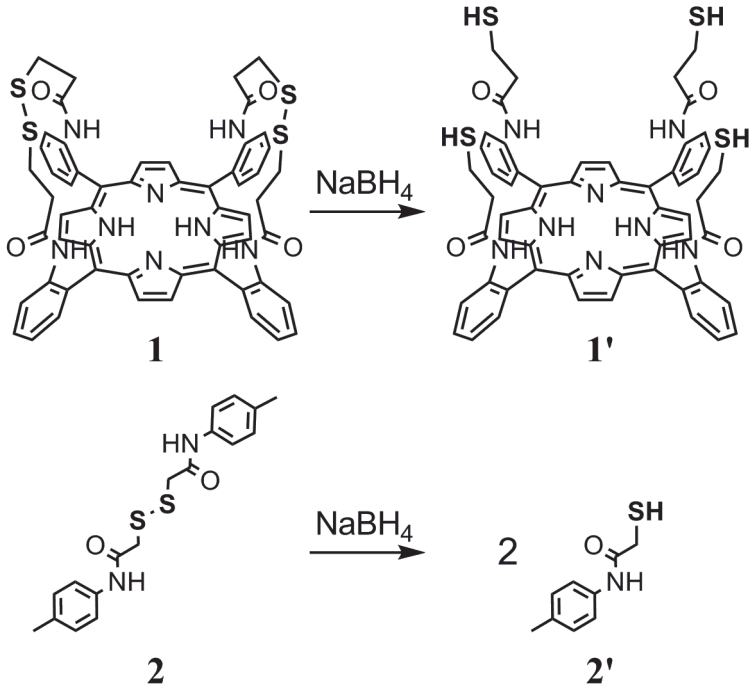

$NaBH_4$ reduction gave rise to changes in both the XANES spectra of the solution containing $HAuCl_4$ in the presence of **1** or **2**. Figure 6 shows the time-resolved Au L_3-edge XANES spectral changes of the solution of **1** and $HAuCl_4$ at $\xi = 1$ on adding $NaBH_4$, together with the spectrum of Au foil as a reference. The white line decreased in intensity and completely disappeared at 5.6 s, which corresponds to the reduction of Au ion, and concomitantly a new, small, and broad peak absorption appeared at 11922 eV. The smooth XANES spectrum observed at 5.6 s indicates the generation of a very small Au cluster, i.e., Au nuclei.[16] After 5.6 s, the smooth XANES spectrum was converted to the spectrum showing two peaks in the energy range 11940–11980 eV. These two peaks were also observed in the XANES spectrum of the Au foil and can be assigned as Au–Au scatterings. Therefore, the increase in the intensity of the two peaks after 5.6 s indicates the growth of gold nanoparticles. From these results, it is concluded that the change in the spectral feature from 5.6 s corresponds to the particle growth by aggregation of Au nuclei. This is because almost all Au atoms in the reaction solution were transformed to the Au nuclei at 5.6 s.[16]

The Au L_3-edge XANES spectra of bare Au clusters, Au_{25} and Au_{38}, and Au–S clusters, $Au_{25}S_{18}$ and $Au_{38}S_{24}$, were simulated using FEFF 8.4 code (Figure 7),[20] whose structures were based on previous reports.[21,22] The small bands around the edge for $Au_{25}S_{18}$ and $Au_{38}S_{24}$ had higher intensity than those around the edge for Au_{25} and Au_{38}. In fact, it was reported that gold nanoparticles supported by alkanethiols showed a more intense band around the edge relative to sulfur-free gold nanoparticles, which were generated within an amine-based dendrimer.[23] Thus, it was concluded that the small band around 11922 eV is due to the formation of Au−S bonds. Therefore, the formation of the small peak around 11922 eV at 5.6 s (Figure 6) indicates that the passivants interacted with Au nuclei at this stage. Furthermore, the simulated small band around the edge for $Au_{38}S_{24}$ was weaker in intensity relative to that for $Au_{25}S_{18}$. Thus, the small band intensity at around 11922 eV should be considered an index of the size of Au nuclei. Similar trends were observed for maturing gold nanoparticles; the peak intensity at 11922 eV decreases as gold nanoparticles become larger as shown in Figure 6.[24,25]

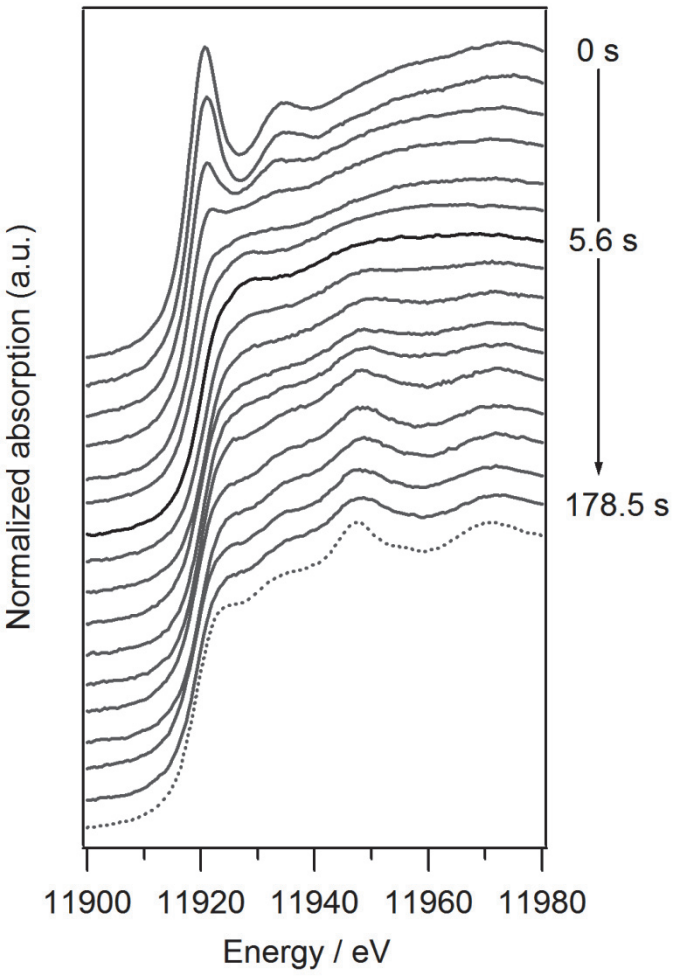

Figure 6. Series of XANES spectra during $HAuCl_4$ reduction in the presence of **1** (solid line), together with the spectrum of Au foil (dotted line). The black solid line represents Au nuclei at 5.6 s.

The $HAuCl_4$ solution containing **2** at $\xi = 1$ showed XANES spectral changes similar to those observed for **1** upon $NaBH_4$ reduction, but the XANES spectrum of Au nuclei showed features different from that of **1**. That is, the peak intensity of Au nuclei at 11922 eV was slightly more intense compared with that observed for **1**, as shown in Figure 8(a) and (b). The larger gold nanoparticles show the weaker absorption band around 11922 eV as described above. Therefore, the weaker absroption band around 11922 eV for **1** than **2** indicates that larger Au nuclei were formed by using **1** than **2**. The formation of larger Au

nuclei with **1** may originate from the low mobility and/or the steric hindrance of **1** because of the large molecular weight and rigidly directed thiol groups of **1**, both of which result in less frequent collisions between the Au species and **1**.

The XANES analysis was performed at various ξ values. As shown in Figure 8, the band at 11922 eV for the Au nuclei prepared with **1** at $\xi = 4$ was higher than that observed at $\xi = 1$. Similarly, the Au nuclei prepared with **2** at $\xi = 0.1$ showed a weaker band at 11922 eV than that observed at $\xi = 1$. Thus, the size of Au nuclei depends on the concentration and structure of the passivants, which implies that the size of Au nuclei is kinetically controlled by the speed with which the passivants trap the growing Au nuclei.

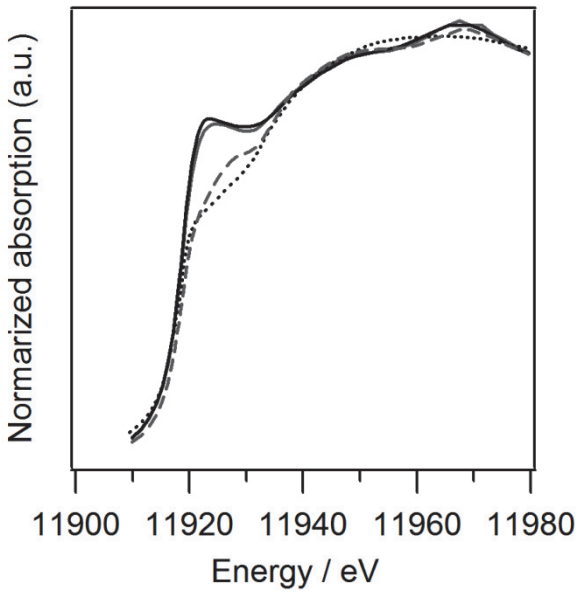

Figure 7. Calculated Au L_3-edge XANES spectra of Au clusters: $Au_{25}S_{18}$ (black solid line), $Au_{38}S_{20}$ cluster (gray solid line),Au_{25} without S atoms (black dotted line), and Au_{38} without S atoms (gray dotted line).

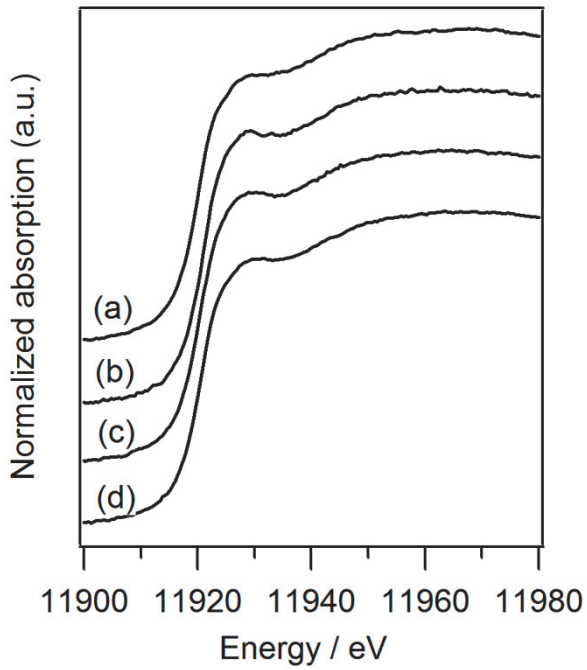

Figure 8. XANES spectra of Au nuclei in the presence of **1** at $\xi = 1$ (a), **2** at $\xi = 1$ (b), **1** at $\xi = 4$ (c), and **2** at $\xi = 0.1$ (d).

EXAFS. Figure 9 shows a series of k^3-weighted EXAFS spectra during the formation of **GN@1**. Before $NaBH_4$ reduction, the EXAFS spectrum showed oscillation phase and amplitude identical to those observed for $HAuCl_4$ alone. Upon $NaBH_4$ reduction, the EXAFS amplitude decreased and the spectrum at 5.6 s showed only small peaks at around 5.2 and 6.9 $Å^{-1}$ (Figure 9(a)), which is characteristic of an Au foil but is not observed for $HAuCl_4$. These spectral changes indicate that the Au−Cl bonds of $AuCl_4^-$ are dissociated and a small number of new Au−Au bonds are generated. The small number of Au−Au bonds suggests the formation of very small Au clusters. As mentioned above, the XANES analysis revealed that the Au–S bond formation took place within the initial 5.6 s. Therefore, it is most likely that the Au–Au bond formation competes with the Au–S bond formation. In other words, Au clusters will be trapped by the passivants during their growing process. This mechanism accounts for the observed size dependence of the Au nuclei on the concentration and structure of the passivants.

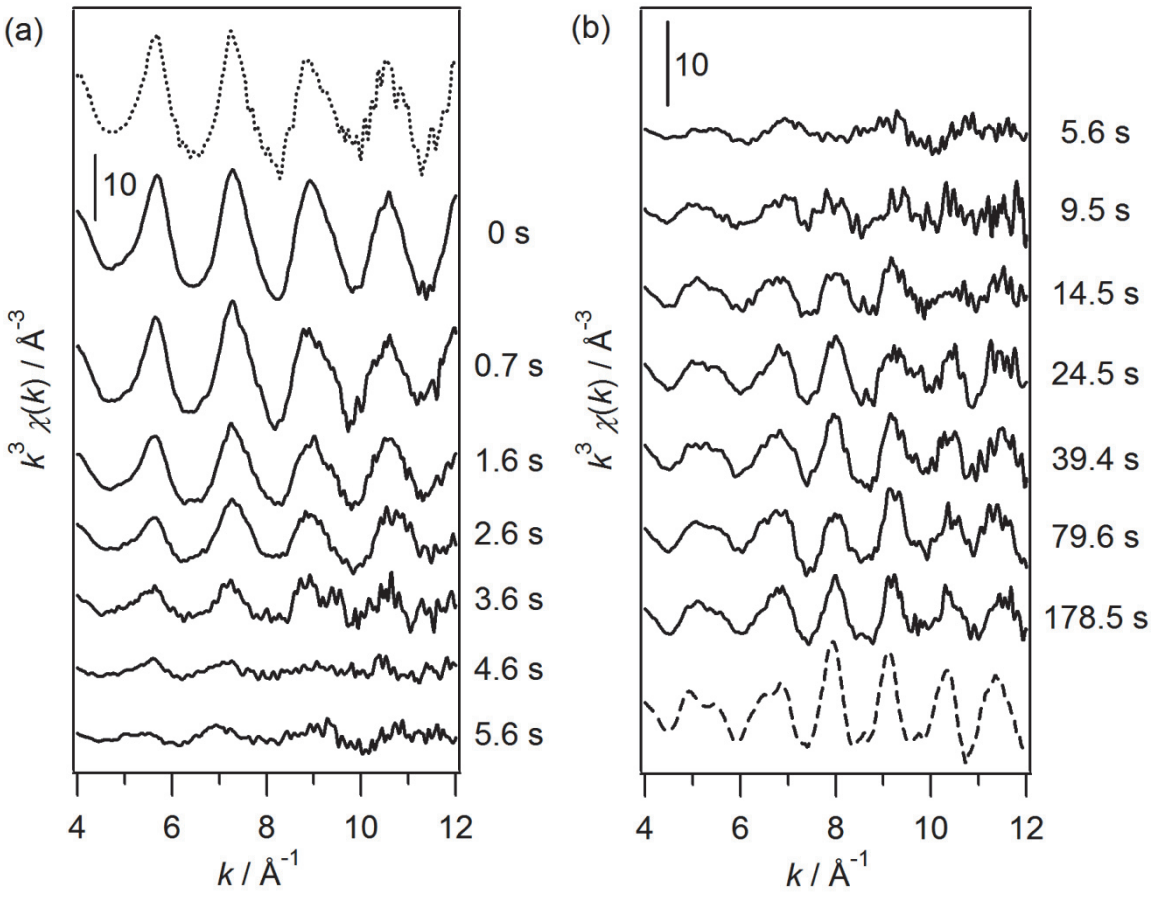

Figure 9. Series of k^3-weighted EXAFS spectra during the **GN@1** formation: spectra from 0 to 5.6 s (solid line) with $HAuCl_4$ (dotted line) (a); spectra from 5.6 to 178.5 s (solid line) with Au foil (dashed line) (b).

Figure 10 shows the k^3-weighted EXAFS spectra of Au nuclei generated using **1** or **2**. The peak intensity of the Au nuclei with **1** around 6.9 Å^{-1} (marked by an arrow in Figure 10) is slightly higher than that with **2**. Thus, both EXAFS and XANES studies suggest that the size of the Au nuclei with **1** is larger than those with **2**.

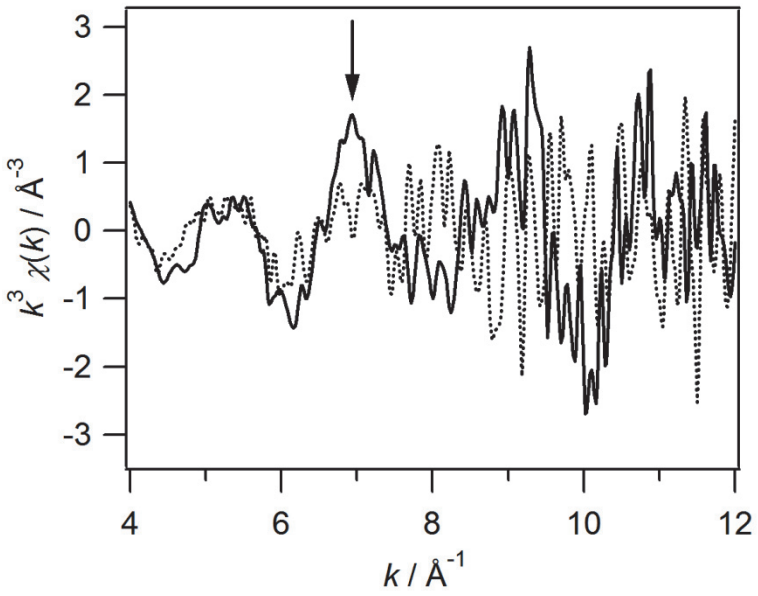

Figure 10. EXAFS spectra of Au nuclei generated with **1** and **2**.

Figure 9(b) shows the time-resolved spectral change after 5.6 s. The amplitude of oscillation increased with the reaction time and the spectral feature of **GN@1** became close to that of the Au foil. The Fourier-transformed EXAFS spectra (FT-EXAFS) after 5.6 s are shown in Figure 11. The height of bands from 1.8 to 3.2 Å, assigned to the Au–Au scatterings of Au metal, increased with the reaction time, indicating the growth of gold nanoparticles. For the formation of **GN@2**, similar changes were observed. The height at 2.68 Å in the FT-EXAFS spectra is plotted against the reaction time in Figure 12. (Unfortunately, the low amplitude and low S/N ratio of the EXAFS data did not allow determination of appropriate structural parameters by curve fitting.) The height for **GN@1** increased up to ca. 5 Å with increased reaction time while that for **GN@2** increased up to ca. 6 Å. Moreover, the height for **GN@1** increased more slowly than that for **GN@2**. These results suggest that **1** suppresses the particle growth more efficiently than **2** to provide smaller gold nanoparticles relative to **1**. This difference is probably caused by the slow dissociation of **1** from the gold surface owing to its tight fixation through four Au–S bonds.

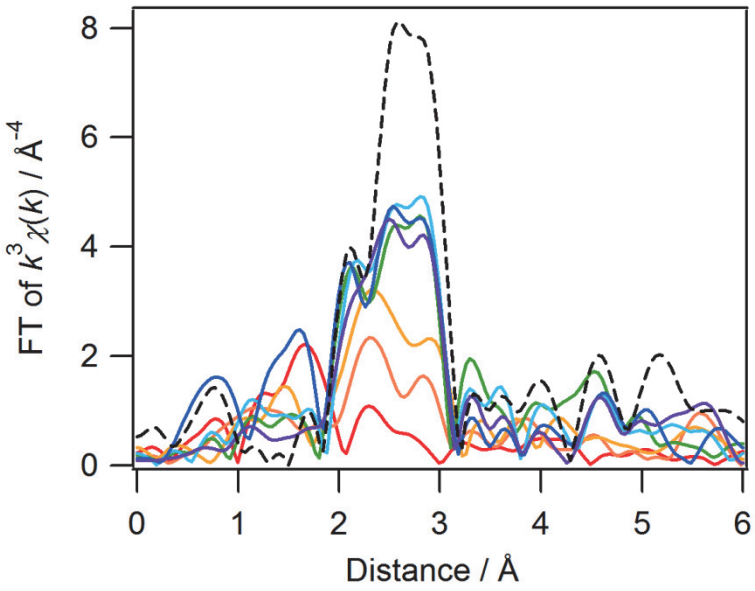

Figure 11. Series of FT- of k^3 weighted EXAFS spectra during the **GN@1** formation together with the Au foil spectrum (dashed line). (red: 5.6 s, orange: 9.5 s, yellow: 14.5 s, green: 24.5 s, light blue: 39.4 s, blue: 79.6 s, purple: 178.5 s).

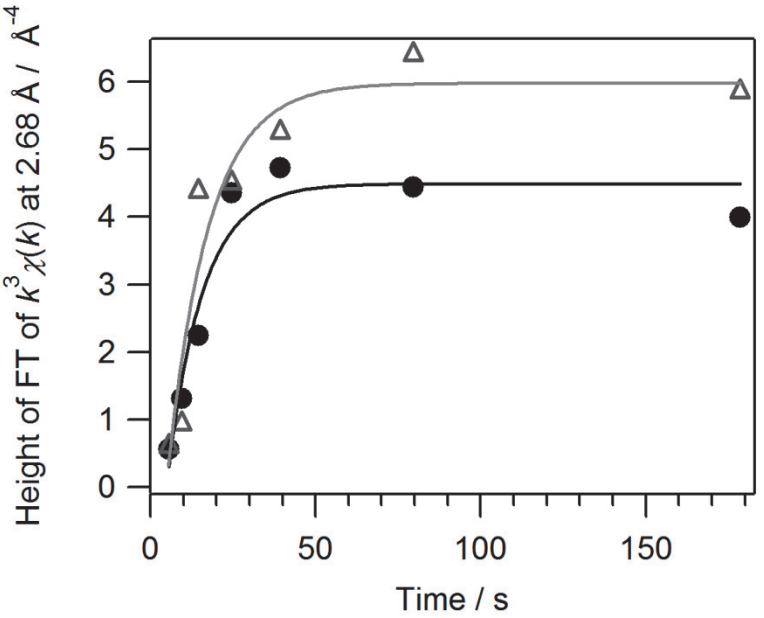

Figure 12. Height of FT of EXAFS spectra at 2.68 Å for **GN@1** (circle) and **GN@2** (triangle) against reaction time after the formation of Au nuclei.

Conclusion

The QXAFS study revealed that all Au ions are reduced to form Au nuclei, and that the Au nuclei become larger by aggregation. This formation mechanism is consistent with that for the gold nanoparticles generated by the $NaBH_4$ reduction of Au^{3+} ions in the presence of 1-dodecanethiol in toluene,[16] except for the lack of reduction of Au^{3+} ions by disulfide passivants. Duff et al. proposed the combination/coalescence mechanism as a particle growth mechanism for the formation of gold nanoparticles by using a strong reducing agent, $P(CH_2OH)_4Cl$, in aqueous solution.[15] Presumably, when strong reducing agents are used, gold nanoparticles grow by aggregation after all of the Au atoms are composed of Au nuclei.

Scheme 3 shows the proposed formation mechanism of gold nanoparticles in the presence of passivants **1** and **2**. Before the $NaBH_4$ reduction, passivants **1** and **2** neither interact with nor reduce Au^{3+} ions. $NaBH_4$ addition reduces $HAuCl_4$ and the disulfide groups of **1** or **2**. The $HAuCl_4$ reduction leads to the dissociation of Au–Cl bonds to form bare Au atoms and then small Au clusters. The reduced form of **1** or **2** traps the very small, growing Au nuclei. Thus, the size of the Au nuclei is kinetically controlled; **1** provides larger Au nuclei than **2** because of the low mobility of **1** and the rigidly directed S atoms of **1**. However, these characteristics of **1** strongly suppress the growth of gold nanoparticles once **1** traps Au nuclei. Thus, this study demonstrates the importance of the initial S/Au ratio and the structure of the passivants, which should provide a useful guideline for the future passivant-based design of gold nanoparticles.

Scheme 3 Formation mechanism of gold nanoparticles in the presence of tetradentate passivant **1** and monodentate passivant **2**.

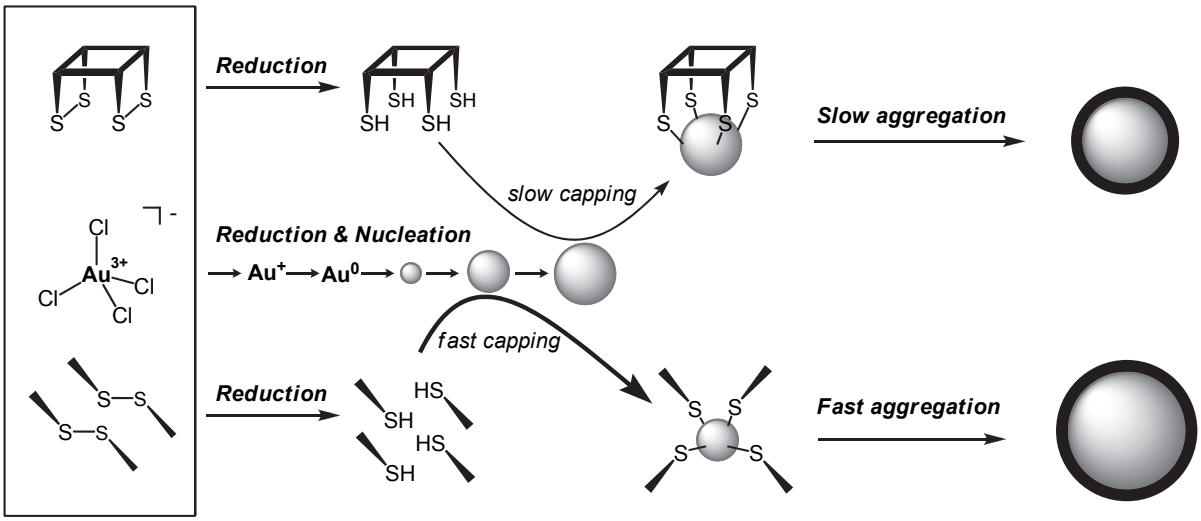

References

(1) Haruta, M. *Catal. Today* **1997**, *36*, 153.

(2) Hu, M.; Chen, J.; Li, Z.-Y.; Au, L.; Hartland, G. V.; Li, X.; Marquez, M.; Xia, Y. *Chem. Soc. Rev.* **2006**, *35*, 1084.

(3) Hori, H.; Yamamoto, Y.; Iwamoto, T.; Miura, T.; Teranishi, T.; Miyake, M. *Phys. Rev. B* **2004**, *69*, 174411.

(4) Brust, M.; Walker, M.; Bethell, D.; Schiffrin, D. J.; Whyman, R. *Chem. Commun.* **1994**, 801.

(5) Hostetler, M. J.; Wingate, J. E.; Zhong, C.-J.; Harris, J. E.; Vachet, R. W.; Clark, M. R.; Londono, J. D.; Green, S. J.; Stokes, J. J.; Wignall, G. D.; Glish, G. L.; Porter, M. D.; Evans, N. D.; Murray, R. W. *Langmuir* **1998**, *14*, 17.

(6) Leff, D. V.; Ohara, P. C.; Heath, J. R.; Gelbart, W. M. *J. Phys. Chem.* **1995**, *99*, 7036.

(7) Hitomi, Y.; Ohyama, J.; Higuchi, Y.; Aoki, K.; Shishido, T.; Funabiki, T.; Kodera, M.; Tanaka, T. *Bull. Chem. Soc. Jpn.* **2010**, *83*, 1392.

(8) Ohyama, J.; Hitomi, Y.; Higuchi, Y.; Shinagawa, M.; Mukai, H.; Kodera, M.; Teramura, K.; Shishido, T.; Tanaka, T. *Chem. Commun.* **2008**, 6300.

(9) Yonezawa, T.; Yasui, K.; Kimizuka, N. *Langmuir* **2001**, *17*, 271.

(10) Jin, R.; Qian, H.; Wu, Z.; Zhu, Y.; Zhu, M.; Mohanty, A.; Garg, N. *J. Phys. Chem. Lett.* **2010**, *1*, 2903.

(11) Jin, R. C. *Nanoscale* **2010**, *2*, 343.

(12) Peterle, T.; Leifert, A.; Timper, J.; Sologubenko, A.; Simon, U.; Mayor, M. *Chem. Commun.* **2008**, 3438.

(13) LaMer, V. K.; Dinegar, R. H. *J. Am. Chem. Soc.* **1950**, *72*, 4847.

(14) Teranishi, T.; Kiyokawa, I.; Miyake, M. *Adv. Mater.* **1998**, *10*, 596.

(15) Duff, D. G.; Baiker, A.; Edwards, P. P. *Langmuir* **1993**, *9*, 2301.

(16) Ohyama, J.; Teramura, K.; Higuchi, Y.; Shishido, T.; Hitomi, Y.; Kato, K.; Tanida, H.; Uruga, T.; Tanaka, T. *ChemPhysChem* **2011**, *12*, 127.

(17) Goulet, P. J. G.; Lennox, R. B. *J. Am. Chem. Soc.* **2010**, *132*, 9582.

(18) Uruga, T.; Tanida, H.; Inoue, K.; Yamazaki, H.; Irie, T. *AIP Conf. Proc.* **2007**, *882*, 914.

(19) Cha, S.-H.; Kim, J.-U.; Kim, K.-H.; Lee, J.-C. *Chem. Mater.* **2007**, *19*, 6297.

(20) Ankudinov, A. L.; Ravel, B.; Rehr, J. J.; Conradson, S. D. *Phys. Rev. B* **1998**, *58*, 7565.

(21) Zhu, M.; Aikens, C. M.; Hollander, F. J.; Schatz, G. C.; Jin, R. *J. Am. Chem. Soc.* **2008**, *130*, 5883.

(22) Qian, H.; Eckenhoff, W. T.; Zhu, Y.; Pintauer, T.; Jin, R. *J. Am. Chem. Soc.* **2010**, *132*, 8280.

(23) Zhang, P.; Sham, T. K. *Appl. Phys. Lett.* **2002**, *81*, 736.

(24) Zhang, P.; Sham, T. K. *Phys. Rev. Lett.* **2003**, *90*, 245502.

(25) MacDonald, M. A.; Zhang, P.; Qian, H.; Jin, R. *J. Phys. Chem. Lett.* **2010**, *1*, 1821.

Chapter 5

In Situ Au L_3 and L_2 edge XANES Spectral Analysis during Growth of Thiol Protected Gold Nanoparticles for the Study on Particle Size dependent Electronic Properties

Abstract

The formation process of gold nanoparticles in the presence of dodecanethiol is observed *in situ* by means of the quick X-ray absorption fine structure (QXAFS) spectroscopy with 100-ms time resolution at Au L_3 and L_2 edges. The series of X-ray absorption near edge structure (XANES) spectra at the both edges were analyzed to evaluate the dispersion and the electronic properties of gold nanoparticles during their growth process.

Introduction

There has been a growing interest in the study of gold nanoparticles (AuNPs) because of their unique properties not observed in the bulk.[1-3] In particular, AuNPs having < 2-nm diameter show the deviated property from not only the bulk but also larger NPs.[2,4] Therefore, great efforts have been made to control the size and structure of AuNPs by using various protective agents or under various conditions.[4-8] Thiol is well known as one of the most useful protective agents to control the size and structure of AuNPs, since the report by Brust et al.[5] The size controlled synthesis can be easily attained by the variation of the initial molar ratio of thiol to Au ion.[6,9,10] Recently, the atomically precise thiolate protecting gold nanoparticles with < 2-nm diameter, $Au_m(SR)_n$, have been synthesized to show new properties such as catalytic activity, chemical stability, magnetic property, optic property, and so on.[1] In order to elucidate the unique properties, it is important to investigate their structure and electronic state.

X-ray absorption spectroscopy (XAS) is often utilized in the characterization of metal NPs.[11,12] Zanchet et al. clarified that the strong Au-S interaction compensates the expected lattice contraction for free AuNPs.[13] Sham el al. reported that AuNPs lose *d* electrons when protected by thiolate which strongly interact with gold, although AuNPs gain electrons in 5*d* orbital when AuNPs are protected by weakly interacting dendrimer.[14] They also revealed that *d* electrons of the thiolate protecting AuNPs decrease with a decrease in their size.[15] MacDonald et al. precisely determined the structure of $Au_{144}(SR)_{60}$, and also investigated the size dependent nature of bonding by comparing $Au_m(SR)_n$.[16] In these studies on the electronic properties of AuNPs passivated by thiol, the Mansour's method has been applied. However, the method assumes that the there is no significant hybridization of orbitals. Thus, we should investigate more closely the XANES analysis of the AuNPs with thiol using Mansour's method.

Very recently, we reported the *in situ* observation of formation process AuNPs using dodecanethiol (DT) as a protecting agent in solution by means of QXAFS spectroscopy having 100-ms time resolution.[17] It is proposed that all of Au ions in solution are reduced by $NaBH_4$ at a burst to form very small Au clusters, nuclei, followed by aggregation of

themselves to form AuNPs.[17,18] In other words, we can observe AuNPs with various sizes, from sub-nanometer to several nanometers, in their growth process. As a result, in this study, the variation of electronic properties with the size of AuNPs is investigated by *in situ* observation of particle formation process.

Experimental section

Preparation and XAFS measurement. 2 mL of $HAuCl_4$ aqueous solution (0.129 M) and 2.58 mL of toluene were added to a round-bottomed flask, followed by the addition of tetraoctylammonium bromide (TOAB) (282 mg, 0.516 mmol), resulting in the transfer of $HAuCl_4$ from aqueous to toluene in the form of $[TOA]AuCl_4$. 0.2 mL of the toluene solution of $HAuCl_4$ (0.1 M), 0.2 mL of the toluene solution of DT (0.1 M), and 1.2 mL of toluene were added to a Teflon cell (optical path length: 8 mm), in which the concentration of $HAuCl_4$ and DT were 0.0125 M (DT/Au = 1). The solution in the Teflon cell was cooled to 263 K using USP-203-A variable-temperature liquid-nitrogen cryostat (UNISOKU Co., Ltd.). To the solution, 0.4 mL of the *N*,*N*′-dimethylformamide (DMF) solution of $NaBH_4$ (0.1 M) was added using an electromagnetic valve.

QXAFS experiment at Au L_3 and L_2 edges was carried out on the BL40XU beamline in SPring-8 of the Japan Synchrotron Radiation Research Institute (JASRI; 8 GeV, 100 mA), where a high-flux X-ray is supplied by using a helical undulator.[19] The spectra were measured in the transmission mode. A small and light Si (111) monochromator was used to achieve millisecond time resolution. The XAFS measurement was performed with 100 ms time resolution. After 10 spectra were collected, the *in-situ* XAFS measurement was triggered off at the same time as the addition of the DMF solution of $NaBH_4$ to the toluene solution. The spectra were measured for 180 s to obtain 1800 spectra. XAFS spectra with good quality were selected and accumulated for each 1 s time-interval to obtain a series of spectra. The spectra of the Au foil (0.1 μm) were measured simultaneously for energy calibration. The Au L_3 and L_2 edge XANES spectral measurements were separately carried out. The data reduction was performed using REX2000 Ver.2.5.9. program (Rigaku). $Au_{11}(PPh_3)_8Cl_3$ as a

reference was prepared as reported elsewhere.[20] $Au_{11}(PPh_3)_8Cl_3$ was identified by using UV-vis. and XAFS spectroscopies.[21] The solution of DT/Au = 2, in which a Au atom exist as $[TOA]Au^+Cl$,[22] also prepared as a reference.

Characterization of electronic property. The XANES spectra were analyzed by using according to Mansour's method to calculate the parameters for the number of *d* band vacancies, although the parameters might not have clear correlation with the numver of d band vacancies in the present case, i.e. AuNPs protected by DT.[11] The L_3 and L_2 XAFS spectra of Au foil were normalized so that the both extended XAFS (EXAFS) oscillations symmetrically overlap one another at greater than 40 eV above the X-ray absorption edge. The areas are determined by using the part of the XANES spectrum that extends from 10 eV below the edge to 15 eV above the edge using Simpson's method. The L_3 and L_2 edge areas for the Au foil, A_{3r} and A_{2r}, are determined to be 1.064×10^4 and 1.67×10^3 $eVcm^{-1}$, respectively, by using the absorption cross sections for the edges: 107.7 and 57.3 cm^2g^{-1} for L_3 and L_2 edge.

The fractional change in the number of *d* band vacancies (unoccupied *d* states) from that of bulk Au, f_d, was defined as

$$f_d = \Delta h_T / (h_T)_{\text{bulk Au}} = (\Delta A_3 + 1.11\Delta A_2) / (A_3 + 1.11A_2)_{\text{bulk Au}} \quad (1)$$

where $\Delta h_T = (h_T)_{\text{sample}} - (h_T)_{\text{bulk Au}}$; $\Delta A_j = (A_j)_{\text{sample}} - (A_j)_{\text{bulk Au}}$; h_T = total number of unoccupied *d* states; A_j = edge area for the *j*th edge.

The h_T was calculated using the follow equation (rearrangement of (1))

$$h_T = (1 + f_d)\, h_{Tr} \quad (2)$$

The change in the vacancies in $d_{5/2}$ and $d_{3/2}$ states were calculated by using the following expressions

$$\Delta h_{5/2} = (2.25\Delta A_3 - 0.5\Delta A_2) / C \quad (3)$$

$$\Delta h_{3/2} = 3\,\Delta A_2 / C \quad (4)$$

where C is constant characteristic of the absorption (C = 75213 $eVcm^{-1}$).[23]

Results and Discussion

Dispersion. Figure 1(a) shows the series of Au L_3 edge XANES spectra during particle formation, together with those of [TOA]$AuCl_4$ in toluene (Au^{3+} solution) and Au foil. The XANES spectrum of Au^{3+} solution has sharp and narrow absorption band around the edge (1192 eV), which is called the white line. The band corresponds to the electronic transition from the $2p_{3/2}$ core level state to the vacant $5d_{3/2}$ and $5d_{5/2}$ states. The XANES spectrum of the Au foil exhibits almost no white line because of the almost fully filled 5*d* state of Au^0. The solution of DT/Au =1 before addition of $NaBH_4$ represented the smaller white line than Au^{3+} solution. This is due to the reduction of an Au^{3+} ion by 2 molecules of DT to from Au^+ ion.[22] In other words, the solution of DT/Au =1 before addition of $NaBH_4$ contains an equal quantity of Au^+ and Au^{3+} ions, which was confirmed by the least squares fitting of the XANES spectrum before the reduction with the linear combination of the those of Au^{3+} and Au^+ solutions.[17] The white line of the solution of DT/Au =1 disappeared immediately after addition of $NaBH_4$, and, alternatively, the small and broad peak appeared just at the high-energy side of the edge (11929 eV). The peak intensity became the strongest at 3.6 s. Previously, the XANES spectrum having the small and broad peak was assigned to that of very small Au clusters during the particle formation process, i.e. nuclei.[17] The intensity of the peak at 3.6 s decreased with time, and the two broad bands at 11948 and 11970 eV appeared. In short, the XANES spectra became similar to that of the Au foil. The spectral change indicates the reduction of Au ions and the formation of AuNPs. Figure 1(b) shows the series of Au L_2 edge XANES spectra, together with those of Au^{3+} solution and Au foil. The L_2 edge XANES spectra of Au^{3+} solution also show the white line at 13735 eV, which is assignable to the electronic transition from and from the $2p_{1/2}$ to $5d_{3/2}$. The white line intensity is smaller than that at the L_3 edge because the white line at the L_2 edge proves the unoccupied $d_{3/2}$ state and that at the L_3 edge probes the unoccupied $d_{3/2}$ and $d_{5/2}$ states. The analysis of the L_2 edge XANES spectrum indicated that the Au atoms in the solution of DT/Au = 1 before reduction consists of an equal quantity of Au^+ and Au^{3+} ions, which is the same result as that of the L_3 spectral analysis. The spectral change at L_2 edge showed the same behavior as that at L_3 edge: immediate disappearance of the white line by addition of $NaBH_4$; appearance of the small and

broad peak at the high-energy side of the edge (13742 eV); decrease of of the intensity of the peak from 3.6 s and appearance of the two small peaks at 13760 and 13783 eV to approach the spectrum of Au foil. Thus, we successfuly observed the spectral change during AuNPs formation not only at Au L_3 edge but also at Au L_2 edge. Here, the influence of DT on the particle growth should be mentioned. The spectra of Au nuclei observed at 3.6 s have the small and broad peak around the edges, which is the characteristic to the AuNPs with Au-S bonds. Thus, DT traps the gold cluster from the beginning of the growth, which will lead slower particle growth in comparison to the growth wihtout DT.

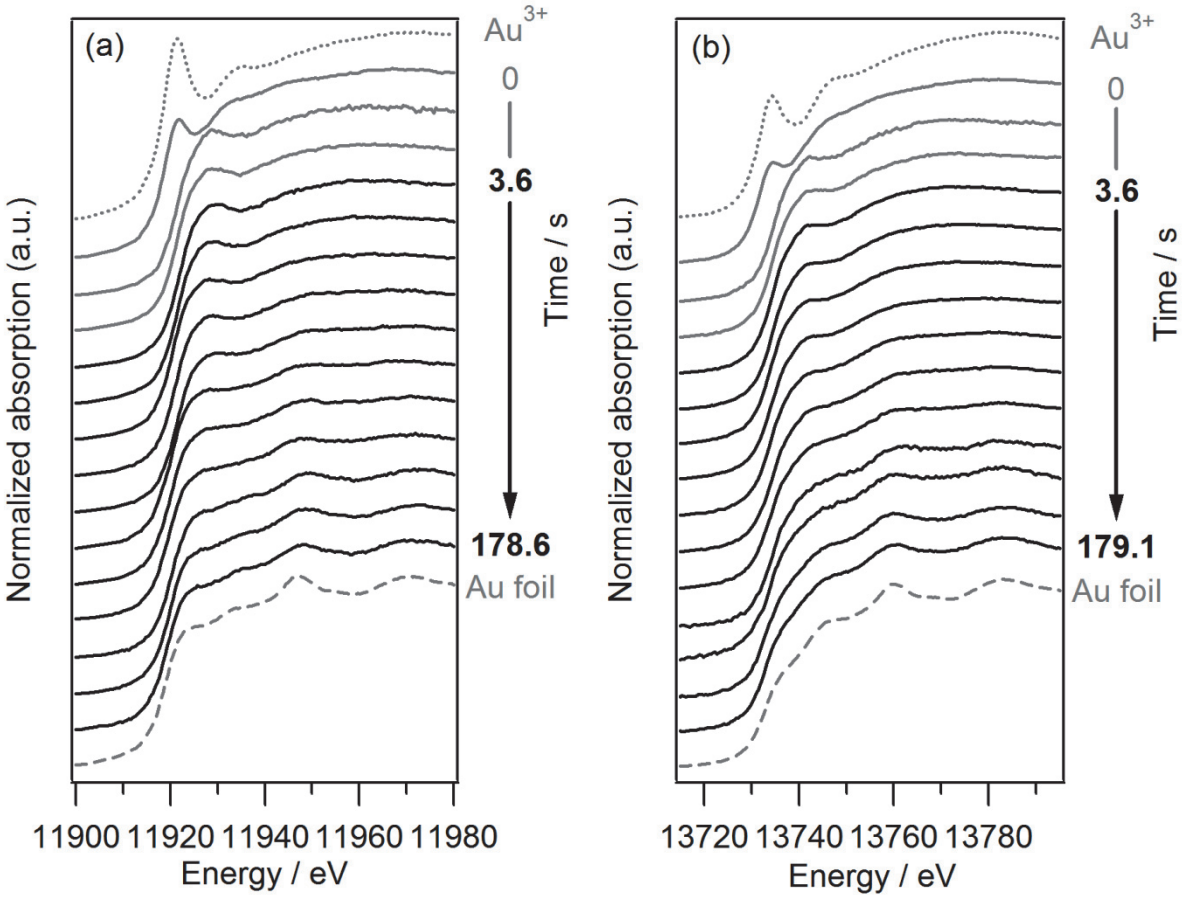

Figure 1. The series of XANES spectra at (a) Au L_3 and (b) L_2 edge during particle formation (solid lines), together with those of $HAuCl_4$ in DMF (Au^{3+} solution) (dotted line) and Au foil (dashed line). The series of spectra during particle formation and that of Au^{3+} solution were shifted vertically for clarity.

The series of Au L_3 edge XANES spectra from 3.6 s to 178.6 s were fitted with the linear combination of the spectrum of the Au nuclei (observed at 3.6 s) and that of Au foil by using the least square method as well as the Au L_2 edge XANES spectra from 3.6 s to 179.1 s, which was verified by by factor analysis. Figure 2 shows the time course of the fractions of the spectrum at 3.6 s and that of Au foil resulting from the fitting. The fractions L_3 edge XANES spectra are almost the same as those of L_2 edge XANES spectra. The fructions of the spectra of Au nuclei and foil respectivelydecreased and increased with time and approached to ca. 70 and 30%. We interpreted the fractions of the spectra of Au nuclei and Au foli as those of the surface and inner atoms of AuNPs, respectively, as previously reported.[17] On the basis of this interpritation, the fractions of the surface and inner atoms decreased and increased with reaction time, respectively, which means the growth of AuNPs from Au nuclei. The fraction of Au foil less than 100 % at 180 s means the formation of AuNPs, because AuNPs have higher surface fraction than Au foil. It is also worth noting that almost all of Au atoms in the reaction solution compose Au nuclei at 3.6 s, because the Au nuclei were observed by the XAFS spectroscopy which provides information of average state of an absorption atom. These results suggest that AuNPs grow via the aggregation of AuNPs themselves.[17,18] As a result, we can estimate the particle size from the fraction of the surface atoms, in other words, the dispersion.

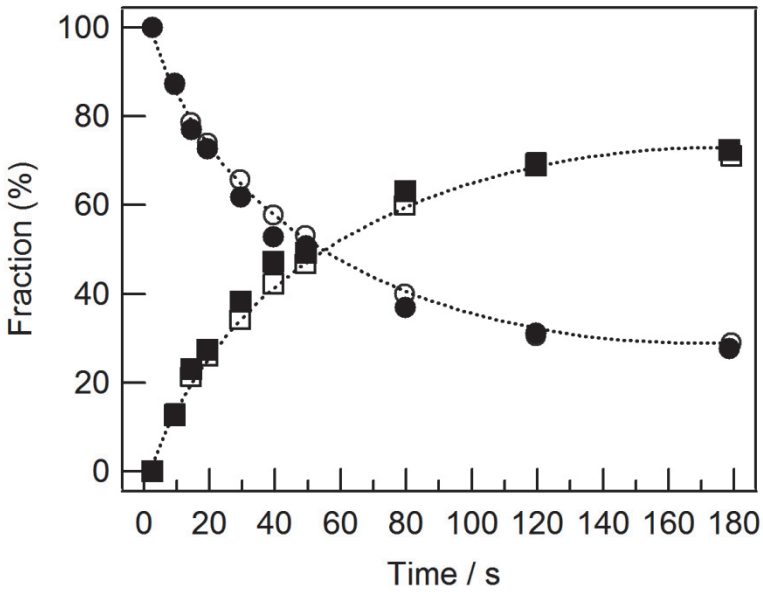

Figure 2. Time course of the fraction of the XANES spectrum of Au nuclei observed at 3.6 s (representing the surface atoms) (circle) and that of Au foil inner atoms (representing the inner atom) (square) after 3.6 s. The fractions were evaluated by least-squares fitting of the series of XANES spectra at Au L_3 (unfilled) and L_2 edges (filled) with linear combination of those of the Au nuclei and Au foil. The resulting R factors are 0.4−1 %.

Electronic state. The series of Au L_3 and L_2 XANES spectra during the particle growth from 3.6 to 180 s showed higher absorption intensity than that of Au foil in the energy region from the edge to 15 eV above the edge as represented by Figure 3. Such spectral feature is characteristic of the XANES spectra of AuNPs protected with DT as reported elsewhere.[14-16] The larger absorption intensities for the AuNPs at the edges have been assumed to be only due to the larger *d* band vacancies of Au atoms of AuNPs than that of Au foil. The *d* band vacancies are resulted from the electron transfer from Au atoms to the adsorbed S atoms of DT.[24] According to this assumption, we analyzed the series of Au L_3 and L_2 edge XANES spectra after the formation of Au nuclei at 3.6 s to evaluate the *h* parameters for the number of *d* band vacancies. The *h* parameters were evaluated from the difference absorption areas between the XANES spectra of a sample and Au foil at L_3 and L_2 edges in

the energy region from 10 eV below the edge to 15 eV above the edge (ΔA_3 and ΔA_2) by using established equations (1-4), assuming that the number of unoccupied *d* states per an Au atom for the bulk Au in total (h_T), in $d_{5/2}$ ($h_{5/2}$), and in $d_{3/2}$ satate ($h_{3/2}$) is 0.401, 0.283, and 0.118, respectively.[25] Table 1 summarized the representative results. The spectrum of $Au_{11}(PPh_3)_8Cl_3$ was also analyzed as a reference. The h_T of Au nuclei (0.525) was slightly larger than that of $Au_{11}(PPh_3)_8Cl_3$, which implies the generation of small Au cluster like the Au_{11} cluster at 3.6 s. This implication accords with our previous proposal of the generation of an Au_4 cluster as an Au nucleus.[17] The h_T decreases with the reaction time, in other words, with the size of AuNPs. The dependence of the h_T value on the size is compatible to the result of Zhang et al., who showed that the percent of *d* band vacancies decreases with the size of AuNPs protected with DT (1.6 nm > 2.4 nm > 4.0 nm),[15] and also the result of MacDonald et al., who investigated the changes of the number of *d* band vacancies of $Au_{25}(SR)_{18}$, $Au_{38}(SR)_{24}$, and $Au_{144}(SR)_{60}$ relative to bulk Au to clarify that the smaller cluster have the larger vacancies in *d* band.[16] We concluded that the analysis described above is an appropriate method for the evaluation of the size dependent XANES spectra of AuNPs protected by thiolate.

Interestingly, the difference in $h_{3/2}$ between a sample and Au foil, $\Delta h_{3/2}$, shows larger value than $\Delta h_{5/2}$ at each time, as listed in Table 1. Generally, the $\Delta h_{3/2}$ should have smaller value than the $\Delta h_{5/2}$ as follow reasons: The splitting of *d* states due to spin-orbit coupling results in $d_{5/2}$ states at higher energies and $d_{3/2}$ states at lower energies; The *d* vacancies are distributed from the higher to lower energy; In the case of Au metal, there are slight d vacancies, which should be largely distributed to $d_{5/2}$ states. However, the $\Delta h_{5/2}$ is not larger than the $\Delta h_{3/2}$ in our case. Zhang et al. also pointed out that the $\Delta h_{3/2}$ for AuNPs protected by DT shows slightly larger value than the $\Delta h_{5/2}$.[14] On the basis of the general understanding of the density of states in *d* band, it is concluded that the h_T, $h_{5/2}$, and $h_{3/2}$ evaluated from the XANES spectral analysis of the AuNPs do not reflect only the number of *d* band vacancies. The other factors will concern in the small and broad bands around the edges in XANES spectra of AuNPs protected by DT.

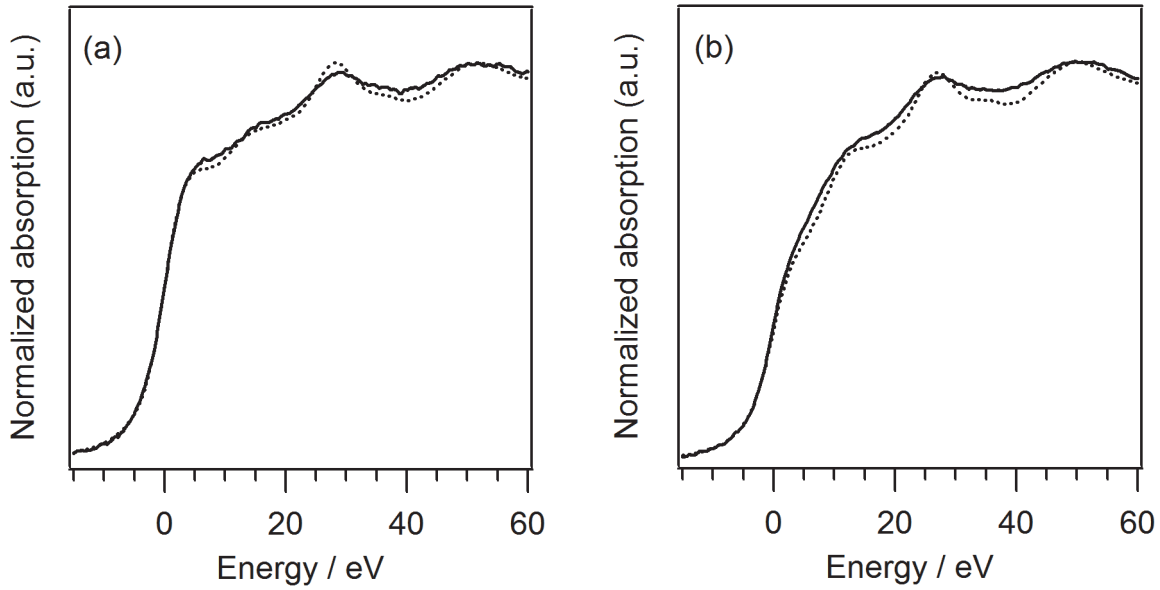

Figure 3. The XANES spectra at (a) Au L_3 and (b) L_2 edges observed at ca. 180 s (solid lines) plotted over those of Au foil (dotted lines).

Table 1. The parameters of AuNPs evaluated from the XANES spectra.

Sample [(a)]	ΔA_3 eVcm^{-1}	ΔA_2 eVcm^{-1}	h_T	$h_{5/2}$	$h_{3/2}$	$\Delta h_{5/2}$	$\Delta h_{3/2}$	Dispersion (%) [(b)]
3.6 s	2138	1545	0.525	0.337	0.180	0.054	0.062	100
9.5 s	1750	1374	0.506	0.326	0.173	0.043	0.055	87.2
19.5 s	1693	1093	0.494	0.326	0.162	0.043	0.044	73.3
39.5 s	1067	711	0.461	0.310	0.146	0.027	0.028	55.3
79.6 s	631	698	0.446	0.297	0.146	0.014	0.028	38.4
178.9 s	309	492	0.428	0.289	0.138	0.006	0.020	28.3
Au foil [(c)]	–	–	0.401	0.283	0.118	–	–	0
$Au_{11}(PPh_3)_8Cl_3$	2017	1141	0.506	0.336	0.164	0.053	0.046	91.0

(a) The average time for the L_3 and L_2 edge XANES spectra.

(b) The average dispersion evaluated from the L_3 and L_2 edge XANES spectra.

(c) Values from ref. (25).

On the other hand, it was reported that the chemisorptions of hydrogen induces changes in the Au L_3 and L_2 edge XANES spectra of AuNPs supported metal oxides as well as in the Pt L_3 and L_2 edge spectra of Pt nanopartices (PtNPs).[26-29] By the chemisorption of hydrogen, the Au L_3 and L_2 edge XANES spectra show higher X-ray absorption intensity in the energy region from the edge to ca. 15 eV above the edge, where the Pt L_3 and L_2 edge XANES spectra represent higher absorption intensity with the chemisorption. The difference absorption spectrum at L_3 edge between the spectra with and without the chemisorption displays almost the same band to that at L_2 edge. If the *d* band vacancies are calculated from almost the same difference absorption spectra at L_3 and L_2 by using the described procedure, the $\Delta h_{3/2}$ should show the larger value than $\Delta h_{5/2}$, which is generally unacceptable for the reason of the density of the state of d band described above. Actually, the origin of the increase in the absorption intensity are considered to be due to the electronic transition to antibonding orbital of metal-H bonds or the multiple scattering of adsorbed H atoms with partially negative charge.[27,30,31] In the case of AuNPs protected by DT, however, these bands are assumed to be due to the *d* band vacancies, it is likely that the higher X-ray absorption intensity of AuNPs around the edges is mainly due to the electronic transition to the unoccupied orbitals of the Au-S bonds, in other words, the Au-S scatterings.[26-28] In fact, the density functional calculation for Au cluster reported by Nobusada presents the main atomic orbital consisting of Au(6s) and S(3s) as LUMO.[32] Furthermore, our proposal is also supported by the fact that [TOA]Au^+Cl, which does not have Au-S bonds, represents no peak around the L_3 and L_2 edges (Figure 4). Therefore, the values of h_T, $h_{5/2}$, and $h_{3/2}$ mainly reflect the scattering intensity of Au-S pair, and might contain the information about the *d* band vacancies.

With the understanding about the values of $h_{5/2}$ and $h_{3/2}$, the values were plotted against the dispersion as shown in Figure 5. The $h_{3/2}$ almost linearly decreased with the dispersion, which indicates that the net vacancies in $d_{3/2}$ states are too small to appear in the variation of $h_{3/2}$ in comparison with the amplitude of the Au-S scatterings.

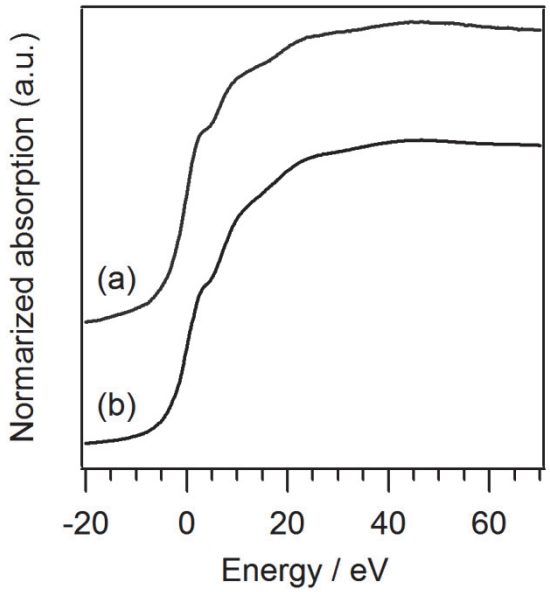

Figure 4. The Au (a) L_3 and (b) L_2 edge XANES spectra of the solution of [TOA]$Au^{+}Cl$.

On the other hand, the value of $h_{5/2}$ also decreased with the dispersion, however not in a linear fashion. This result suggests that the value of $h_{5/2}$ reflects not only the Au-S scatterings but also the electronic properties of the AuNPs. Figure 6 shows the Au L_3 and L_2 edge XANES spectra at ca. 180 s with those synthesized by the linear combination of those of the Au nuclei at 3.6 s and Au foil. The synthesized XANES spectrum at L_3 edge showed slightly stronger intensity than the experiment one in the energy region from the edge to 15 eV above the edge. The stronger intensity of the synthesized spectrum agrees with the non-linear decrease of the value of $h_{5/2}$ with the dispersion, particularly at the low dispersion. On the other hand, the synthesized spectrum at L_2 edge well accords with the measurement one in the energy region from the edge to 15 eV above the edge, which conforms to the linear decrease of $h_{3/2}$ with the dispersion. It is concluded that the value of $h_{5/2}$ reflects the *d* band vacancies of AuNPs and that of $h_{3/2}$ hardly signifies it due to the large contribution of the Au-S scatterings.

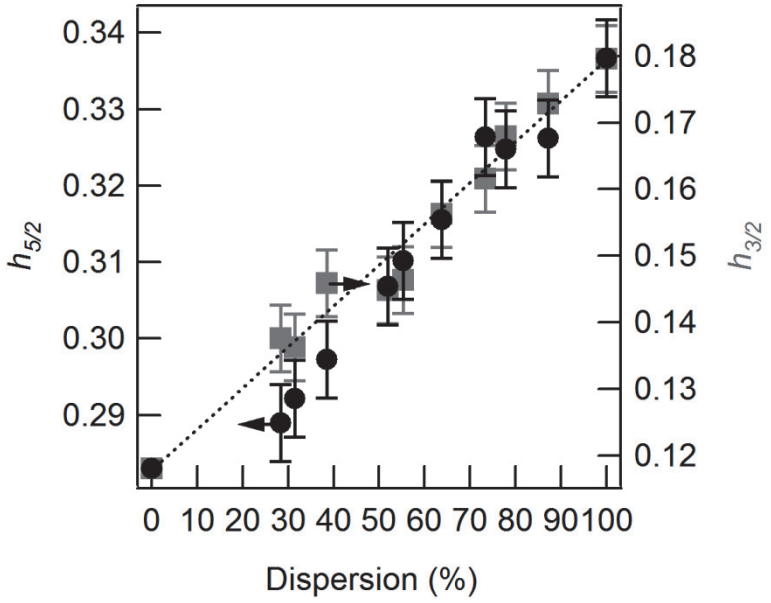

Figure 5. (a) The values of $h_{5/2}$ (circle) and (b) $h_{3/2}$ (square) plotted against the dispersion evaluated from the XANES spectral analysis.

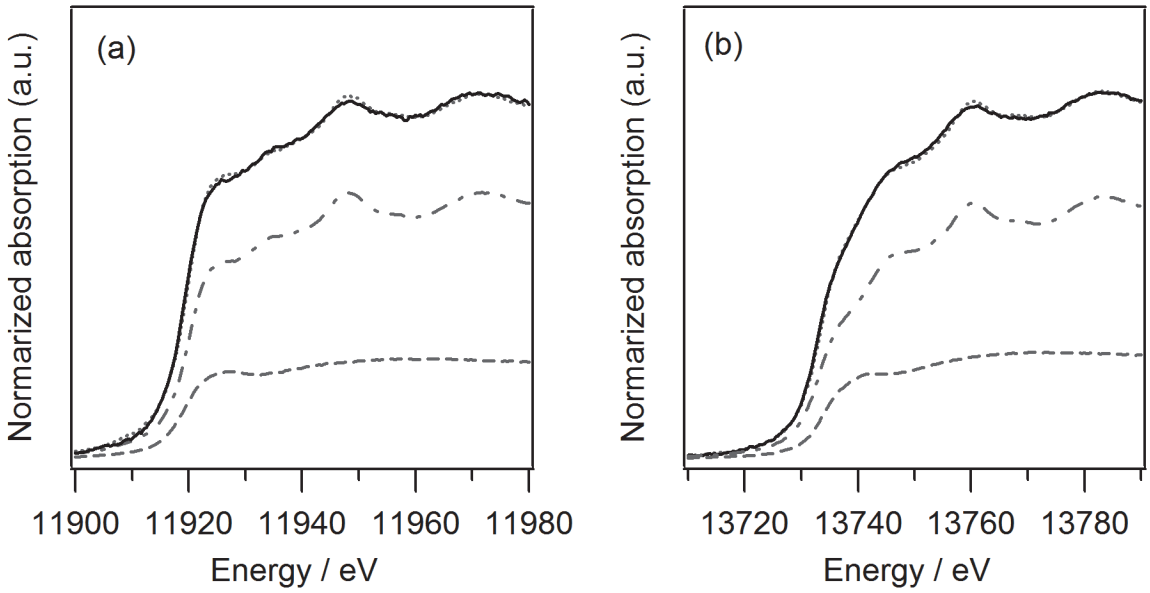

Figure 6. The measurement XANES spectra at ca. 180 s (solid line) and the synthesized spectra (dotted line) with the linear combination of those of Au nuclei at 3.6 s (dashed line) and Au foil (dashed-dotted line) at (a) Au L_3 and (b) L_2 edges.

Figure 7 displays the variation of the value of $h_{5/2}$ with the diameter of AuNPs. The diameter was estimated from the dispersion evaluated by XANES analysis on the assumption of spherical AuNPs and 0.288 nm of Au atomic distance. In Figure 7, the AuNPs having 20-nm diameter was presumed to have the same value of *d* vacancies as that of bulk Au (the calculated dispersion of AuNPs with 20-nm diameter is 8.4%). The value of $h_{5/2}$ did not increase according to the inverse of the diameter, but exponentially increased with a decrease in the diameter. This change in the value of $h_{5/2}$ suggests that the electrons of Au atoms are additionally transferred to the S atoms of DT as the size of AuNPs decreases. The additional electron transfer might be the intrinsic size effect of AuNPs. The size dependent catalytic activity has been attracting a lot of attention in catalysis science. There are reports on the catalytic activities deviated the size of AuNPs, for example, the oxidation of p-hydroxybenzaldehyde using AuNPs protected by poly(N-vinyl-2-pyrroridone) (PVP) and glucose oxidation on AuNPs supported by active carbon.[4,33] These catalytic activities deviated from the size are well consistent with the variation of the $h_{5/2}$ parameters with the size investigated in this study. The deviated electron transfer from AuNPs to the adsorbate (DT) observed in this study is assumed to contribute to the activation of O_2 in the catalytic reaction. In fact, it has been proposed that O_2 gains electron to form the reactive oxygen species on AuNPs.[4,34] On the other hand, in catalytic reactions on AuNPs supported by metal oxides, it have been proposed that the contact structure of AuNPs with the metal oxide supports and the function of the supports largely contribute on the reactivity.[35,36] Metal oxide supports would have more significant effect on the function of AuNPs than PVP and active carbon. But, it was also reported that AuNPs with 2-nm diameter on TiO_2 shows the property like Pt and Pd.[37] In addition, the unique catalytic activity of AuNPs was accounted by the quantum size effect.[38,39] These results suggest that the electronic property of AuNPs also attributes to the catalysis of AuNPs supported by metal oxides. Thus, the evaluation of the electronic properties of AuNPs is important to understand the origin of unique properties. In this connection, we will conduct further study on the evaluation of electronic property of AuNPs using X-ray absorption spectroscopy.

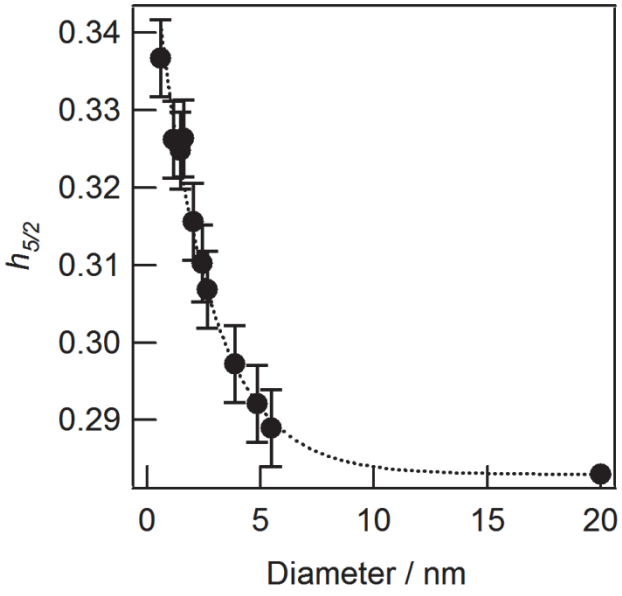

Figure 7. The variation of the value of $h_{5/2}$ with the diameter calculated from the dispersion evaluated from the XANES spectral analysis.

Conclusion

The formation process of AuNPs in the presence of DT was observed *in situ* by means of the QXAFS spectroscopy at Au L_3 and L_2 edges. The spectra of small AuNPs during particle growth represented the higher absorption intensity around the edges in comparison with Au foil. The XANES spectral analysis revealed that the higher absorption intensity was mainly attributable to the Au-S scatterings, and slightly to the *d* band vacancies of Au metal species. The slight contribution of the *d* band vacancies did not appear in the value of $h_{3/2}$ due to the much larger contribution of the Au-S scatterings than that of the vacancies in $d_{3/2}$ state. On the other hand, the value of $h_{5/2}$ reflected the contribution of the *d* band vacancies under the large contribution of the Au-S scatterings. The variation of the value of $h_{5/2}$ with the size of AuNPs implied the intrinsic properties of AuNPs deviated from the size.

References

(1) Jin, R. C. *Nanoscale* **2010**, *2*, 343.

(2) Haruta, M. *Catal. Today* **1997**, *36*, 153.

(3) Hu, M.; Chen, J.; Li, Z.-Y.; Au, L.; Hartland, G. V.; Li, X.; Marquez, M.; Xia, Y. *Chem. Soc. Rev.* **2006**, *35*, 1084.

(4) Tsunoyama, H.; Ichikuni, N.; Sakurai, H.; Tsukuda, T. *J. Am. Chem. Soc.* **2009**, *131*, 7086.

(5) Brust, M.; Walker, M.; Bethell, D.; Schiffrin, D. J.; Whyman, R. *Chem. Commun.* **1994**, 801.

(6) Ohyama, J.; Hitomi, Y.; Higuchi, Y.; Shinagawa, M.; Mukai, H.; Kodera, M.; Teramura, K.; Shishido, T.; Tanaka, T. *Chem. Commun.* **2008**, 6300.

(7) Enüstün, B. V.; Turkevich, J. *J. Am. Chem. Soc.* **1963**, *85*, 3317.

(8) Schmid, G.; Boese, B.; Pfeil, R.; Bandermann, F.; Meyer, S.; Calis, G. H. M.; van der Velden, J. W. A. *Chem. Ber.* **1981**, *114*, 3634.

(9) Yonezawa, T.; Yasui, K.; Kimizuka, N. *Langmuir* **2001**, *17*, 271.

(10) Hitomi, Y.; Ohyama, J.; Higuchi, Y.; Aoki, K.; Shishido, T.; Funabiki, T.; Kodera, M.; Tanaka, T. *Bull. Chem. Soc. Jpn.* **2010**, *83*, 1392.

(11) Mansour, A. N.; Cook, J. W.; Sayers, D. E. *J. Phys. Chem.* **1984**, *88*, 2330.

(12) Ebitani, K.; Tanaka, T.; Hattori, H. *Appl. Catal. A* **1993**, *102*, 79.

(13) Zanchet, D.; Tolentino, H.; Alves, M. C. M.; Alves, O. L.; Ugarte, D. *Chem. Phys. Lett.* **2000**, *323*, 167.

(14) Zhang, P.; Sham, T. K. *Appl. Phys. Lett.* **2002**, *81*, 736.

(15) Zhang, P.; Sham, T. K. *Phys. Rev. Lett.* **2003**, *90*, 245502.

(16) MacDonald, M. A.; Zhang, P.; Qian, H.; Jin, R. *J. Phys. Chem. Lett.* **2010**, *1*, 1821.

(17) Ohyama, J.; Teramura, K.; Higuchi, Y.; Shishido, T.; Hitomi, Y.; Kato, K.; Tanida, H.; Uruga, T.; Tanaka, T. *ChemPhysChem* **2011**, *12*, 127.

(18) Duff, D. G.; Baiker, A.; Edwards, P. P. *Langmuir* **1993**, *9*, 2301.

(19) Uruga, T.; Tanida, H.; Inoue, K.; Yamazaki, H.; Irie, T. *AIP Conf. Proc.* **2007**, *882*, 914.

(20) Woehrle, G. H.; Warner, M. G.; Hutchison, J. E. *J. Phys. Chem. B* **2002**, *106*, 9979.

(21) Benfield, R. E.; Grandjean, D.; Kroll, M.; Pugin, R.; Sawitowski, T.; Schmid, G. *J. Phys. Chem. B* **2001**, *105*, 1961.

(22) Goulet, P. J. G.; Lennox, R. B. *J. Am. Chem. Soc.* **2010**, *132*, 9582.

(23) Tyson, C. C.; Bzowski, A.; Kristof, P.; Kuhn, M.; Sammynaiken, R.; Sham, T. K. *Phys. Rev. B* **1992**, *45*, 8924.

(24) Hakinen, H.; Barnett, R. N.; Landman, U. *Phys. Rev. Lett.* **1999**, *82*, 3264.

(25) Mattheiss, L. F.; Dietz, R. E. *Phys. Rev. B* **1980**, *22*, 1663.

(26) Bus, E.; Miller, J. T.; van Bokhoven, J. A. *J. Phys. Chem. B* **2005**, *109*, 14581.

(27) Kubota, T.; Asakura, K.; Ichikuni, N.; Iwasawa, Y. *Chem. Phys. Lett.* **1996**, *256*, 445.

(28) Kubota, T.; Asakura, K.; Iwasawa, Y. *Catal. Lett.* **1997**, *46*, 141.

(29) Oudenhuijzen, M. K.; van Bokhoven, J. A.; Miller, J. T.; Ramaker, D. E.; Koningsberger, D. C. *J. Am. Chem. Soc.* **2005**, *127*, 1530.

(30) Samant, M. G.; Boudart, M. *The Journal of Physical Chemistry* **1991**, *95*, 4070.

(31) Soldatov, A. V.; Della Longa, S.; Bianconi, A. *Solid State Commun.* **1993**, *85*, 863.

(32) Nobusada, K. *J. Phys. Chem. B* **2004**, *108*, 11904.

(33) Comotti, M.; Della Pina, C.; Matarrese, R.; Rossi, M. *Angew. Chem. Int. Ed.* **2004**, *43*, 5812.

(34) Okumura, M.; Kitagawa, Y.; Haruta, M.; Yamaguchi, K. *Chem. Phys. Lett.* **2001**, *346*, 163.

(35) Boccuzzi, F.; Chiorino, A.; Manzoli, M.; Lu, P.; Akita, T.; Ichikawa, S.; Haruta, M. *J. Catal.* **2001**, *202*, 256.

(36) Haruta, M. *The Chemical Record* **2003**, *3*, 75.

(37) Hayashi, T.; Tanaka, K.; Haruta, M. *J. Catal.* **1998**, *178*, 566.

(38) Valden, M.; Lai, X.; Goodman, D. W. *Science* **1998**, *281*, 1647.

(39) Cunningham, D. A. H.; Vogel, W.; Kageyama, H.; Tsubota, S.; Haruta, M. *J. Catal.* **1998**, *177*, 1.

Part II

Formation Mechanism and Characterization of Photodeposited Metal Nanoparticles

Introduction of Part II

Photodeposition

When a semiconductor catalyst is illuminated with photons equal to or greater than the band gap energy (e.g. $h\nu \geq 3.2$ eV, anatase crystalline phase of TiO_2), electrons and holes are formed in the conduction and valence bands, respectively (1).

$$h\nu \rightarrow e^- + h^+ \qquad (1)$$

In 1978, Bard et al. illuminated TiO_2 in the aqueous solution containing H_2PtCl_6, and hydroquinone.[1] The photo-formed electrons in TiO_2 reduced Pt ions to deposit Pt metal on TiO_2. The metal deposition on photocatalysts in such a manner is called photodeposition. In case that metal ions have more positive redox potential than the conduction band level of a photocatalyst, a photodeposition reaction proceeds. In order to carry out a photodepostion smoothly, organic substances such as alcohol, aldehyde, and carboxylic acid are used as sacrificial reagents which consume the photo-formed holes. Although Bard et al. used hydroquinone as a sacrificial reagent, alcohols are the most frequently applied among various sacrificial reagents.

Metal modification on a photocatalyst is often helpful to improve the photocatalytic activity, because of prompt charge separation by trap of photo-formed electron by metals as well as their intrinsic catalytic properties. Photodepostion method is one of the most useful methods to modify a photocatalyst with metals. The photodeposition method is also utilized for recovery of noble metal, removal of metal cations from aqueous effluents.[2]

Photo-formed electrons and holes in TiO_2 and Metal-TiO_2 in the presence of alcohols

Here, the author summarizes the photo induced reaction on a surface of TiO_2 in the presence of alcohols and absence of oxygen, which is a general condition for photodeposition.

The photo-formed holes are trapped by hydroxyl groups on the surface of TiO_2 (1), by alkoxides adsorbed on TiO_2 (2), or recombined with the photo-formed electrons (3).

$$h^+ + HO(a)^- \rightarrow HO\cdot(a) \qquad (1)$$

$$h^+ + RO(a)^- \rightarrow RO\cdot(a) \qquad (2)$$

$$e^- + h^+ \rightarrow h\nu \text{ or } \Delta \text{ (light or heat)} \qquad (3)$$

where h^+ represents the photo-formed holes, e^- represents the photo-formed electrons, $OH(a)^-$ and $RO(a)^-$ refer to hydroxyl group of TiO_2 and adsorbed alkoxide, respectively, and $HO\cdot(a)$ and $RO\cdot(a)$ presents the hole trapped by $OH(a)^-$ and $RO(a)^-$, respectively. When the recombination is enacted, the $OH(a)^-$ and $RO(a)^-$ successively accept the holes and are oxidized into oxygen and carbon dioxides, respectively, by consuming lattice oxygen of TiO_2.

The trapping of holes by hydroxyl groups is required an average time of 250 ns.[3,4] The adsorbed alkoxides trap the holes faster than the hydroxyl groups of TiO_2.[3,5] For example, methoxide traps the holes within ps–1 ns.[3,5] On the other hand, the time range for recombination is ps–10 μs,[4,6,7] which is much faster than the time for trap of holes by $OH(a)^-$ and compatible to that by $RO(a)^-$. In the absence of alcohols, the recombination dominantly occurs and the photoreaction poorly proceeds. Therefore, alcohols cause an efficient charge separation and promote reduction of metal ions and proton to produce metals and hydrogen.

While the photo-formed holes are trapped or consumed, the photo-formed electrons tend to move from Ti^{4+} to Ti^{3+} defect sites in TiO_2, because the energy level of Ti^{3+} is lower than the bottom of the conduction band of Ti^{4+}.[8] In the presence of metals on TiO_2, the photo-formed electrons can be trapped by the metals (4).

$$e^- + M \rightarrow e^-[M] \qquad (4)$$

where M represents metal, and $e^-[M]$ refers to electrons trapped by metal. In the case that Pt is deposited on TiO_2, the photo-formed electrons are captured by Pt within fs–10 ps,[6,9,10] which is compatible to the time for the recombination reaction (3). Thus, metals deposited on TiO_2 suppress the recombination, in other words, metals improve the charge separation.

Metal Particle Formation Mechanism for Photodeposition

The photodeposition mechanism has been investigated by Herrmann's group.[11-16] They proposed the mechanism as follows: adsorption of metal complex on TiO_2 (5), creation of electron-hole pair in TiO_2 by photoirradiation (6), reduction of metal complex (7), and formation of metal particles through aggregation of individual zerovalent metal atoms (8a) or

through cathodic-like reduction of metal ions on small metal nuclei.

$$M^{n+}(s) \rightleftarrows M^{n+}(a) \quad (5)$$

$$TiO_2 + hn \rightarrow e^- + h^+ \quad (6)$$

$$M^{n+} \rightarrow M^0(a) \quad (7)$$

$$mM^0(a) \rightarrow M_m \quad (8a)$$

$$M_0 \xrightarrow{+M^{n+}} M_2^{n+} \xrightarrow{+ne^-} M_2^0 \xrightarrow{+M^{n+}} M_3^{n+} \xrightarrow{+ne^-} M_3^0 \rightarrow \cdots \rightarrow M_m^0 \quad (8b)$$

where $M^{n+}(s)$, $M^{n+}(a)$, and $M^0(a)$, represents metal ions in solution, those adsorbed on TiO_2, zerovalent metal atoms adsorbed on TiO_2, respectively; M^{n+} refers to $M^{n+}(s)$ or $M^{n+}(a)$; M_m^{n+} and M_m^0 present metal particle with metal ion and metal particle, respectively. The adsorption of metal ions represented by reaction (5) is Langmuir type. The generation of electron-hole pair (reaction (6)) proceeds as described above. As for the reaction (7), Ferrnandez et al. analyzed a photodeposition in gas/solid interface by the *in situ* X-ray photoelectron spectroscopy (XPS) and presented that Pt^{4+} and Rh^{3+} ions were reduced to metal through Pt^{2+} and Rh^+, while Pd^{2+} ions are reduced directly to metal.[17] However, the photodeposition is usually carried out in liquid/solid interface and not in gas/solid interface. The reduction of metal ions should be investigated in the usual liquid/solid interface. The particle formation reaction occurs on TiO_2 (8a) or on metal (8b). Herrmann et al. reported the reduction of Pt ions on the predeposited Ag particles when anatase phase TiO_2 was used. In the case of rutile phase TiO_2, Pt ions were reduced on TiO_2 to form Pt particles.[16] These results implied that the reaction (8a) proceeds on anatase TiO_2 and the reaction (8b) on the rutile TiO_2. On the other hand, Ferrnandez et al. successfully observed the photodeposition process of Au particles on TiO_2 by means of *in situ* X-ray absorption fine structure (XAFS) spectroscopy, although they could not clarify the photodeposition mechanism.[12,13] The XAFS spectroscopy will be the most powerful tool to analyze photodeposition, because it can be applied without regard to the states of samples and provide information about the electronic state and the structure of absorption atom.

It is proposed that metal nanoparticles are formed at the defect sites of TiO_2 in photodeposition process.[18,19] The defect sites can be formed by the reduction of TiO_2 by

photo-formed electrons. In fact, the Ti^{3+} is easily formed by photoirradiation to TiO_2 in the presence of alcohols and absence of oxidant such as metal ion and O_2.[20] On the other hand, it is well known that the Ti^{3+} in TiO_2 strongly interact with metal particles and it can migrate on the surface of metal particles.[21,22] Therefore, the interaction of metal particles and TiO_2 in photodeposition should contribute the photodeposition mechanism. Furthermore, the interaction significantly affect on the catalytic property.[21,22] However, there is a few studies dealing with the interaction in metal modifying photocatalyst prepared by photodeposition.[23,24]

Survey of Part II

On these backgrounds, the author studied the photodeposition mechanism mainly by means of *in situ* time resolved XAFS spectroscopy. In chapter 6, the photodeposition mechanism of Rh nanoparticles on TiO_2 is described. The author proposes a new and unique particle formation mechanism. Additionally, in this study, an interesting structure of Rh nanoparticles was observed, which indicated the strong interaction between Rh and TiO_2. On the basis of these results, in chapter 7, the structure of metal nanoparticles photodeposited on photocatalyst was analyzed and the modification of metal with TiO_2 during photodeposition process is proposed.

References

(1) Kraeutler, B.; Bard, A. J. *J. Am. Chem. Soc.* **1978**, *100*, 4317.

(2) Herrmann, J. M. *Catal. Today* **1999**, *53*, 115.

(3) Tamaki, Y.; Furube, A.; Murai, M.; Hara, K.; Katoh, R.; Tachiya, M. *J. Am. Chem. Soc.* **2005**, *128*, 416.

(4) Rothenberger, G.; Moser, J.; Graetzel, M.; Serpone, N.; Sharma, D. K. *J. Am. Chem. Soc.* **1985**, *107*, 8054.

(5) Chen, T.; Feng, Z.; Wu, G.; Shi, J.; Ma, G.; Ying, P.; Li, C. *J. Phys. Chem. C* **2007**, *111*, 8005.

(6) Iwata, K.; Takaya, T.; Hamaguchi, H.; Yamakata, A.; Ishibashi, T.-a.; Onishi, H.;

Kuroda, H. *J. Phys. Chem. B* **2004**, *108*, 20233.

(7) Furube, A.; Asahi, T.; Masuhara, H.; Yamashita, H.; Anpo, M. *J. Phys. Chem. B* **1999**, *103*, 3120.

(8) Thompson, T. L.; Yates, J. T. *Chem. Rev.* **2006**, *106*, 4428.

(9) Ohtani, B.; Bowman, R. M.; Colombo, D. P.; Kominami, H.; Noguchi, H.; Uosaki, K. *Chem. Lett.* **1998**, 579.

(10) Furube, A.; Asahi, T.; Masuhara, H.; Yamashita, H.; Anpo, M. *Che. Phys. Lett.* **2001**, *336*, 424.

(11) Herrmann, J.-M.; Mansot, J.-L. *J. Catal.* **1990**, *121*, 340.

(12) Caballero, A.; Gonzalezelipe, A. R.; Fernandez, A.; Herrmann, J. M.; Dexpert, H.; Villain, F. *J. Photochem. Photobiol. A* **1994**, *78*, 169.

(13) Fernandez, A.; Caballero, A.; Gonzalez-Elipe, A. R.; Herrmann, J.-M.; Dexpert, H.; Villain, F. *J. Phys. Chem.* **1995**, *99*, 3303.

(14) Herrmann, J. M.; Disdier, J.; Pichat, P. *J. Phys. Chem.* **2002**, *90*, 6028.

(15) Herrmann, J.-M.; Disdier, J.; Pichat, P. *J. Catal.* **1988**, *113*, 72.

(16) Sclafani, A.; Herrmann, J. M. *J. Photochem. Photobiol. A* **1998**, *113*, 181.

(17) Fernandez, A.; Gonzalez-Elipe, A. R. *Appl. Surf. Sci.* **1993**, *69*, 285.

(18) Molina, L. M.; Rasmussen, M. D.; Hammer, B. *J. Chem. Phys.* **2004**, *120*, 7673.

(19) Kowalska, E.; Abe, R.; Ohtani, B. *Chem. Commun.* **2009**, 241.

(20) Takeuchi, M.; Deguchi, J.; Sakai, S.; Anpo, M. *Appl. Catal. B* **2010**, *96*, 218.

(21) Tauster, S. J.; Fung, S. C.; Baker, R. T. K.; Horsley, J. A. *Science* **1981**, *211*, 1121.

(22) Tauster, S. J.; Fung, S. C.; Garten, R. L. *J. Am. Chem. Soc.* **1978**, *100*, 170.

(23) Wang, X. C.; Yu, J. C.; Yip, H. Y.; Wu, L.; Wong, P. K.; Lai, S. Y. *Chem. Eur. J.* **2005**, *11*, 2997.

(24) Lin, C. H.; Chao, J. H.; Liu, C. H.; Chang, J. C.; Wang, F. C. *Langmuir* **2008**, *24*, 9907.

Chapter 6

Investigation of Formation Process of Photodeposited Rh Nanoparticles on TiO_2 by In Situ Time-Resolved Energy-Dispersive XAFS Analysis

Abstract

The photodeposition process of Rh metal nanoparticles on a TiO_2 photocatalyst from $RhCl_3$ aqueous solution in the presence of methanol as a sacrificial oxidant, which consists of the direct reduction process of Rh^{3+} ions to Rh metal and the formation process of Rh nanoparticles, was uncovered by *in situ* time-resolved energy-dispersive X-ray absorption fine structure (DXAFS) analysis in liquid-solid suspension state. The fractions of Rh metal particle and Rh^{3+} precursor were estimated by least-squares fitting of each X-ray absorption near edge structure (XANES) spectrum by linear combination of authentic spectra corresponding to Rh^0 and Rh^{3+}. The fraction of Rh metal linearly increased with photoirradiation time and saturated after 90 min photoirradiation. The coordination number (Rh-Rh pair) was evaluated by the curve fitting of the Rh-Rh scattering at 2.45 Å in the Fourier transforms (FT) of extended XAFS (EXAFS) spectra. The coordination number linearly increased with photoirradiation time and attained constant value, 10 at 90 min of photoirradiation. This value is lower than that of Rh foil (12). These suggest that the formation of fine Rh metal nanoparticles on TiO_2. In addition, the diminution rate of Rh^{3+} ions determined by the ICP analysis gave close agreement with the increase rates of the fraction of Rh metal particles estimated by the XANES spectra and the coordination number (Rh-Rh pair) evaluated by the FT of EXAFS spectra. This result strongly supports that the electrons generated by a charge separation reduce the Rh^{3+} precursor to the Rh metal particle at a moment of time and at a constant rate. The Rh particles do not grow up in incremental steps but the Rh particles with a uniform size appear one after another on the surface.

Introduction

In situ time resolved X-ray absorption fine structure (XAFS) measurement has attracted attention to analyze a time-dependent variation on active sites of catalysts[1] or a formation process of metal particles.[2] Recently, it is desirable to observe a slight chemical change on the nanosecond time scale in the field of magnetism, electronics, and catalyt. Energy-dispersive XAFS (DXAFS) method provided by Matsushita et al. allows the spectral measurement within a few seconds, because white X-ray with ca. 1000 eV of energy range which is dispersed using bent crystal as polychromator is radiated to the sample at the focal point of the dispersed X-ray.[3] We can perform the DXAFS measurement of high-quality XAFS spectra at the synchrotron radiation source supplying irradiation light with very high photon flux. The DXAFS analysis currently is applied to some catalytic reactions to clarify the kinetics and the dynamics of these processes because the structural information (coordination number and bond length around target element) of sample is more quickly obtained without regard to configuration, phases, and atmosphere *in situ*.[1,2,4] We have studied the photodeposition of Rh metal particles on TiO_2 in the suspension state by in situ DXAFS analysis and reported as an letter.[4]

Photodeposition is one of the most popular methods in order to recover noble metal, to remove metal cations from aqueous effluents,[5] and to prepare supported metal catalysts[6-8] and photocatalyst.[9] Bard et al. firstly illuminated the suspension consisting of H_2PtCl_6 as a precursor, hydroquinone as a sacrificial reagent, and TiO_2 as a photocatalyst to modify TiO_2 with platinum nanoparticle.[8] Electrons and holes are generated by UV light irradiation to TiO_2. The electrons reduce metal cations which have more positive redox potential than the conduction band level of TiO_2, while the holes in the valence band are consumed to react with a sacrificial reagent such as alcohol, aldehyde and carboxylic acid to promote the photodeposition smoothly.[6,8,10] Several papers reported that the photodeposited metal species modify specific sites of a photocatalyst, for example, an edge or plane of photocatalyst, and vary their morphology with properties and structures of photocatalyst. There are a few studies dealing with systematic kinetics, and reaction mechanism of the photodeposition and structure of the photodeposited metal species,[4,11] although many research groups employed it

as a modification method and reported photocatalytic activity of various kinds of metal modifying photocatalysts.

Fernandez et al. have observed the photodeposition process of Au particles by *in situ* XAFS measurement, in which the suspension composed of Au precursor and TiO_2 was pumped out under photoirradiation from the photochemical reactor to the XAFS measurement cell.[12] Their experimental set-up for *in situ* XAFS analysis is laid out properly to obtain a good XAFS spectrum on the minute time scale. In this study, we carried out the photodeposition process and analyzed the behavior of photodeposition of Rh metal particles on a TiO_2 photocatalyst in the suspension by means of the *in situ* time-resolved DXAFS spectroscopy on the second time scale. Furthermore, the Rh ions adsorbed on TiO_2 and the Rh metal particles photodeposited under various conditions were characterized by means of ordinary XAFS spectroscopy, XRD, UV-vis. spectroscopy, transmission electron microscopy (TEM), and energy dispersive X-ray spectroscopy (EDX). These analyses indicated the unique formation mechanism of Rh metal particles on TiO_2..

Experimental Section

Photodeposition of Rh on TiO_2 was carried out in a closed batch system. As a typical photodeposition method, 500 mg of TiO_2 (JRC-TIO-8, anatase phase) calcined at 673 K in air was suspended in 3.2 mL of methanol in the batch reactor made of Pylex® glass with a flat ceiling window for irradiation, followed by addition of 0.8 mL of $RhCl_3 \cdot H_2O$ (Wako Pure Chemical Industries, Ltd.) aqueous solution (Rh: 0.076 mmol). The suspension was irradiated with a 200-W Hg-Xe lamp equipped with fiber optics, collective lens, and a mirror (San-Ei Electric Co., Ltd., UVF-204S type C) after Ar bubbling for 10 min. The suspension after a given time phnotoirradiation was filtered and the residual powder was washed with purified water, followed by dryness at 353 K.

UV-vis. diffuse reflectance spectra were collected by a JASCO V-670 spectrometer equipped with an integrating sphere. Spectralon® supplied from Labsphere Inc. was adopted as a standard reflection sample. The UV-vis. reflectance spectra of the powder were measured

and transformed with the Kubelka-Munk function. XRD patterns were recorded with a Rigaku Multiflex powder X-ray diffractometer (Cu $K\alpha_1$ irradiation, λ = 1.5406 Å). The amount of residual Rh ions in the filtrate was determined by a sequential inductively-coupled plasma (ICP) spectrometer (SHIMAZU ICPS-1000IV). The suspensions after the given photoirradiation periods were filtered off and the filtrates were diluted with 100 mL of water. The static XAFS measurements at Rh-K edge were carried out on BL01B1 beamline of the SPring-8 with a Si(311) two-crystal monochromator. Ion chambers of I and I_0 detector were filled with Ar(100%) flow and Ar(75%)/Kr(25%) flow, respectively. The X-ray energy was calibrated with a spectrum of Rh foil. The XAFS spectra of all of the samples were measured in the transmission mode. Data reduction of XAFS spectra was performed using REX2000 program Ver. 2.5.9 (Regaku Corp.). The k^3-weighted EXAFS oscillation in the range of 2.8-15.7 $Å^{-1}$ was Fourier-transformed. The curve-fitting of Fourier-filtered EXAFS spectrum was performed by using empirical parameters extracted from the static XAFS spectrum of Rh foil.

The *in situ* time resolved DXAFS measurements at Rh-K edge (~23.2 keV) were performed on BL28B2 beamline at the SPring-8 synchrotron radiation facility (8 GeV, 100 mA) of the Japan Synchrotron Raciation Research Institute (JASRI) in Hyogo, Japan. The DXAFS measurement system consists of a polychromator set to a Laue configuration with a net plane Si(422) and a position-sensitive detector (PSD) mounted on a θ- 2θ diffractometer as shown in Scheme 1. The X-ray energy was calibrated by a spectrum of Rh foil. The above-mentioned Pylex® reactor with the suspension was set at the X-ray focal spot. Light irradiation to the reactor was synchronized with exposure to X-ray. Scheme 2 shows the timetable of the DXAFS measurement in this study. The exposure time of the PSD was 267 msec. Fifty shots were accumulated, 13.35 sec per a spectrum. We programmed collecting 500 snapshot spectra (134 sec) in the dark and then 6050 snapshot spectra (1614 sec) under photoirradiation consecutively. This measurement program was repeated 4 times to obtain spectral change for 107.6 min under photoirradiation. Data reduction of XAFS spectra was performed as described above. The k^3-weighted EXAFS oscillation in the range of 2.64-10.5 $Å^{-1}$ was Fourier-transformed.

Scheme 1. The main equipment of the DXAFS spectroscopy system at the BL28B2 beamline.

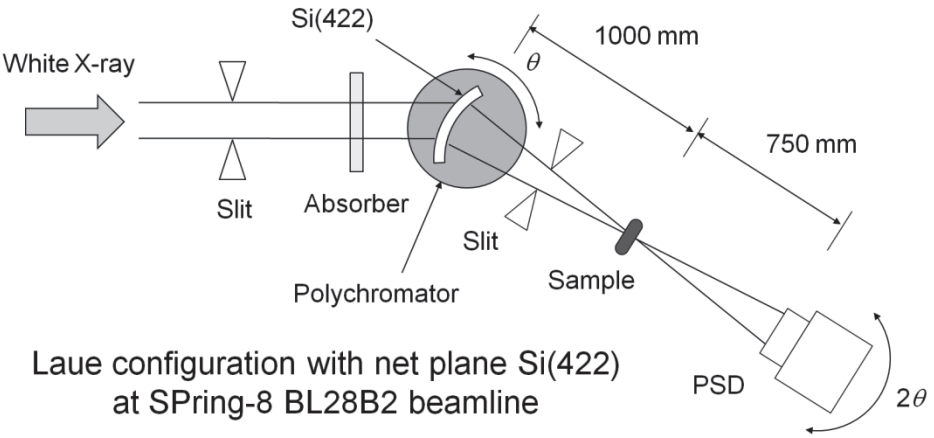

Scheme 2. Timetable of the DXAFS analysis in this study.

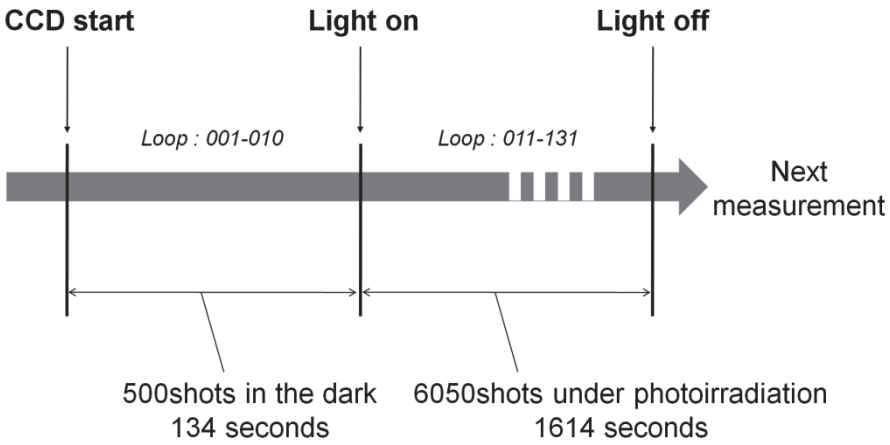

Results and Discussion

Static characterization. In order to understand the adsorption state of Rh ions on TiO_2 before photoirradiation, we measured the Rh-K edge EXAFS spectrum of the powders filtered from the suspension consisting of $RhCl_3$ solution (Rh: 0.076 mmol) and TiO_2 (500 mg) as well as those of the suspensions themselves. The Rh/TiO_2 prepared by photodeposition was studied by XRD, UV-vis. DR, and XAFS spectroscopies for the filtrated powders and suspensions.

Figure 1 shows the FT of k^3-weighted Rh-K edge EXAFS spectra of (a) Rh species adsorbed on TiO_2 after filtration together with those of (b) Rh_2O_3 and (c) $RhCl_3$ reference samples. Rh species adsorbed on TiO_2 exhibits the peak at 1.57 Å in Figure 1(a). The peak due to Rh-O scatterings is found at 1.57 Å in Figure 1(b) and the peak mainly due to Rh-Cl scatterings at 1.92 Å in Figure 1(c). By comparison of these peaks, the peak of Rh species adsorbed on TiO_2 before photoirradiation is assignable to the Rh-O scatterings. Rh ions are, therefore, adsorbed on TiO_2 without Cl^- ions. Figure 2 represents the FT of EXAFS spectra of the suspensions consisting of $RhCl_3$ and various amounts of TiO_2. The peaks were observed at 1.73 Å, although that of the adsorbed Rh ions on TiO_2 was found at 1.57 Å as shown in Figure 1(a). Since the spectra show average information of Rh cations in the suspension, the state of dissolved Rh ions are different from that of adsorbed ones. The peak height at 1.73 Å linearly decreased with an increase in the amount of TiO_2 as clearly shown in the inset of Figure 2. Alternatively, the band at lower than the peak position became broader noticeable with increasing the amount of TiO_2. The broadness shows the increase of contribution from Rh-O scatterings. We concluded that the peak at 1.73 Å is due to the contribution from both the Rh-O scatterings of Rh ions adsorbed on TiO_2 (1.57 Å) and Rh-Cl scatterings of $RhCl_3$ (1.92 Å). Figure 3 shows the FT of k^3-weighted Rh-K edge EXAFS spectra of (a) Rh/TiO_2 after completion of photodeposition and filtration, and (b) Rh foil. The peaks found at 2.42 Å are due to Rh-Rh scatterings. The peak in the spectrum of the Rh/TiO_2 at 2.42 Å is smaller than that of Rh foil, which would indicate the formation of small Rh metal particles on TiO_2.

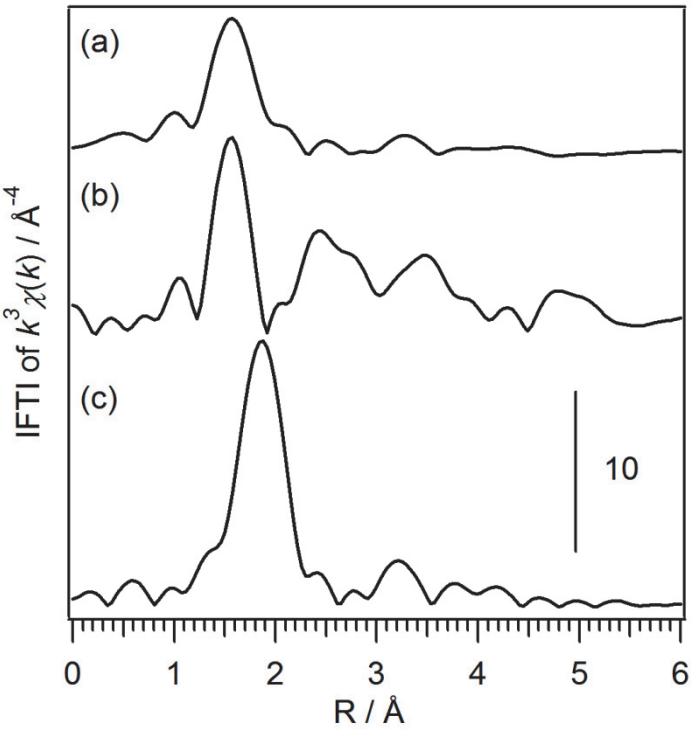

Figure 1. FT of k^3-weighted Rh-K edge EXAFS spectra of (a) Rh species adsorbed on TiO_2 before photoirradiation, (b) Rh_2O_3, and (c) $RhCl_3$.

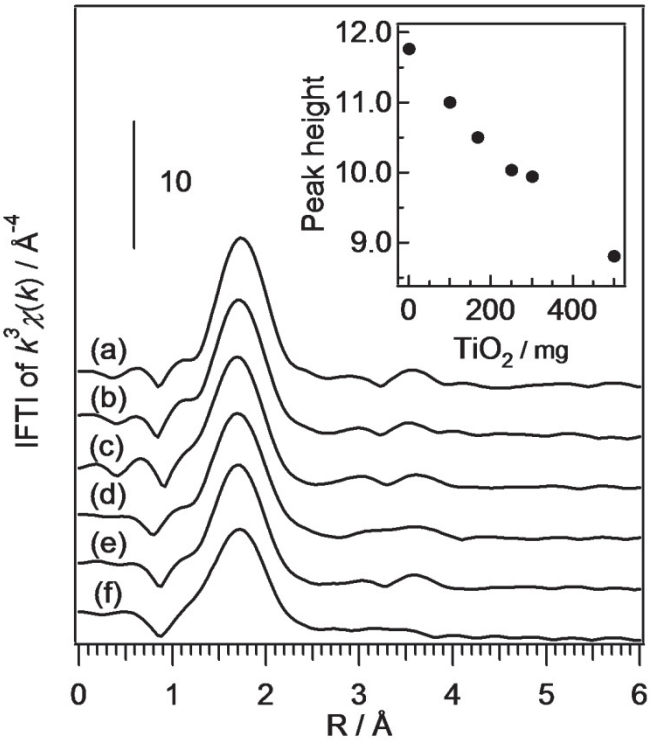

Figure 2. FT of EXAFS spectra of the suspensions consisting of $RhCl_3$ and various amounts of TiO_2: (a) 0, (b) 100, (c) 167, (d) 250, (e) 300, and (f) 500 mg. The inset is plot of the peak height of the peak at 1.73 Å against the amount of TiO_2.

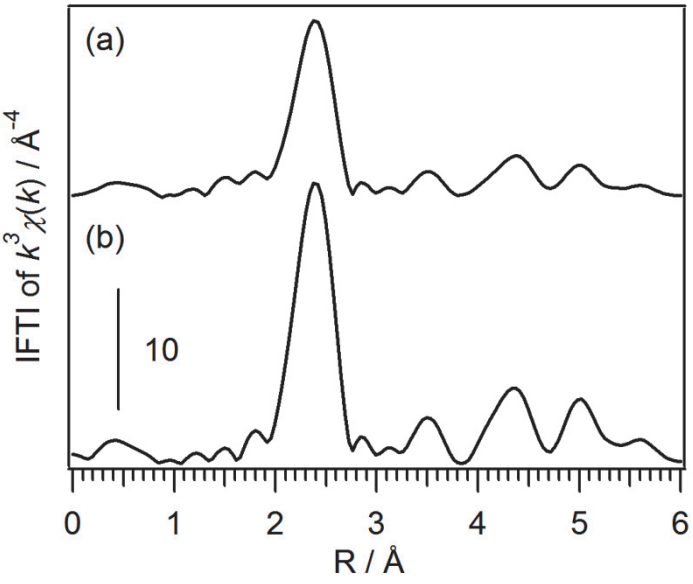

Figure 3. FT of k^3-weighted Rh-K edge EXAFS spectra of (a) Rh/TiO_2 after completion of photodeposition and (b) Rh foil.

XRD patterns of JRC-TIO-8 and Rh/TiO_2 prepared by the photodeposition method are shown in Figure 4. The anatase phase of TiO_2 was observed for all samples. The peaks around 40 degree marked with arrows in Figures 4(b) and (c) are due to the diffraction of Rh(111) plane, indicating the formation of Rh metal by photodeposition. The UV-vis. spectra of TiO_2 and Rh/TiO_2 were shown in Figure 5. The UV-vis. spectra of Rh/TiO_2 exhibit the broad band between 400 and 800 nm, which was attributed to the presence of Rh metal particle on TiO_2.[13] The band intensity increased with the photoirradiation time, corresponding to an increase in the amount of Rh on TiO_2 with photoirradiation time.

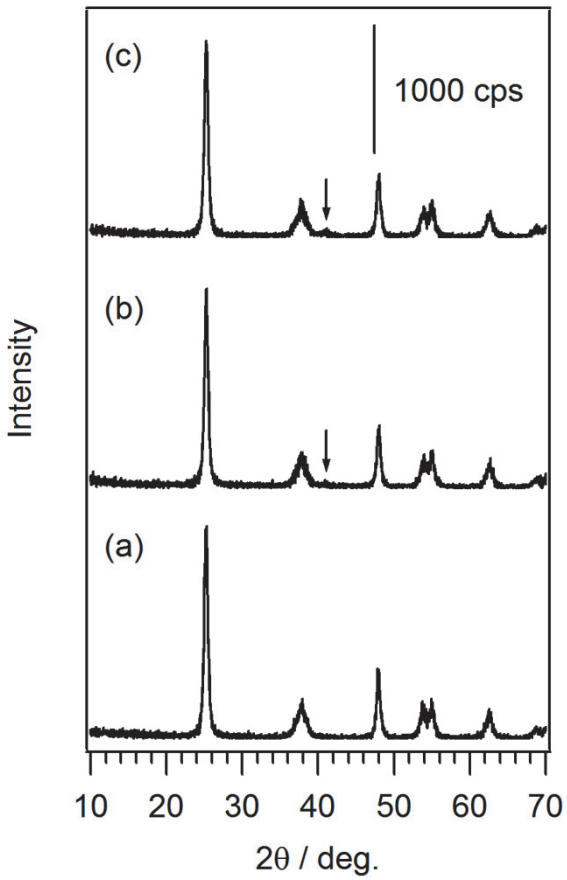

Figure 4. XRD patterns of (a) TiO_2 (JRC-TIO-8) and Rh/TiO_2 prepared by the photodeposition method using (b) 0.076 mmol and (c) 0.19 mmol of $RhCl_3$.

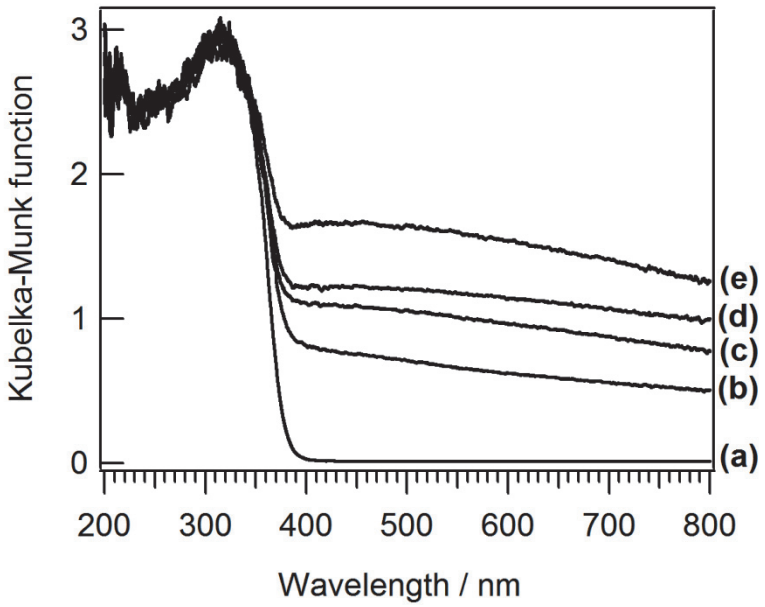

Figure 5. UV-vis. spectra of (a) TiO_2 (JRC-TIO-8) and a series of Rh species on TiO_2 prepared by the photodepositon for (b) 27, (c) 54, (d) 81, and (e) 108 min.

The FT of k^3-weighted Rh-K edge EXAFS spectra of the suspension of Rh/TiO_2 prepared by the photodeposition method was analyzed. The coordination number (Rh-Rh pair) was ca. 10, although that of Rh foil is 12, suggesting generation of fine Rh metal particles on TiO_2 by the photodeposition as mentioned before. The diamenter is estimated to be ca. 3 nm, assuming that the structure of the Rh metal particles is a cuboctahedron.[14,15] Table 1 listed the curve fitting results of Rh-Rh scattering of Rh metal particles prepared by the photodeposition of the suspensions involving various amount of $RhCl_3$ without change in the amount of TiO_2, water, and methanol. The coordination number was found to be independent on the amount of Rh photodeposited on TiO_2. On the other hand, Rh/TiO_2 was observed by TEM and EDX. Interestingly, Rh metal particles were not observed clearly with only TEM, although Rh domains with a few dozen nanometers were observed by EDX. We expected that Rh metal particle prepared by the photodeposition process has low crystallinity. The Rh domain may consist of Rh metal particles with 3-nm diameter. We are now investigating the structure of Rh metal particles and the reason why the Rh metal particles

have such structure.

Table 1. Curve fitting results of Rh-Rh scattering of Rh metal particles prepared by the photodeposition of the suspensions involving various amount of $RhCl_3$ without change in the amount of TiO_2, water, and methanol.

Amount of $RhCl_3$	C. N.[(a)]	r / Å[(b)]	σ / Å[(c)]	R[(d)]
0.076 mmol	9.0	2.69	0.067	0.08
0.152 mmol	9.7	2.69	0.067	0.14
0.228 mmol	9.2	2.69	0.064	0.10

R fitting range is 1.96-2.72 Å, and k fitting range is 2.80-15.7 $Å^{-1}$. (a) C. N., coordination number. (b) r: interatomic distance. (c) σ, Debye-Waller factor. (d) So-called R factor.

***In situ* DXAFS analysis.** We observed the photodeposition process of Rh metal particles on TiO_2 by *in situ* DXAFS spectroscopy. The reduction of Rh ions and the formation of Rh metal particles were evaluated by the analyses of XANES and EXAFS spectra, respectively. The residual Rh ions in the filtrate at the given irradiation time were evaluated with ICP analysis. We also investigated the photodeposition behaviors with various introduction amounts of $RhCl_3$ and various kinds of alcohol as sacrificial reagents.

Figure 6 shows a series of XANES spectra at Rh-K edge of the suspension consisting of $RhCl_3$ methanol-aqueous solution and TiO_2 under photoirradiation for 108 min. The XANES spectrum before photoirradiation is well consistent with those of $RhCl_3$ solution, and different from that of Rh_2O_3 shown in Figure 7. The edge energies (E_0) of XANES shifted to lower photon energy with elongation of photoirradiation time, indicating reduction of Rh^{3+} ions by photoirradiation. The XANES spectrum after 108 min of photoirradiation was almost identical with that of Rh foil presented in Figure 7, which suggests that Rh ions were

reduced to Rh^0 metal after 108 min. The XANES spectra gradually changed from that of Rh^{3+} ion to that of Rh^0 metal with the isosbestic points. This result indicates that the Rh^{3+} ions are reduced into Rh^0 in the photodeposition process without any intermediates on the second time scale. It should be also noted that such spectral change was not observed without TiO_2 or photoirradiation. All Rh-K edge XANES spectra can be reproduced with the linear combination of the two XANES spectra; one is that of Rh ion in the initial state and the other is that of Rh metal in the final state. We obtained the fractions of Rh^0 metal and Rh^{3+} precursor by least-squares fitting of each XANES spectrum with linear combination of authentic XANES spectra of Rh^0 and Rh^{3+}.

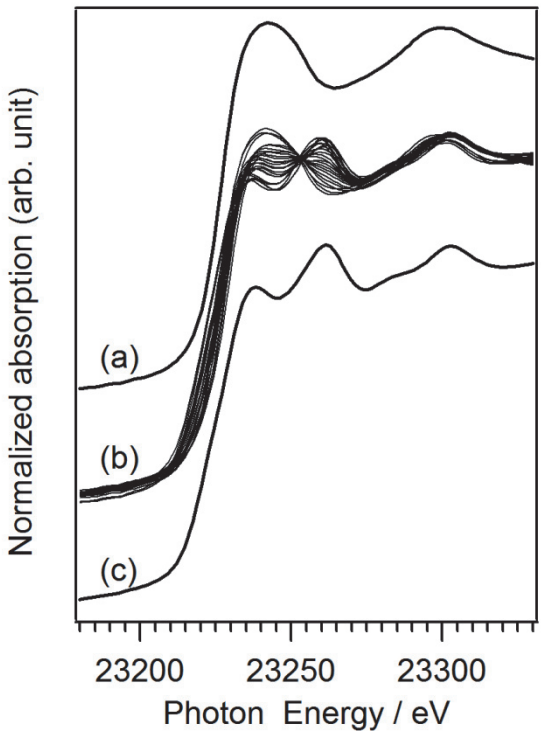

Figure 6. XANES spectra at Rh-K edge of the suspension consisting of $RhCl_3$ methanol-aqueous solution and TiO_2 (a) before photoirradiation, (b) under photoirradiation, and (c) after photoirradiation for 108 min.

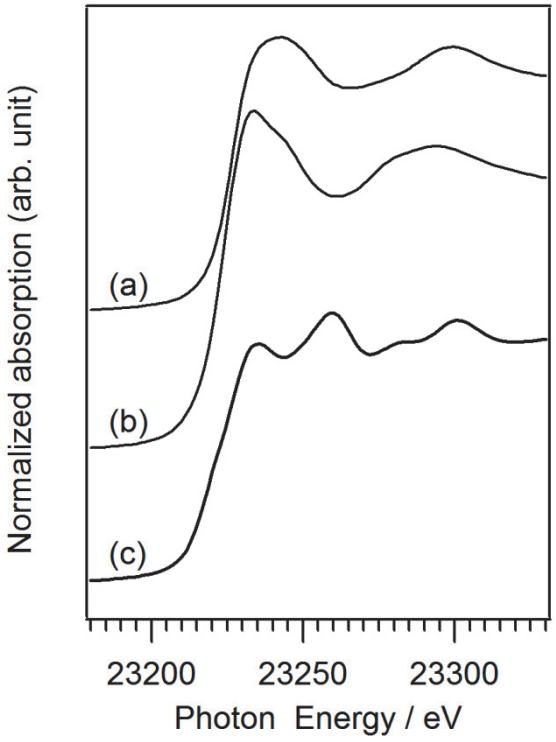

Figure 7. XANES spectra at Rh-K edge of (a) $RhCl_3$ solution, (b) Rh_2O_3, and (c) Rh foil.

Figures 8(a) and (b) shows the dependence of the fraction of Rh metal and Rh^{3+} precursor on photoirradiation time respectively. The fraction of Rh metal linearly increased with photoirradiation time and saturated after 90 min photoirradiation. On the other hand, the fraction of Rh^{3+} ions linearly decreased and reached 0% after 90 min. These indicate that the Rh^{3+} ions are reduced to Rh metal at a constant rate and consumed completely after 90 min. The residual amount of Rh^{3+} ion in the filtrate evaluated with ICP also decreased and is not detected after 90 min photoirradiation as shown in Figure 8(c), although it did not decreased linearly. This implies the adsorption of Rh^{3+} ion on TiO_2. The adsorption amount is given by,

$Rh^{3+}_{ads.} = Rh^{3+}_{tot.} - Rh^{3+}_{res.}$

where $Rh^{3+}_{ads.}$ is the adsorbed amount and $Rh^{3+}_{res.}$ is residual amount evaluated by ICP. $Rh^{3+}_{tot.}$ is given by the fraction of Rh ion evaluated by XANES analysis shown in Figure 8 (b).

$Rh^{3+}_{tot.} = (1 - t / 90)\ Rh_{tot.}$

where t is the photoirradiation time / min and $Rh_{tot.}$ is the total amount of Rh species (0.076

mmol). Figure 9 shows the plot of 1 / $Rh^{3+}{}_{ads.}$ against 1 / $Rh^{3+}{}_{res.}$. (The amount of TiO_2 and the volume of solution are constant in this case.) The linear plot suggests a Langmuir type adsorption of Rh^{3+} ion. This result suggests that the adsorption of Rh^{3+} ion is not the rate determining step of photodeposition, because Rh^{3+} ions are reduced propotionally to photoirradiation time as shown in Figure 8(b). Therefore, Rh metal is generated by the reduction of Rh^{3+} ion at constant rate regardless of the adsorption of Rh^{3+} ion.

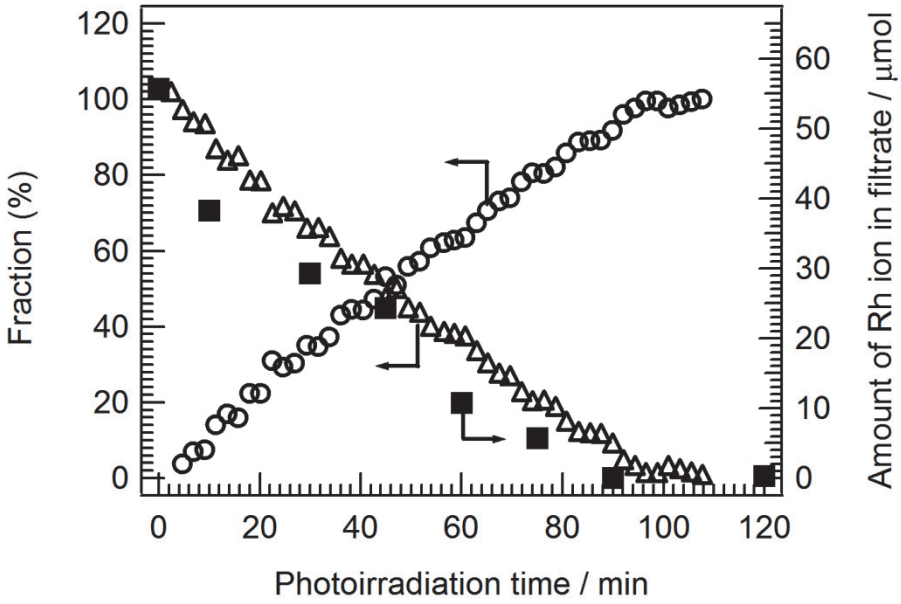

Figure 8. Dependence of the fractions of (a) Rh metal (circle) and (b) Rh ion (triangle) on photoirradiation time evaluated by the pattern fitting of respective XANES spectra with those before photoirradiation and after photoirradiation for 108 min, together with (c) the residual amount of Rh ion in the filtrate evaluated with ICP (square).

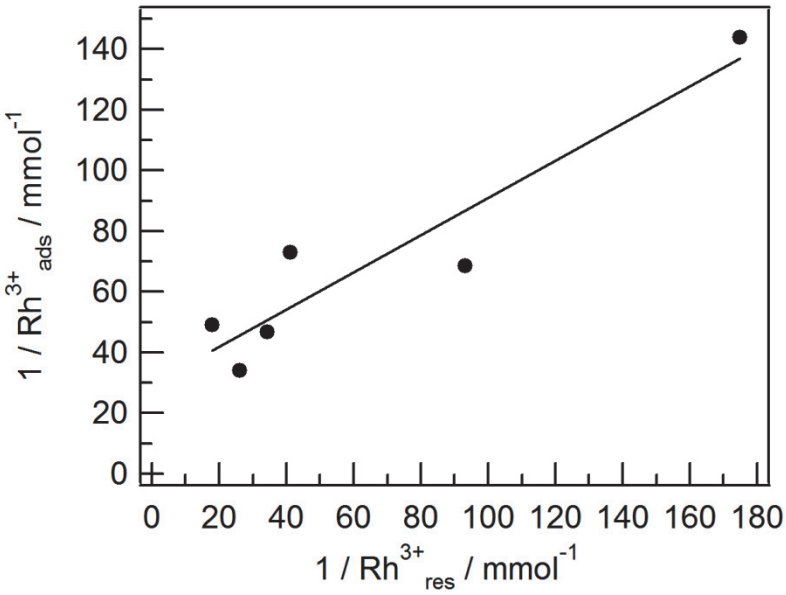

Figure 9. Dependence of the amount of adsorbed Rh^{3+} ion ($Rh^{3+}_{ads.}$) on the amount of residual Rh^{3+} ion in the solution ($Rh^{3+}_{res.}$) at various photoirradiation time. $1 / Rh^{3+}_{ads.}$ is plotted against $1 / Rh^{3+}_{res.}$.

We also obtained a series of k^3-weighted Rh-K edge EXAFS spectra of Rh species for the photodeposition as shown in Figure 10. The amplitude of the oscillation in the high k range grew with photoirradiation time, meaning that a Rh atom is not bonded with a light atom but a heavy atom, i.e., Rh. The oscillations in the k range 2.64-10.5 $Å^{-1}$ exhibit appropriate quality to perform Fourier transformation of Rh-K edge EXAFS spectra. Figure 11 shows a series of the FT of k^3-weighted Rh-K edge EXAFS spectra of Rh species for the photodeposition. The peak located at 1.73 Å is assignable to the mixture of Rh-Cl scattering of $RhCl_3$ and Rh-O scattering of Rh ions adsorbed on TiO_2 as described above. The height of the peak at 1.73 Å decreased with increasing photoirradiation time and an alternative peak appeared at 2.45 Å. The peak at 2.45 Å is evidently assigned to Rh-Rh scattering of Rh metal particles generated by photoirradiation, in comparison with the FT of EXAFS spectrum of Rh foil as a reference. The peak height at 2.45 Å linearly rose with photoirradiation time and

saturated after 90 min photoirradiation when the XANES spectrum of Rh species just corresponded to that of Rh foil as shown in Figures 6-8. The structural parameters (coordination number, interatomic distance, and Debye-Waller factor) of the Rh metal particles were obtained by a curve fitting analysis. The structural parameters at the selected photoirradiation time (26.9, 53.8, 80.7, and 107.6 min) are listed in Table 2.

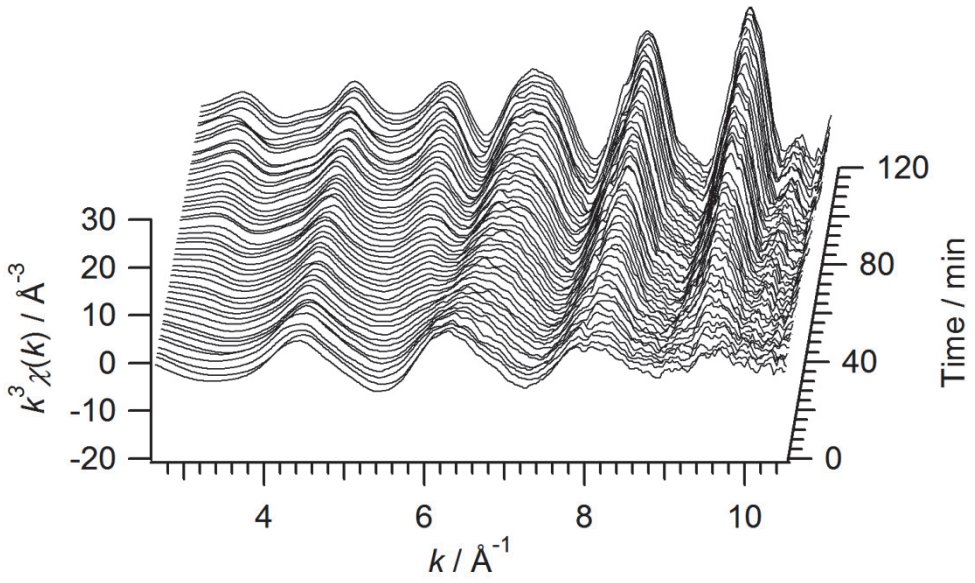

Figure 10. Series of of k^3-weighted Rh-K edge EXAFS spectra of Rh species for the photodeposition.

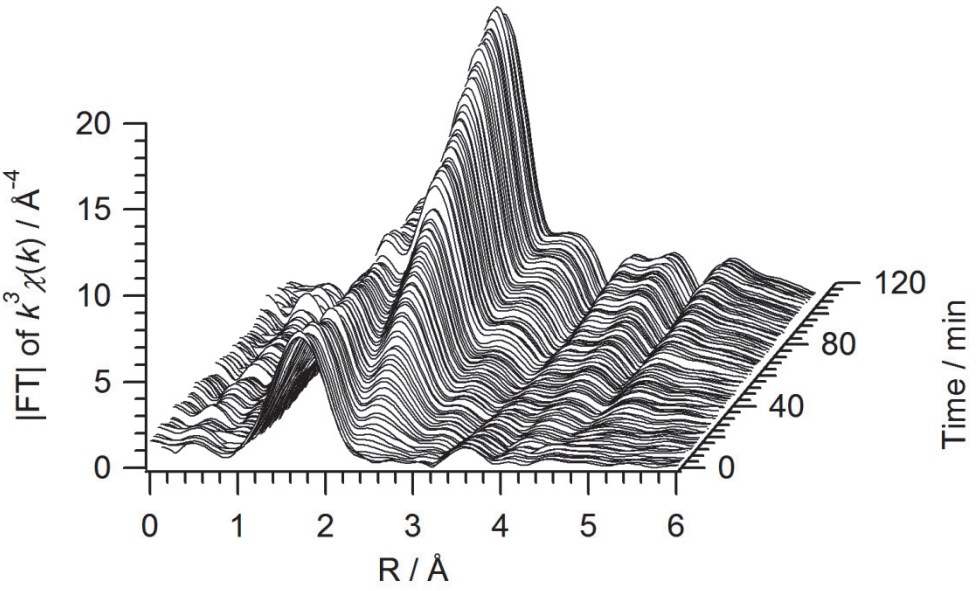

Figure 11. Series of the FT of k^3-weighted Rh-K edge EXAFS spectra of Rh species for the photodeposition.

Table 2. Curve fitting results of Rh-Rh scattering of FT of EXAFS spectra at selected photoirradiation time.

Photoirradiation time / min	C. N.[(a)]	r / Å[(b)]	σ / Å[(c)]	R[(d)]
26.9 min	3.1	2.72	0.060	0.46
53.8 min	5.9	2.72	0.066	0.37
80.7 min	8.6	2.72	0.068	0.63
107.6 min	10.1	2.73	0.070	0.95

R fitting range is 2.07-2.92 Å, and k fitting range is 2.64-10.5 Å^{-1}. (a) C. N., coordination number. (b) r, interatomic distance. (c) σ, Debye-Waller factor. (d) So-called R factor.

Figure 12(a) demonstrates the photoirradiation time dependence of the coordination number (Rh-Rh pair) evaluated by the curve fitting of Rh-Rh scattering. The coordination number increased proportionally to photoirradiation time. And it was evaluated to be 10 at 90 min of photoirradiation. The behavior in Figure 12(a) is perfectly consistent with that in Figure 8(a). This result strongly supports that the electrons generated by a charge separation reduce the Rh^{3+} ions to form Rh metal particles at a constant rate. At present we suppose that the Rh metal particles do not grow up in incremental steps but the Rh metal particles with a uniform size appear one after another on the surface because the coordination number (Rh-Rh pair) increases in a linear fashion and the Debye-Waller factor does not undergo appreciable changes as shown in Figure 13. Combined with the XANES analysis, the number of Rh metal particles with a uniform size constantly increases with the reduction of Rh ions at constant rate.

The formation rate of Rh metal particles depended on the initial amount of Rh ions and the kind of alcohols as sacrificial reagent. Figure 12 shows the photoirradiation time dependence of the coordination number (Rh-Rh pair) with the different initial amount of $RhCl_3$: (a) 0.076 mmol and (b) 0.038 mmol. The increasing rate of the coordination number in the case of 0.038 mmol of $RhCl_3$ is three-fold higher than that of the typical amount of $RhCl_3$ (0.076 mmol), although the coordination number (Rh-Rh pair) in Rh metal particles after photodeposition is almost the same value, ca. 10. The reduction rate of Rh ions to Rh metal in the photodepostion varied with the kind of alcohols as sacrificial reagents; methanol > ethanol >> 1-propanol > 2-propanol. The reduction rate does not have relations with ionization potential of alcohols but with the p*K*a value of alcohols.[16] Table 3 shows the curve fitting results of the Rh metal particles prepared by the photodeposition in the presence of various sacrificial reagents. The coordination number (Rh-Rh pair) was constant at ca. 10 in spite of variation of the kinds of alcohols. The reduction rate from Rh^{3+} ions to Rh metal on TiO_2 has no effect on the size of the generated Rh metal particles.

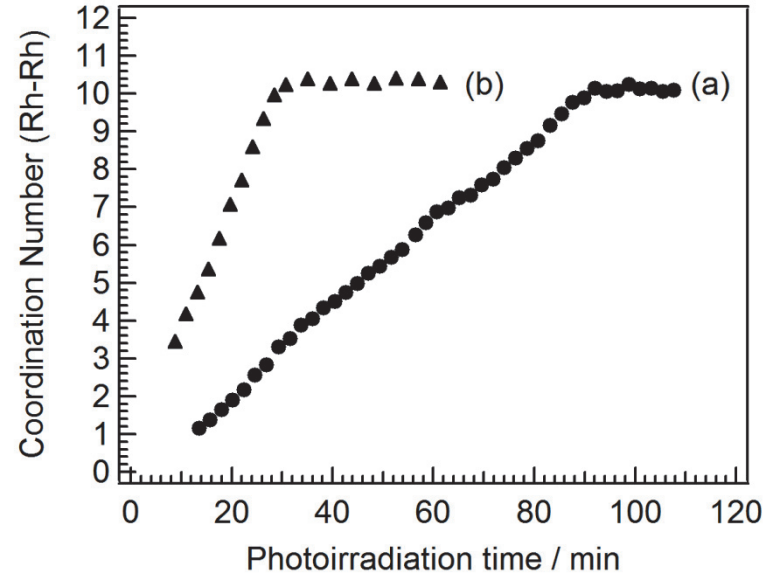

Figure 12. Photoirradiation time dependence of the coordination number (Rh-Rh pair) with the different initial amount of $RhCl_3$: (a) 0.076 mmol and (b) 0.038 mmol.

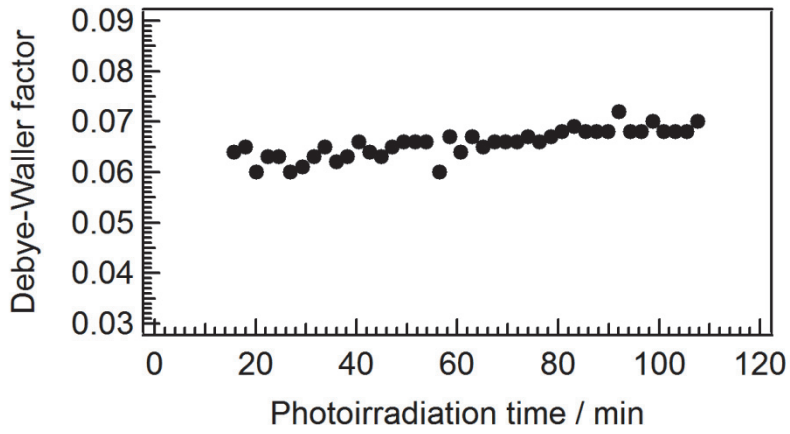

Figure 13. Photoirradiation time dependence of the Debye-Waller factor of the generated Rh metal particles.

Table 3. Curve fitting results of the Rh metal particles prepared by the photodeposition in the presence of various sacrificial reagents.

Sacrificial Reagent	C. N.[(a)]	r / Å[(b)]	σ / Å[(c)]	R[(d)] (%)
Methanol	9.0	2.69	0.064	0.11
Ethanol	9.0	2.69	0.067	0.13
1-Propanol	9.3	2.69	0.068	0.11
2-Propanol	9.6	2.69	0.067	0.13

R fitting range is 2.07-2.92 Å, and k fitting range is 2.64-10.5 $Å^{-1}$. (a) C. N., coordination number. (b) r, interatomic distance. (c) σ, Debye-Waller factor. (d) So-called R factor.

Formation mechanism. The static characterization and *in situ* DXAFS analysis of the photodeposition of Rh metal particles on TiO_2 suggest the mechanism as follows; the Langmuir type adsorption of Rh^{3+} ions on TiO_2 to form Rh-O bonds, the reduction of Rh^{3+} ions to Rh^0 metals on the surface of irradiated TiO_2 photocatalyst by electron together with the oxidation of alcohols by holes, and the constant appearance of Rh metal particles. And the average coordination number (Rh-Rh pair) is ca. 10. The coordination number did not depend on the reduction rate nor the introduction amount of Rh. This result is compatible to the linear increase in the coordination number in the photodeposition process, suggesting the constant appearance of Rh metal nanoparticles with a uniform size on TiO_2.

Conclusion

The photodeposition process of Rh metal particles on TiO_2, which was performed in the presence of $RhCl_3$ as a precursor and methanol as a sacrificial reagent, was observed by *in situ* time-resolved DXAFS measurement, static XAFS measurement, and ICP analysis. These analyses revealed that the photodeposition process of Rh species on TiO_2 contains the Langmuir type adsorption of Rh^{3+} ions on TiO_2, the reduction of Rh^{3+} ions to Rh metals by electrons generated by UV light irradiation to TiO_2 together with the oxidation of alcohols by holes, and the constant appearance of Rh metal particles of a fixed size.

References

(1) (a) Couves, J. W.; Thomas, J. M.; Waller, D.; Jones, R. H.; Dent, A. J.; Derbyshire, G. E.; Greaves, G. N. *Nature* **1991**, *354*, 465. (b) Fiddy, S. G.; Newton, M. A.; Dent, A. J.; Salvini, G.; Corker, J. M.; Turin, S.; Campbell, T.; Evans, J. *Chem. Commun.* **1999**, 851. (c) Yamaguchi, A.; Shido, T.; Inada, Y.; Kogure, T.; Asakura, K.; Nomura, M.; Iwasawa, Y. *Bull. Chem. Soc. Jpn.* **2001**, *74*, 801. (d) Yamaguchi, A.; Suzuki, A.; Shido, T.; Inada, Y.; Asakura, K.; Nomura, M.; Iwasawa, Y. *J. Phys. Chem. B* **2002**, *106*, 2415. (e) Suzuki, A.; Inada, Y.; Yamaguchi, A.; Chihara, T.; Yuasa, M.; Nomura, M.; Iwasawa, Y. *Angew. Chem. Inte. Ed.* **2003**, *42*, 4795. (f) Yamamoto, T.; Suzuki, A.; Nagai, Y.; Tanabe, T.; Dong, F.; Inada, Y.; Nomura, M.; Tada, M.; Iwasawa, Y. *Angew. Chem. Int. Ed.* **2007**, *46*, 9253.

(2) (a) Shishido, T.; Asakura, H.; Aamano, F.; Sone, T.; Yamazoe, S.; Kato, K.; Teramura, K.; Tanaka, T. *Catal. Lett.* **2009**, *131*, 413. (b) Harada, M.; Inada, Y. *Langmuir* **2009**, *25*, 6049. (c) Okumura, K.; Kusakabe, T.; Yokota, S.; Kato, K.; Tanida, H.; Uruga, T.; Niwa, M. *Chem. Lett.* **2003**, *32*, 636. (d) Okumura, K.; Nota, K.; Yoshida, K.; Niwa, M. *J. Catal.* **2005**, *231*, 245.

(3) (a) Kaminaga, U.; Matsushita, T.; Kohra, K. *Jpn. J. Appl. Phys.* **1981**, *20*, L355. (b) Matsushita, T.; Phizackerley, R. P. *Jpn. J. Appl. Phys.* **1981**, *20*, 2223.

(4) Teramura, K.; Okuoka, S.-i.; Yamazoe, S.; Kato, K.; Shishido, T.; Tanaka, T. *J. Phys. Chem. C* **2008**, *112*, 8495.

(5) (a) Tanaka, K.; Harada, K.; Murata, S. *Solar Energy* **1986**, *36*, 159. (b) Herrmann, J. M. D. *Catal. Today* **1999**, *53*, 115.

(6) Wang, X. C.; Yu, J. C.; Yip, H. Y.; Wu, L.; Wong, P. K.; Lai, S. Y. *Chem.-Eur. J.* **2005**, *11*, 2997.

(7) Bamwenda, G. R.; Tsubota, S.; Nakamura, T.; Haruta, M. *Catal. Lett.* **1997**, *44*, 83.

(8) Kraeutler, B.; Bard, A. J. *J. Am. Chem. Soc.* **1978**, *100*, 4317.

(9) (a) Yoneyama, H.; Nishimura, N.; Tamura, H. *J. Phys. Chem.* **2002**, *85*, 268. (b) Sato, S. *J. Catal.* **1985**, *92*, 11.

(10) Kowalska, E.; Abe, R.; Ohtani, B. *Chem. Commun.* **2009**, 241.

(11) Herrmann, J. M. D., J.; Pichat, P. *J. Phys. Chem.* **2002**, *90*, 6028, and references therein.

(12) (a) Caballero, A.; Gonzalezelipe, A. R.; Fernandez, A.; Herrmann, J. M. D.; Dexpert, H.; Villain, F. *J. Photochem. Photobiol. A: Chem.* **1994**, *78*, 169. (b) Fernandez, A.; Caballero, A.; Gonzalez-Elipe, A. R.; Herrmann, J. M. D.; Dexpert, H.; Villain, F. *J. Phys. Chem.* **1995**, *99*, 3303.

(13) Zettsu, N.; McLellan, J. M.; Wiley, B.; Yin, Y. D.; Li, Z. Y.; Xia, Y. N. *Angew. Chem. Int. Ed.* **2006**, *45*, 1288.

(14) Greegor, R. B.; Lytle, F. W. *J. Catal.* **1980**, *63*, 476.

(15) Jentys, A. *Phys. Chem. Chem. Phys.* **1999**, *1*, 4059.

(16) Tamaki, Y.; Furube, A.; Murai, M.; Hara, K.; Katoh, R.; Tachiya, M. *J. Am. Chem. Soc.* **2005**, *128*, 416.

Chapter 7

Modification of Metal Nanoparticles with TiO_2 and Metal-Support Interaction in Photodeposition

Abstract

Rh, Pt, and Au metals photodeposited on TiO_2 with an anatase phase (M-TiO_2(p), M: Rh, Pt, Au) were studied using transmission electron microscopy (TEM), scanning transmission electron microscopy (STEM), energy dispersive X-ray (EDX) analysis, X-ray absorption fine structure (XAFS) spectroscopy, X-ray photoelectron spectroscopy (XPS), and XPS depth profile analysis. The TEM images of Rh-TiO_2(p) and Pt-TiO_2(p) did not clearly show the grain boundary of metal particles, although the Rh and Pt species of Rh-TiO_2(p) and Pt-TiO_2(p) were observed by EDX analysis to show the metal particles having 10–20 nm. These results suggest that the photodeposited Rh and Pt metal particles have a disorganized structure, which is also supported by extended XAFS (EXAFS) spectral analysis. It is speculated that a strong metal-support interaction (SMSI) takes place in the case of Rh and Pt, resulting in the disorganized structure. In the case of Au, however, metal particles with a well-organized and spherical structure were observed, indicating that Au does not strongly interact with TiO_2. The XPS analyses revealed that the surface of metal particles of M-TiO_2(p) received electrons from TiO_2. The XPS depth profile analysis suggests that the metal particles are modified by their interaction with TiO_2. $TiO_{2-\delta}$ generated by the photoirradiation of TiO_2 can cause the modification and the disorganized structure of Rh and Pt metal particles.

Introduction

Photodeposition has been used to recover noble metals, to remove metal cations from aqueous effluents, and to prepare metal-supported catalysts and photocatalysts ever since Bard et al. reported in 1978.[1-6] The irradiation of a semiconductor powder (e.g., TiO_2) with UV light results in the reduction of metal cations having appropriate redox potential by the photoexcited electrons, generating metal particles on TiO_2. Very recently, we reported the photodepostion process of Rh metal particles on TiO_2 using *in situ* time-resolved energy dispersive XAFS (DXAFS) spectroscopy.[7,8] The spectral analysis revealed that the $RhCl_3$ precursor was proportionally reduced to Rh metal particles as the photoirradiation time increased. The coordination number (CN) of the Rh−Rh pair also proportionally increased with the photoirradiation time and stopped at a CN of ca. 10, although that of Rh foil is 12. These results indicate that the fine Rh metal particles with a uniform CN of Rh−Rh pair (ca. 10) consistently appear. Interestingly, Rh metal particles were not identified by TEM observation, although Rh domains of a few dozen nanometers were observed by EDX analysis (Figure 1). We expected that Rh metal particles prepared by the photodeposition process would have a disorganized structure. The structure can be induced by the metal-support interaction, which can inhibit the formation of Rh−Rh bonds.[9]

The interaction between the support and the metal in a supported-metal catalyst plays an important role in the catalytic reaction.[10,11] The treatment of group VIII noble metals (e.g., Pt, Rh, Pd, and Ir) on reducible oxide supports (e.g., TiO_2 and Nb_2O_5) with H_2 at high temperature suppresses the H_2 and CO chemisorptions of the metal particles, and this phenomenon was termed strong metal-support interaction (SMSI). The SMSI changes the catalytic activity and selectivity of the metal particles, because the SMSI influences on the electronic property and the morphology of metal particles, and causes the modification of metal particles with the reduced supports (e.g., $TiO_{2-\delta}$) generated by H_2 treatment at high temperature.[11-15]

It is well known that photoirradiation to TiO_2 generates $TiO_{2-\delta}$, which can serve as the formation site for metal particles.[16,17] As mentioned above, $TiO_{2-\delta}$ strongly interacts with metal species to change the electronic properties and morphology of those metal particles.

The electronic properties of the metal particles change the Schottky barrier height between the metal and the support, affecting the efficiency of charge separation,[3] while the variation in the morphology of metal particles influences the way in which the substrates adsorb the metals. The efficiency of charge separation and the manner of adsorption in turn affect the photocatalytic activity. Therefore, the interaction between metal and support is an important factor for metal-modifying photocatalysts. However, there are few studies dealing with the interaction.[3,6,18]

To study the metal-supported interaction that occurs in photodeposition, we used TEM, EDX, XAFS, XPS, and depth analysis to investigate the structure and electronic properties of Rh and Pt, group VIII metals, and Au, a group IB metal, photodeposited on a TiO_2.

Experimental

Preparation. Photodeposition of Rh, Pt, and Au particles on TiO_2 was carried out in a closed batch system. As a typical photodeposition method, 500 mg of TiO_2 (JRC-TIO-8, anatase phase) calcined at 673 K in air was suspended in 3.2 mL of methanol in a batch reactor made of Pylex® glass with a flat ceiling window for illumination, followed by addition of 0.8 mL of aqueous solution of metal precursor (0.076 mmol). $RhCl_3 \cdot H_2O$, $H_2PtCl_6 \cdot 6H_2O$, and $HAuCl_4 \cdot 4H_2O$ (Wako Pure Chemical Industries, Ltd.) were used as metal precursors. The suspension was irradiated for 120 min with a 200-W Hg−Xe lamp equipped with fiber optics, a collective lens, and a mirror (San-Ei Electric Co., Ltd., UVF-204S type C) after Ar bubbling for 10 min. The suspension was then filtered and the residual powder was washed with 100 mL of purified water. The residue was placed in an oven at 353 K, resulting in a powder which is abbreviated to M-TiO_2(p) (M: Rh, Pt, and Au). As a reference, Rh and Pt were deposited on TiO_2 by an impregnation method. The suspension consisting of each metal precursor (0.76 mmol) in 150 mL of water and TiO_2 (5.00 g) was stirred at 353 K for 2 h, and then dried. The sample was then calcinated at 773 K for 3 h. The resulting powder was reduced under ca. 100 Torr of H_2 at 573 K and 773 K to prepare M-TiO_2(i573) and M-TiO_2(i773) (M: Rh and Pt), respectively. Au-TiO_2(dp) was also prepared by the

deposition–precipitation method as a reference.[19] A NaOH aqueous solution (1 M) was added dropwise to a 200 mL $HAuCl_4$ aqueous solution (0.21 mmol) to adjust the pH of the solution between 6 and 10. TiO_2 (2.03 g) was added to the solution and stirred at 343 K for 2 h, followed by filtration. The resulting residue was washed by 20-min stirring in water at 343 K and the solution was discarded by filtration. The washing process was repeated 3 times. The resulting powder was dried under 353 K, and then calcinated at 573 K to prepare Au-TiO_2(dp).

Analysis. TEM, STM, and EDX mapping images were obtained with a JEOL JEM-2100F transmission electron microscope operating at an accelerating voltage of 200 kV. TEM samples were prepared by depositing drops of a methanol suspension containing small amounts of the powders onto a carbon-coated copper grid (Okenshoji Co. Ltd.) and allowing the methanol to evaporate in air.

The XAFS measurement at the Rh K-edge was carried out using an NW10A beamline of the Photon Factory Advanced Ring (PF-AR, 6.5 GeV) at the High Energy Accelerator Research Organization (KEK; Tsukuba, Japan) with a Si(311) double crystal monochromator. Ion chambers of I and I_0 detector were filled with Ar (100%) flow and Kr (100%) flow, respectively. The X-ray energy was calibrated with a spectrum of Rh foil. The XAFS measurement at the Au and Pt L_3-edge was performed using a BL7C beamline of a Photon Factory storage ring (PF, 2.5GeV). Ion chambers of I and I_0 detector were filled with N_2 (85%)/Ar (15%) and Ar (100%) flow, respectively. The X-ray energy was calibrated with a spectrum of Cu foil at 8980 eV. The XAFS spectra of all of the samples were recorded in the transmission mode. Data reduction of XAFS spectra was performed using REX2000 program Ver. 2.5.9 (Regaku Corp.). The k^3 weighted Rh K-edge and Pt L_3-edge EXAFS oscillations were Fourier-transformed in the ranges of 3.2–17.0 and 3.1–16.9 $Å^{-1}$, respectively. The curve-fitting of Fourier-filtered EXAFS spectra was performed using empirical parameters extracted from the XAFS spectrum of the Rh and Pt foils.

XPS spectra were acquired using an ULVAC PHI 5500MT system. Samples mounted on indium foil were analyzed using Mg $K\alpha_{1,2}$ radiation (15 kV, 400 W) in a

chamber with the gas pressure less than 1×10^{-8} Torr. The electron take-off angle was set at 45°. Binding energies were referenced to C 1s peak of residual carbon at 284.6 eV. Sputtering was performed by Xe ion beam (3.0 kV) with raster size 1.1 mm × 2.1 mm.

Result and Discussion

Structural analysis. Figure 1 shows the TEM image and the overlay of the EDX mapping image on the STEM image of Rh-TiO_2(p). The particle boundaries of the Rh metal species are not identified in the TEM image, although the existence of an Rh metal species is identified as green dots that have a domain width of ca. 15 nm. As a reference, the TEM image of Rh-TiO_2 (i573) clearly showed Rh metal particles ca. 2 nm in diameter. Figure 2 shows the TEM image and the overlay of the EDX mapping image on the STEM image of Pt-TiO_2(p). The metal species of Pt-TiO_2(p) and Rh-TiO_2(p) are identified in the EDX mapping images but not in the TEM images. Rh and Pt particles which have a disordered structure on TiO_2 show ambiguous contrast, Moire fringes, and particle boundaries.

Figures 3 and 4 show the Rh K-edge and Pt L_3-edge with k^3 weighted EXAFS spectra of Rh-TiO_2(p) and Pt-TiO_2(p). These EXAFS spectra have the same phase as the respective foils and a smaller oscillation amplitude than the respective foils. The small amplitude is indicative of the small number of metal–metal pairs. Table 1 lists the structural parameters obtained by the curve fitting of the Fourier-transformed EXAFS spectra of Rh-TiO_2(p) and Pt-TiO_2(p). The CNs of the Rh and Pt metal particles are 9.0 and 10.1, respectively, although the foils have a CN of 12. This suggests the formation of metal particles of ca. 2−3 nm diameter, assuming the cuboctahedral structure. The agglomerates of these small metal particles would be observed in the EDS mapping images to show a metal domain ca. 15 nm. Our previous work indicated that such metal particles consistently appear with an increase in photoirradiation time.[7,8] It is likely that the small metal particles aggregate and form the large particles with ca. 15 nm, as observed by the EDS analysis.

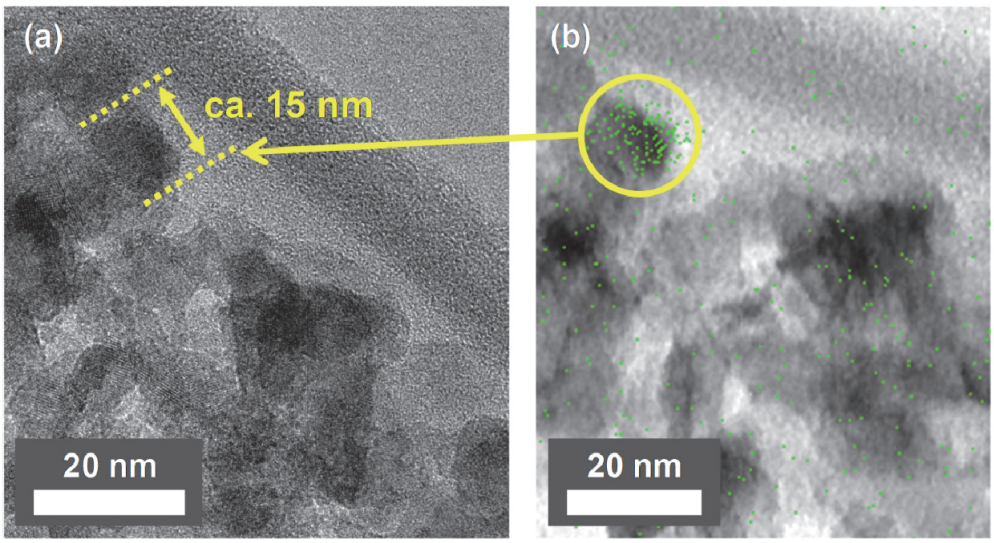

Figure 1. (a) TEM image and (b) overlay of EDS mapping image on STEM image of Rh-TiO_2(p).

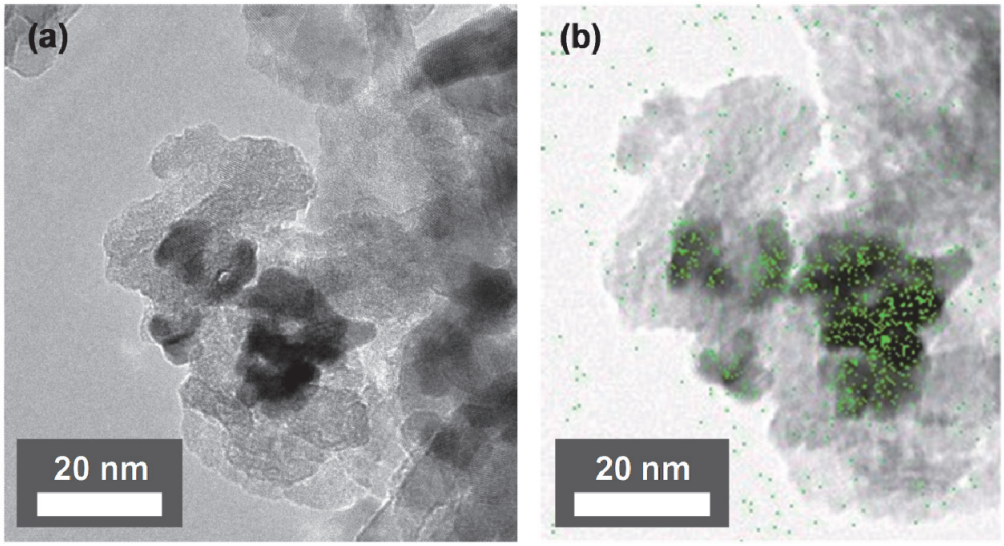

Figure 2. (a) TEM image and (b) overlay of EDS mapping image on STEM image of Pt-TiO_2(p).

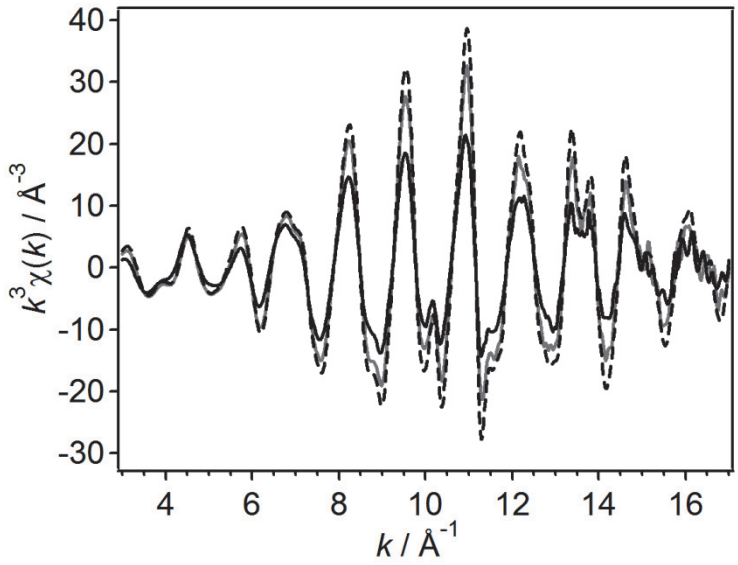

Figure 3. Rh K-edge k^3 weighted EXAFS spectra of Rh-TiO_2(p) (black solid line), those after heat treatment (gray solid line), and Rh foil (black dashed line).

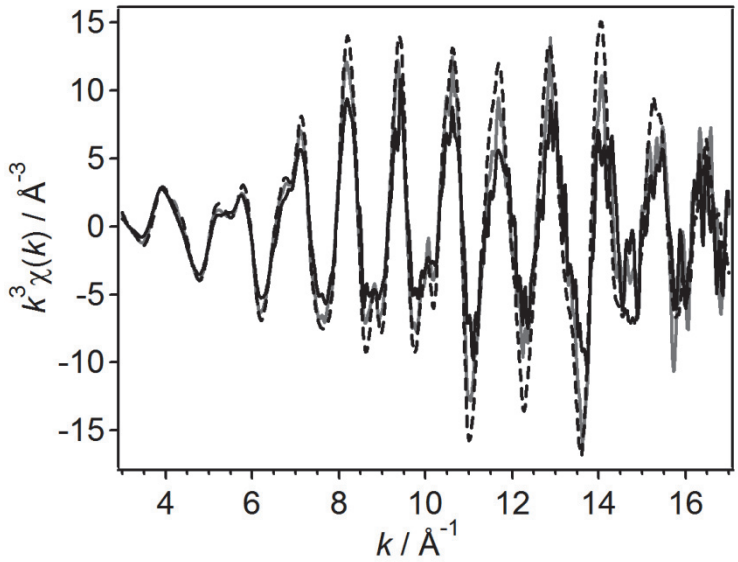

Figure 4. Pt L_3-edge k^3 weighted EXAFS spectra of Pt-TiO_2(p) (black solid line), those after heat treatment (gray solid line), and Pt foil (black dashed line).

Table 1. Curve fitting results of Rh-Rh scattering of Rh metal particles and Pt-Pt scattering of Pt metal particles prepared by the photodeposition.

	C. N.[(a)]	r / Å[(b)]	σ/ Å[(c)]	R (%)[(d)]
Rh	9.0	2.69	0.069	21.2
Pt	10.1	2.76	0.072	23.8

Rh: R fitting range is 2.00-2.76 Å, and k fitting range is 4.6-16.4 $Å^{-1}$. Pt: R fitting range is 2.30-3.03 Å, and k fitting range is 4.6-16.2 $Å^{-1}$. (a) C. N., coordination number. (b) r: interatomic distance. (c) σ, Debye-Waller factor. (d) So-called R factor.

Au-TiO_2(p) was also observed by TEM as shown in Figure 5. The Au metal particles show clear particle boundaries and a spherical structure. This means a well-organized structure for the Au metal particles. Figure 6 exhibits the Au L_3-edge k^3 weighted EXAFS spectra of Au-TiO_2(p). The EXAFS spectrum of Au-TiO_2(p) has almost the same amplitude as the Au foil, which supports the well-organized structure of Au metal particles indicated by the TEM analysis.

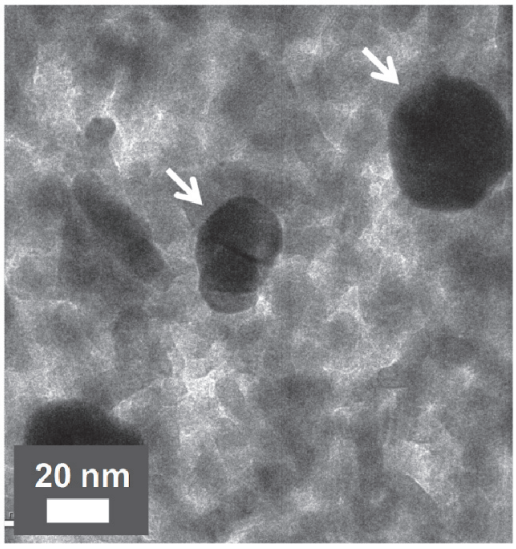

Figure 5. TEM image of Au-TiO_2(p).

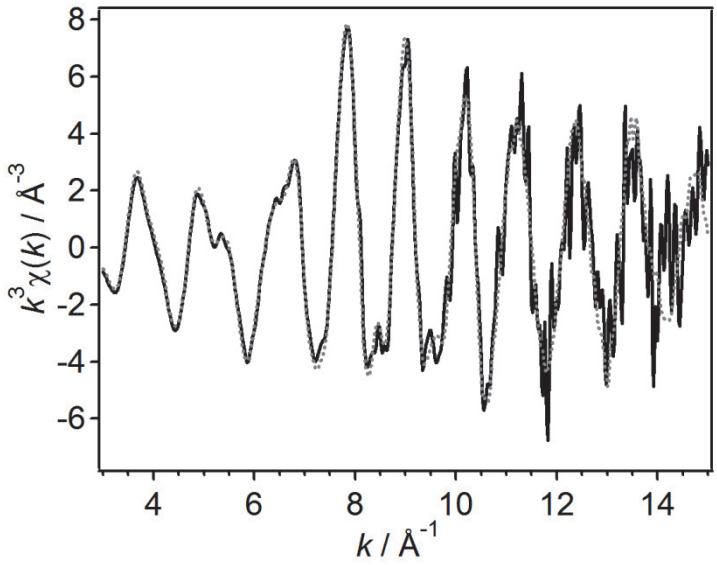

Figure 6. Au L_3-edge k^3 weighted EXAFS spectra of Au-TiO_2(p) (black solid line) and Au foil (gray dotted line).

The structure of the metal particles is different among the different kinds of metals. This is due to the difference in the strength of the metal-support interaction between the kinds of metals: the strong interaction of Rh and Pt metal particles with TiO_2 causes their disorganized structure, whereas the weak interaction of Au metal particles results in the spherical and well-organized structure.[20,21] In fact, as mentioned above, Rh and Pt are active metals for SMSI but Au is not. It is also noteworthy that the disorganized structures of Rh and Pt metal particles of Rh-TiO_2(p) and Pt-TiO_2(p) vary according to the heat treatment at 673 K to show spherical particles with obvious boundaries, as shown in Figure 7. The change in structure is also observed by the EXAFS spectra as the increase of the oscillation amplitude (Figures 3 and 4). Metal−metal bonds are probably formed beyond the metal-support interaction by the heat treatment. Therefore, the disorganized structure of Rh and Pt metal particles are produced after the photodeposition without calcination.

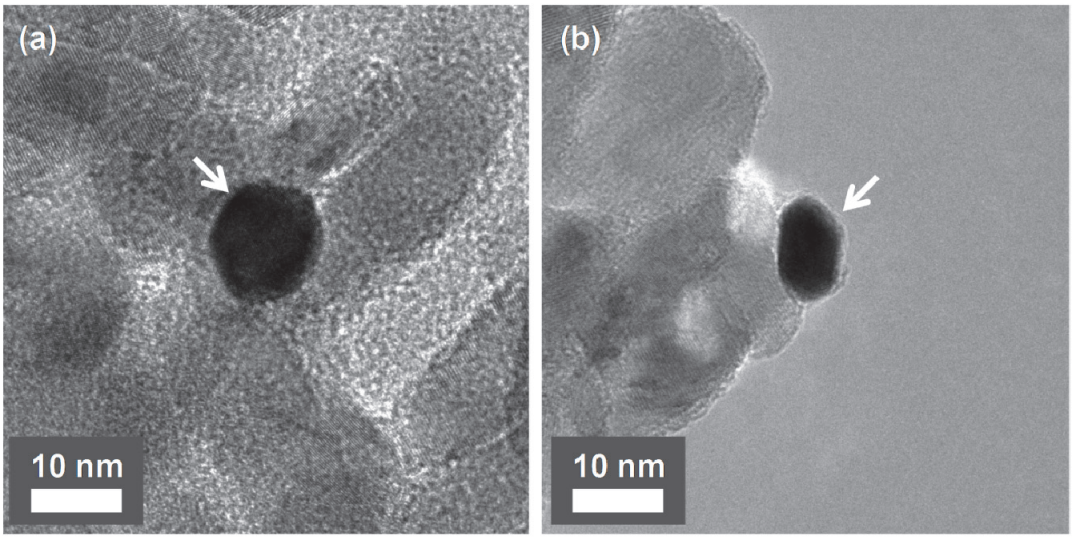

Figure 7. TEM images of (a) Rh-TiO_2(p) and (b) Pt-TiO_2(p) after heat treatment at 673 K under vacuum.

Analysis of electronic property

Figure 8 shows the Rh 3d XPS. The electronic properties of the surfaces of metal particles were evaluated from the peak energy of Rh $3d_{5/2}$ XPS. The lower energy at the peak indicates the more electron-rich surface of metal particles. The peak of Rh $3d_{5/2}$ XPS of Rh-TiO_2(p) appears at 306.5 eV (Figure 8(a)), which is of lower energy than that of Rh foil at 307.0 eV[22]. This indicates that the surface of Rh metal particles of Rh-TiO_2(p) sample is more electron-rich than Rh foil. As controls, Rh-TiO_2(i773) and Rh-TiO_2(i573), which are and are not in SMSI state, respectively, were also analyzed by XPS. (Figure 8(b) and (c)). The XPS peak of Rh-TiO_2(i773) (306.8 eV) presents at lower energy than that of Rh-TiO_2(i573) (307.2 eV), which indicates that the surface of Rh metal particles of Rh-TiO_2(i773) have more electrons than that of Rh-TiO_2(i573). This is probably due to the SMSI effect.[23,24] The peak energy of Rh-TiO_2(p) being lower than Rh-TiO_2(i773) suggests that the Rh metal particles of Rh-TiO_2(p) have a stronger interaction with TiO_2 than those of Rh-TiO_2(i773). Figure 9 represents the Pt 4f XPS. The peak of Pt $4f_{7/2}$ of Pt-TiO_2(p) appears at to have a lower binding energy (70.2 eV) than that of the references (Pt-TiO_2(i573), 70.9 eV; Pt-TiO_2(i773), 71.0 eV; Pt foil, 70.9 eV).[22] Only the Pt metal particles of Pt-TiO_2(p) are

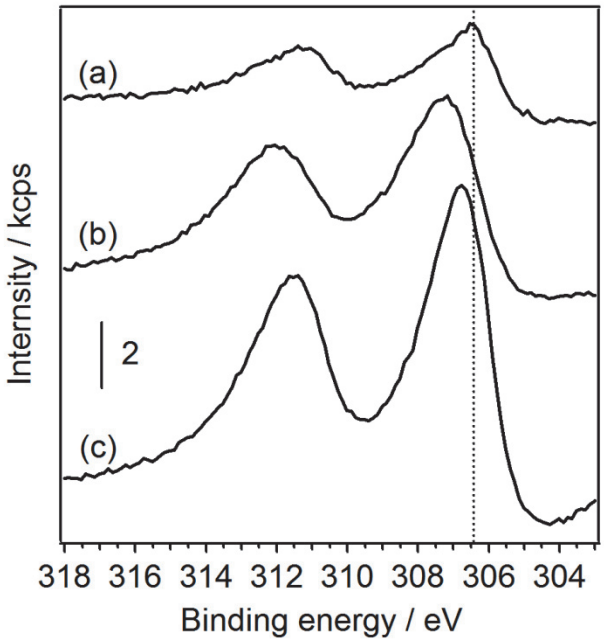

Figure 8. Rh 3d XPS spectra of (a) Rh-TiO_2(p), (b) Rh-TiO_2(i573), and (c) Rh-TiO_2(i773). The dashed lines shows the energies at the Rh $3d_{5/2}$ peak of Rh-TiO_2(p).

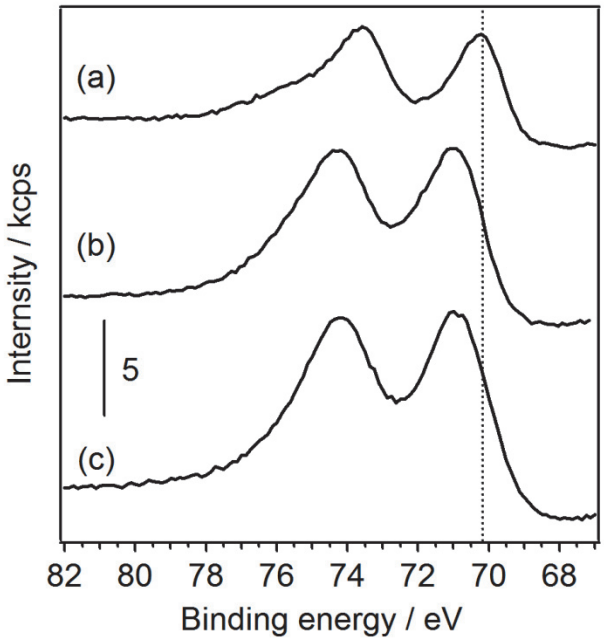

Figure 9. Pt 4f XPS spectra of (a) Pt-TiO_2(p), (b) Pt-TiO_2(i573), and (c) Pt-TiO_2(i773). The dashed lines shows the energies at the Pt $4f_{7/2}$ peak of Pt-TiO_2(p).

electron-rich. Not only Rh but also Pt metal particles interact more strongly with TiO_2 to obtain more electrons from the TiO_2 than those reduced by H_2 at the high temperature. The ideal condition for SMSI may thus be provided in the photodeposition process.

Figure 10 shows the Au 4f XPS of Au-TiO_2(p), together with those of Au-TiO_2(dp) and Au foil as references. The peak of Au $4f_{7/2}$ XPS of Au-TiO_2(p) appears at the lower binding energy (83.1 eV) than that of Au foil (83.5 eV) and at the same energy as that of Au-TiO_2(dp). This indicates that the surface electronic property of Au-TiO_2(p) is the same as that of Au-TiO_2(dp) and is more negative than that of Au foil. Figure 11 exhibits Au L_3-edge X-ray absorption near the edge structure (XANES) spectra of Au-TiO_2(p), Au-TiO_2(dp), and Au foil. We can evaluate the mean electronic properties of Au metal particles from the peak at the edge, the so-called white line. The white line at the Au L_3-edge is attributed to the electron transition from the $2p_{3/2}$ to the 5d state. The white line of Au-TiO_2(p) has a slightly greater intensity than that of Au-TiO_2(dp) and is the same as that of Au foil. This result indicates that the 5d state of Au atoms in Au-TiO_2(p) has more holes than those in Au-TiO_2(dp) and is the same as that of Au foil.[25] In other words, all of the Au atoms in Au-TiO_2(p) are more electron-poor than those in Au-TiO_2(dp) but are in the same state as those of the Au foil. However, the XPS analysis indicates that the surface electronic properties of Au-TiO_2(p) are the same as those of Au-TiO_2(dp). It is concluded that only the surface of Au metal particles of Au-TiO_2(p) is as electron-rich as that of Au-TiO_2(dp). On the other hand, Au metal particles of Au-TiO_2(p) are much larger (ca. 20−40 nm) than those of Au-TiO_2(dp) (ca. 3 nm, determined by a TEM observation). The Au metal particles of Au-TiO_2(p) should therefore be modified with TiO_2 to have the same surface electronic properties as the much smaller Au metal particles of Au-TiO_2(dp).

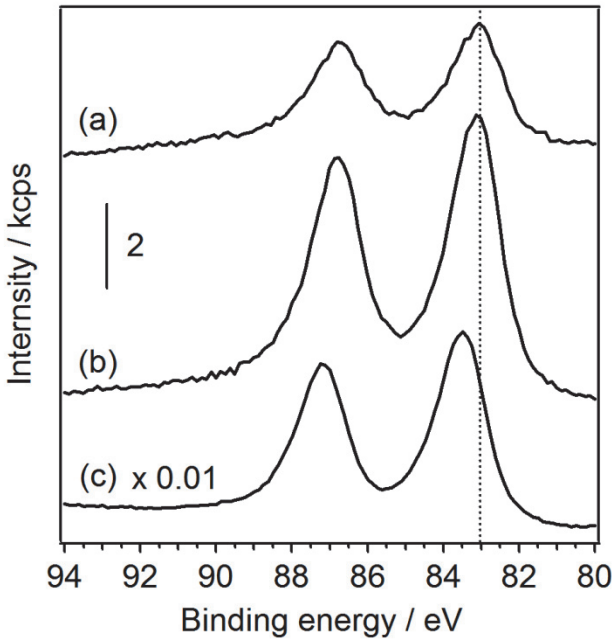

Figure 10. Au 4f XPS spectra of (a) Au-TiO_2(p), (b) Au-TiO_2(dp), (c) Au foil. The dashed lines shows the energies at the Au $4f_{7/2}$ peak of Au-TiO_2(p).

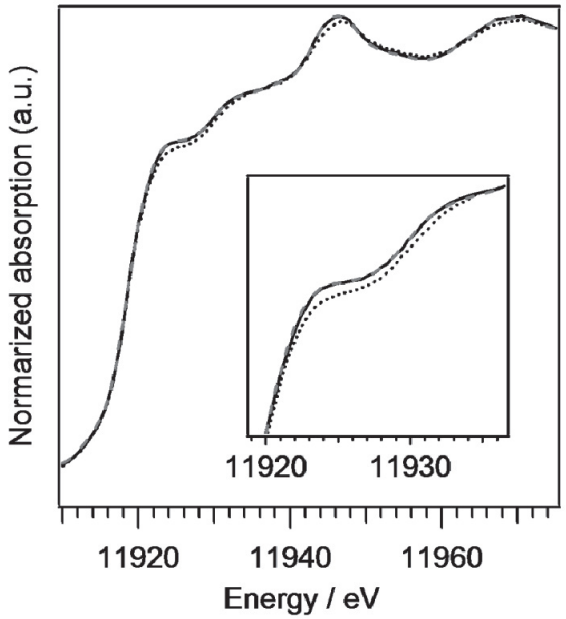

Figure 11. Au L_3-edge XANES spectra of Au-TiO_2(p) (black solid line), Au-TiO_2(dp) (black dotted line), and Au foils (gray dashed line).

Depth analysis. Figure 12 shows the change in Rh 3d and Ti 2p XPS spectra of Rh-TiO_2(p) by Xe ion sputtering. The peak intensity of the Rh 3d XPS spectrum increased with sputtering time. With greater sputtering, the two bands of Ti 2p XPS become smaller and broader in the lower-energy side. This change is due to the reduction of TiO_2 by Xe ion sputtering. The composition ratio between Rh and Ti (Rh/Ti ratio) at a given sputtering time was evaluated from those peak areas divided by respective atomic sensitivity factors.[22]

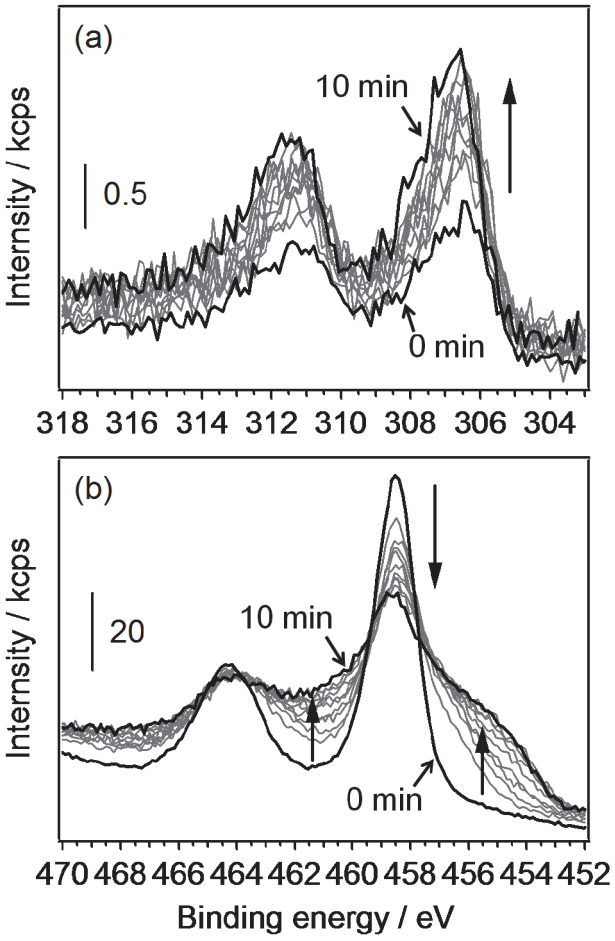

Figure 12. Series of (a) Rh 3d and (b) Ti 2p XPS spectra of Rh-TiO_2(p) during sputtering with Xe ion for 10 min.

Figure 13(a) shows the variation in Rh/Ti ratio with sputtering time of Rh-TiO_2(p). The Rh/Ti ratio of Rh-TiO_2(p) increased as the sputtering time increased, approaching 1.4% after 10 min of sputtering. The two models of Rh-TiO_2(p) are assumed from the depth profile.[26] One is that Rh metal particles having a size comparable to TiO_2 particles are modified by their interaction with TiO_2. The other is that the Rh species is intermixed with a TiO_2 particle. The EDX analysis reveals that the Rh metal particles have almost the same size as that of TiO_2 (ca. 15 nm), which is in accordance with the first model. The depth analyses of Pt-TiO_2(p) and Au-TiO_2(p) were also performed as shown in Figure 13(b) and (c). The M/Ti ratio (M: Pt, Au) increased as the sputtering time increased as well as Rh/Ti ratio of Rh-TiO_2(p) (Figure 13(a)). In addition, Pt and Au metal particles have a size comparable to TiO_2, as shown in the TEM images. It is concluded that the photodeposited metal (Rh, Pt, and Au) particles having almost the same size as TiO_2 particles are modified by their interaction with TiO_2.

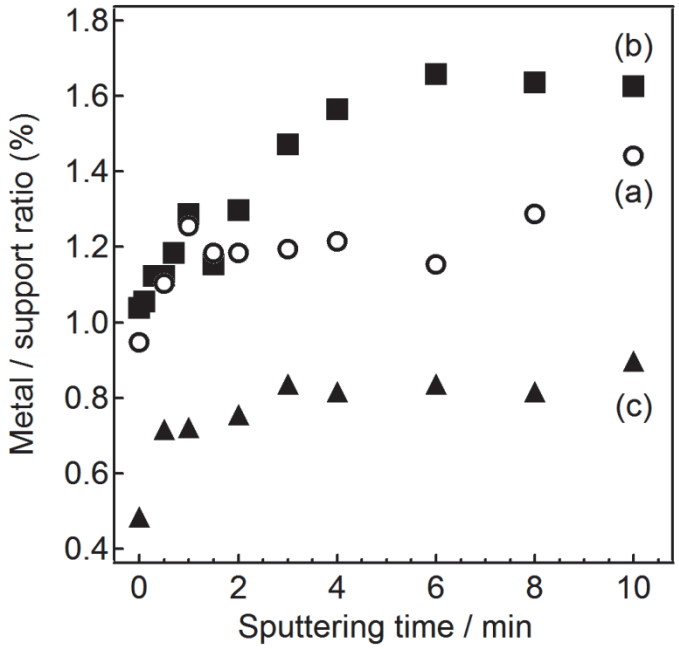

Figure 13. The change in M/Ti ratio of M-TiO_2(p) (M: (a) Rh, (b) Pt, (c) Au) by Xe sputtering for 10 min.

The mechanism of SMSI and photodeposition. $TiO_{2-\delta}$ is well known as a key species in SMSI and in the surface modification of metal particles.[11] $TiO_{2-\delta}$ can be also generated during photodeposition by the consumption of the photogenerated holes on $O^{\delta+}$ of TiO_2 without any reduction on $Ti^{\delta-}$.[27] In addition, $TiO_{2-\delta}$ originally exists on the surface of TiO_2 as defect sites. Ti^{3+} in $TiO_{2-\delta}$ contributes to an electron trap under the conduction band of TiO_2, leading to a flow of excited electrons to $TiO_{2-\delta}$[28] and a reduction of metal ions on $TiO_{2-\delta}$. In fact, the defect sites were proposed as the active sites for formation of metal particles in the photodeposition process.[16,17] Therefore, $TiO_{2-\delta}$ can influence the photodeposition.

As described above, we reported the photodeposition process of Rh metal particles. Rh metal particles do not grow in increments, but Rh metal particles having a CN of ca. 10 for the Rh–Rh pair appear consistently.[7] The CN of the Rh–Rh pair indicates the formation of particles with ca. 2−3 nm assuming the cuboctahedral structure. In this study, we proposed that the Rh metal particles strongly interact with, and are modified by their interaction with, TiO_2 (more specifically with $TiO_{2-\delta}$). In addition, the formation of the disordered structure of Rh metal particles having ca. 15 nm of domain is indicated. From these results, we now assume that Rh metal particles having ca. 2−3 nm constantly appear and aggregate to form a disordered structure, and not a spherical and well-ordered structure as is the case with Au, due to the strong metal-support interaction and modification with TiO_2. Pt metal particles are probably formed in the same manner as Rh metal particles, because Pt-TiO_2(p) shows the same behavior as Rh-TiO_2(p). On the other hand, in the case of Au, metal particles will grow in increments by aggregation to form large spherical particles, because Au does not have a strong interaction with TiO_2 in comparison with Rh and Pt.[17,29]

In this study, it is suggested that metal particles are modified by their interaction with TiO_2 in the photodeposition process, regardless of the kind of metal. $TiO_{2-\delta}$ may migrate onto metal particles, or a metal precursor may be reduced in the oxygen vacancy site of $TiO_{2-\delta}$ to form metal particles in $TiO_{2-\delta}$. On the other hand, Pt-TiO_2(p) and Pt-TiO_2(i773K) were tested for hydrogenation of ethylene. As a result, ethylene was smoothly converted to ethane on Pt-TiO_2(p); however, ethylene was hardly hydrogenated on Pt-TiO_2(i773K). It is speculated that the metal particles prepared by photodeposition are not encapsulated but are

partially modified with TiO_2, in other words, decorated by TiO_2; however, the metal particles are encapsulated by high temperature reduction with H_2. The heat condition may be essential for migration of TiO_2 to encapsulate the metal particles.

Conclusions

When Rh, Pt, and Au metal particles were photodeposited on TiO_2, the Rh and Pt metal particles showed a disorganized structure. On the other hand, Au metal particles showed a well organized and spherical structure. The difference in structure between these metals is due to the difference in the strength of metal-support interaction: Rh and Pt strongly interact with TiO_2 and Au does not. These metal particles are modified by their interaction with TiO_2, which provides electrons to the surface of metal particles. We propose the decoration model for the structure of metal particles photodeposited on TiO_2.

References

(1) Kraeutler, B.; Bard, A. J. *J. Am. Chem. Soc.* **1978**, *100*, 4317.

(2) Bamwenda, G. R.; Tsubota, S.; Nakamura, T.; Haruta, M. *Catal. Lett.* **1997**, *44*, 83.

(3) Wang, X. C.; Yu, J. C.; Yip, H. Y.; Wu, L.; Wong, P. K.; Lai, S. Y. *Chem.-Eur. J.* **2005**, *11*, 2997.

(4) Sato, S. *J. Catal.* **1985**, *92*, 11.

(5) Maeda, K.; Teramura, K.; Lu, D. L.; Saito, N.; Inoue, Y.; Domen, K. *Angew. Chem. Int. Ed.* **2006**, *45*, 7806.

(6) Lin, C. H.; Chao, J. H.; Liu, C. H.; Chang, J. C.; Wang, F. C. *Langmuir* **2008**, *24*, 9907.

(7) Teramura, K.; Okuoka, S.-i.; Yamazoe, S.; Kato, K.; Shishido, T.; Tanaka, T. *J. Phys. Chem. C* **2008**, *112*, 8495.

(8) Ohyama, J.; Teramura, K.; Okuoka, S.-i.; Yamazoe, S.; Kato, K.; Shishido, T.; Tanaka, T. *Langmuir* **2010**, *26*, 13907.

(9) Gonzalez-DelaCruz, V. M.; Holgado, J. P.; Pereniguez, R.; Caballero, A. *J. Catal.* **2008**, *257*, 307.

(10) Tauster, S. J.; Fung, S. C.; Garten, R. L. *Journal of the American Chemical Society* **1978**, *100*, 170.

(11) Tauster, S. J.; Fung, S. C.; Baker, R. T. K.; Horsley, J. A. *Science* **1981**, *211*, 1121.

(12) Tauster, S. J.; Fung, S. C.; Garten, R. L. *J. Am. Chem. Soc.* **1978**, *100*, 170.

(13) Fung, S. C. *J. Catal.* **1982**, *76*, 225.

(14) Baker, R. T. K.; Prestridge, E. B.; Garten, R. L. *J. Catal.* **1979**, *59*, 293.

(15) Fu, Q.; Wagner, T.; Olliges, S.; Carstanjen, H. D. *J. Phys. Chem. B* **2005**, *109*, 944.

(16) Kowalska, E.; Abe, R.; Ohtani, B. *Chem. Commun.* **2009**, 241.

(17) Wahlstrom, E.; Lopez, N.; Schaub, R.; Thostrup, P.; Ronnau, A.; Africh, C.; Legsgaard, E.; Norskov, J. K.; Besenbacher, F. *Phys. Rev. Lett.* **2003**, *90*, 026101.

(18) Fernandez, A.; Gonzalez-Elipe, A. R.; Caballero, A.; Munuera, G. *J. Phys. Chem.* **1993**, *97*, 3350.

(19) Calla, J. T.; Bore, M. T.; Datye, A. K.; Davis, R. J. *J. Catal.* **2006**, *238*, 458.

(20) Dassenoy, F.; Philippot, K.; Ould-Ely, T.; Amiens, C.; Lecante, P.; Snoeck, E.; Mosset, A.; Casanove, M. J.; Chaudret, B. *New J. Chem.* **1998**, *22*, 703.

(21) Chakroune, N.; Viau, G.; Ammar, S.; Poul, L.; Veautier, D.; Chehimi, M. M.; Mangeney, C.; Villain, F.; Fievet, F. *Langmuir* **2005**, *21*, 6788.

(22) Wagner C.D.; Ringgs, W. M., Davis, L.E., Moulder, J.F. *Handbook of X-ray Photoelectron Spectroscopy*; Perkin-Elmer Corp., 1979.

(23) Kao, C.-C.; Tsai, S.-C.; Chung, Y.-W. *J. Catal.* **1982**, *73*, 136.

(24) Horsley, J. A. *J. Am. Chem. Soc.* **1979**, *101*, 2870.

(25) Zhang, P.; Sham, T. K. *Appl. Phys. Lett.* **2002**, *81*, 736.

(26) Linsmeier, C.; Knozinger, H.; Taglauer, E. *Nucl. Instrum. Meth. B* **1996**, *118*, 533.

(27) Takeuchi, M.; Deguchi, J.; Sakai, S.; Anpo, M. *Appl. Catal. B* **2010**, *96*, 218.

(28) Thompson, T. L.; Yates, J. T. *Chem. Rev.* **2006**, *106*, 4428.

(29) Fernandez, A.; Caballero, A.; Gonzalez-Elipe, A. R.; Herrmann, J.-M.; Dexpert, H.; Villain, F. *J. Phys. Chem.* **1995**, *99*, 3303.

Summary

In this thesis, the author developed size controlled synthesis of metal nanoparticles and focused attention on formation mechanisms of metal nanoparticles in two useful preparation systems. The first system is wet chemical synthesis method using fast reduction. The second one is photodeposition of metal nanoparticles on TiO_2.

In Part I, the author effectively synthesized small gold nanoparticles, 2-5 nm in size, by designing the structure of passivants, and investigated the formation mechanism of gold nanoparticles by the fast reduction of gold ions in the presence of various passivants having sulfur atoms.

In Chapter 1, the author describes synthesis of a tetradentate porphyrin derivative having four thioacetyl groups in the same direction to the porphyrin plane for a passivant for efficient synthesis of small gold nanoparticles. The multidentate porphyrin passivant binds to the surface of gold nanoparticles via four Au-S bonds without acetyl groups. This binding manner contributes the strong stabilization of the particle surface. By using the multidentate passivant, gold nanoparticles were synthesized at various molar ratios of S atoms to Au atoms. As a result, the multidentate passivant afforded smaller particles than monodentate passivants. It is suggested that the tight binding of multidentate passivant to the particle surface contributes to the generation of small gold nanoparticles.

In Chapter 2, the acetyl groups of sulfur atoms of multidentate porphyrin passivants were deprotected, i.e. the author synthesized a tetradentate porphyrin passivants having two disulfide straps over one face of the porphyrin plane. As a result of size control synthesis of gold nanoparticles using the passivant having disulfide bonds, it was found that the passivant having disulfide bonds provides smaller gold nanoparticles than that having thioacetyl groups. The passivant having disulfide bonds will efficiently trap the small growing gold nanoparticles as comparison with that having thioacetyl groups. This is because the passivant with disulfide bonds have no need for deprodection of acetyl groups to bind to the surface of gold nanoparticles. Owing to the multidentation effect as well as the fast trap of the particle

surface, the passivant having two disulfide bonds gave much smaller gold nanoparticles than conventional passivants.

In Chapter 3, the author investigated fast formation process of gold nanoparticles in the presence of a conventional passivant, 1-dodecanethiol, using $NaBH_4$ as a reducing agent by means of *in situ* time-resolved QXAFS spectroscopy. The spectral analysis indicated that the gold nanoparticles are generated via very small nuclei such as Au_4 clusters and grow by aggregation between the particles. As far as the author knows, this is the first study to directly observe the fast particle formation process, more specifically, nucleation processes under actual experimental condition.

In Chapter 4, the *in situ* time-resolved QXAFS spectroscopy was applied to elucidate how the multidentate passivant (synthesized in Chapter 2) plays a role in the formation process of gold nanoparticles. The *in situ* analysis suggested that once bare gold atoms and/or very small gold cluster, i.e. nuclei, are formed, passivants begin to trap the gold metal species. Thus, the size of the gold nuclei is kinetically controlled; the bulky multidentate passivant provides larger nuclei than monodentate passivant because of the low mobility and the rigidly directed S atoms of the multidentate passivant. However, these characteristics of the multidentate passivant strongly suppress the growth of gold nanoparticles.

In Chapter 5, the author describes to clarify the variation of electronic property of gold nanoparticles passivated by 1-dodecanethiol with their size by means of *in situ* Au L_3 and L_2 edge XANES spectral analysis during growth of the gold nanoparticles. The author proposed that the characteristic band appeared in the XANES spectra of gold nanoparticles protected by 1-dodecanethiol is mainly due to the Au-S scatterings and slightly due to the d band vacancies derived from the electronic transition from gold to sulfur, however the previous reports attribute the band to only the d band vacancies. On the basis of this proposal, the electron transfer from gold nanoparticles to 1-dodecanethiol was investigated, which suggested that the electrons are increasingly transferred to S atoms (adsorbates) as the size decreased.

Part I is summarized that the gold nanoparticles protected by the passivants having sulfur atoms using strong reducing agents are generated through the nucleation and then

aggregation. Passivants kinetically trap the growing gold clusters in the early stage of particle formation, and not only kinetically but also thermodynamically suppress the growth of gold nanoparticles. Therefore, the structure, the bulkiness and the alignment of functional groups, of passivants affects on the resulting particle size. On the other hand, it is suggested that smaller gold nanoparticles give more electrons to sulfur atoms of the passivants. The electron transfer from gold to sulfur, more generally, to an adsorbate, can be the origin of the unique catalytic activity of small gold nanoparticles. The author hopes that further studies on particle formation mechanism give the guideline to obtain and take advantage of metal clusters having peculiar properties.

In Part II, the photodeposition mechanism of metal nanoparticles on TiO_2 and the structure of photodeposited metal nanoparticles derived from metal-support interaction is described.

In Chapter 6, the photodeposition mechanism of rhodium nanoparticles on TiO_2 was investigated. The *in situ* time-resolved DXAFS spectral analysis revealed that rhodium nanoparticles having uniform size constantly appear on TiO_2 with increasing the photoirradiation time. The DXAFS and ICP analyses revealed that the adsorption of Rh^{3+} ion is not the rate determining step of photodeposition. The reduction rate of Rh^{3+} ion depending on the p*K*a value of alcohols and the initial amount of Rh^{3+} ion did not vary the resulting size of rhodium nanoparticles. The XAFS analysis of these various conditions indicated the same particle formation mechanism. The particle formation mechanism is not applicable to any mechanisms proposed in wet chemical synthesis of metal nanoparticles. This interesting result will suggest the strong interaction between rhodium and TiO_2.

In Chapter 7, the structures of rhodium, platinum, and gold nanoparticles photodeposited on TiO_2 was explored focusing attention on the interaction between metal and support. The rhodium and platinum metal particles showed disorganized structure, because rhodium and platinum strongly interact with TiO_2. On the other hand, Au metal particles represented well organized and spherical structure, since gold does not interact strongly with TiO_2. Although the difference in structure between kinds of metals was observed, it was

found that all of the metal particles are modified with TiO_2. The author proposes that $TiO_{2-\delta}$ generates during the photodeposition and migrate on metal particles, and, in the case of the metals in group VIII (SMSI metal), causes the disorganization of structure due to the strong interaction between metal and $TiO_{2-\delta}$. The strong interaction and modification of rhodium particles with $TiO_{2-\delta}$ can inhibit the growth of metal particles to result in the constant appearance of particles with uniform size presented in Chapter 6.

In summary of Part II, the metal nanoparticles are formed through unique formation mechanism in the photodeposition of metal nanoparticles while the resulting metal nanoparticles interact with photocatalyst. The metal-photocatalyst interaction affects on the morphology of metal nanoparticles. These findings will help to understand metal nanoparticles modifying photocatalysts.

List of publications

Part I

Chapter 1.

1. One-Phase Synthesis of Small Gold Nanoparticles Coated by a Horizontal Porphyrin Monolayer
   Junya Ohyama, Yutaka Hitomi, Yasuhiro Higuchi, Masashi Shinagawa, Hidefumi Mukai, Masahito Kodera, Kentaro Teramura, Tetsuya Shishido and Tsunehiro Tanaka
   Chemical Communications **2008**, 6300-6302.

2. Size Controlled Synthesis of Gold Nanoparticles by Porphyrin with Four Sulfur Atoms
   Junya Ohyama, Yutaka Hitomi, Yasuhiro Higuchi and Tsunehiro Tanaka
   Topics in Catalysis **2009**, *52*, 852-859.

Chapter 2.

3. Efficient Capping of Growing Gold Nanoparticles by Porphyrin Having Two Disulfide Straps over One Face
   Yutaka Hitomi, Junya Ohyama, Yasuhiro Higuchi, Kazuki Aoki, Tetsuya Shishido, Takuzo Funabiki, Masahito Kodera, and Tsunehiro Tanaka
   Bulletin of the Chemical Society of Japan **2010**, *83*, 1392-1396.

Chapter 3.

4. In Situ Observation of Nucleation and Growth Process of Gold Nanoparticles by Quick XAFS Spectroscopy
   Junya Ohyama, Kentaro Teramura, Yasuhiro Higuchi, Tetsuya Shishido, Yutaka Hitomi, Kazuo Kato, Hajime Tanida, Tomoya Uruga, and Tsunehiro Tanaka
   ChemPhysChem **2011**, *12*, 127-131.

Chapter 4.

5. In Situ Quick XAFS Spectroscopy Study on the Formation Mechanism of Small Gold Nanoparticles Supported by Porphyrin-cored Tetradentate Passivants
   Junya Ohyama, Kentaro Teramura, Yasuhiro Higuchi, Tetsuya Shishido, Yutaka Hitomi, Kazuaki Aoki, Takuzo Funabiki, Masahito Kodera, Kazuo Kato, Hajime Tanida, Tomoya Uruga, and Tsunehiro Tanaka
   Physical Chemistry Chemical Physics submitted.

Chapter 5.

6. In Situ Au L_3 and L_2 edge XANES Spectral Analysis during Growth of Thiol Protected Gold Nanoparticles for the Study on Particle Size dependent Electronic Properties
   Junya Ohyama, Kentaro Teramura, Tetsuya Shishido, Yutaka Hitomi, Kazuo Kato, Hajime Tanida, Tomoya Uruga, and Tsunehiro Tanaka
   Chemical Physics Letters submitted.

Part II

Chapter 6.

7. Investigation of Formation Process of Photodeposited Rh Nanoparticles on TiO_2 by In Situ Time-Resolved Energy-Dispersive XAFS Analysis
   Junya Ohyama, Kentaro Teramura, Shin-ichi Okuoka, Seiji Yamazoe, Kazuo Kato, Tetsuya Shishido, and Tsunehiro Tanaka
   Langmuir **2010**, *26*, 13913-13923.

Chapter 7.

8. Modification of Metal Nanoparticles with TiO_2 and Metal-Support Interaction in Photodeposition
   Junya Ohyama, Akira Yamamoto, Kentaro Teramura, Tetsuya Shishido, and Tsunehiro Tanaka
   ACS Catalysis in press.

The following papers are not included in this thesis

9. Adsorption of Manganese Porphyrin on Metal Oxides and Its Enhanced Catalytic Activity on Epoxidation Reaction
   Yutaka Hitomi, Hidefumi Mukai, Junya Ohyama, Masashi Shinagawa, Tetsuya Shishido, and Tsunehiro Tanaka
   Chemistry Letters **2007***, 36,* 660-661.

10. Fast Guest Exchange of a 1:1 Zinc Porphyrin–Amine Host–Guest Complex via a Six-Coordinated Zinc Porphyrin
    Yutaka Hitomi, Junya Ohyama, Minori Takegoshi, Akira Ando, Takuzo Funabiki, Masahito Kodera, and Tsunehiro Tanaka
    Bulletin of the Chemical Society of Japan **2010**, *83*, 950-952.